PLASMA INSTABILITIES IN HALL THRUSTERS

A Thesis Submitted to the

College of Graduate Studies and Research

in Partial Fulfillment of the Requirements

for the degree of Doctor of Philosophy

in the Department of Physics and Engineering Physics

University of Saskatchewan

Saskatoon

By

Winston Frias Pombo

PERMISSION TO USE

In presenting this thesis in partial fulfilment of the requirements for a Postgraduate degree from the University of Saskatchewan, I agree that the Libraries of this University may make it freely available for inspection. I further agree that permission for copying of this thesis in any manner, in whole or in part, for scholarly purposes may be granted by the professor or professors who supervised my thesis work or, in their absence, by the Head of the Department or the Dean of the College in which my thesis work was done. It is understood that any copying or publication or use of this thesis or parts thereof for financial gain shall not be allowed without my written permission. It is also understood that due recognition shall be given to me and to the University of Saskatchewan in any scholarly use which may be made of any material in my thesis.

Requests for permission to copy or to make other use of material in this thesis in whole or part should be addressed to:

Head of the Department of Physics and Engineering Physics
Rm 163
116 Science Place
University of Saskatchewan
Saskatoon, Saskatchewan
Canada
S7N 5E2

ABSTRACT

Plasmas involving strong electron drift in crossed electric and magnetic fields are of great interest for a number of applications such as space propulsion and material processing plasma sources. Specific applications include Hall thrusters, which are high efficiency, low thrust propulsion systems used on many missions for satellite orbit corrections and for future planned interplanetary missions, as well as magnetrons of various configurations used in plasma deposition devices. Similar conditions also exist in the E-layer of the ionosphere and on the Sun.

Despite many successful applications of Hall thrusters and other Hall plasma sources, some aspects of their operation are still poorly understood. A particularly important problem is the anomalous electron transport, which greatly exceeds classical collisional values. Hall plasma devices exhibit numerous turbulent fluctuations in a wide frequency range and it is believed that fluctuations resulting from plasma instabilities are likely one of the main causes of the observed anomalous transport. Plasma turbulence also affects many other important processes such as electron injection, location of the ionization region and wall erosion among others that influence the operation and efficiency of Hall thrusters.

In Hall thrusters, the $\mathbf{E}_0 \times \mathbf{B}_0$ flow is made unstable due to gradients in the plasma density, temperature and magnetic field. The gradient drift instabilities are long wavelength instabilities that propagate in the azimuthal direction. A fluid theory of these unstable modes is proposed. It is shown that a full account of the compressibility of the electron flow in inhomogeneous magnetic field leads to quantitative modifications of the previously obtained instability criteria and characteristics of the unstable modes.

The $\mathbf{E}\times\mathbf{B}$ drift also drives ion sound type instabilities in Hall thrusters. The reactive/dissipative response of the closure current to the thruster walls drives these negative energy modes. A model for this type of instabilities is proposed and analyzed for typical Hall thruster conditions. It is shown how wall parameters modify the characteristic growth rate and frequency of the unstable modes and the related anomalous transport.

Nonlinear phenomena are important to understand different aspects of the Hall thruster plasma dynamics. A nonlinear fluid model for the typical Hall thruster plasma is proposed. The model takes into account electron inertia, electron collisions with neutrals, density gradients as well as

various nonlinear terms that arise from the electron drift and nonlinear polarization that were included via the gyroviscous cancellation. The proposed model includes the long wavelength and the low hybrid modes destabilized by density gradients and collisions. This system of fluid equations was implemented using the computational framework BOUT++ from which a set of nonlinear simulations of plasma turbulence was performed. It is shown from these first principles nonlinear simulations that small scale low hybrid oscillations result in an anomalous electron current significantly exceeding the classical collisional current.

ACKNOWLEDGEMENTS

This dissertation is the culmination of a very interesting stage in my life. Many people have shaped my experience during these many years I have been in Saskatoon. First I would like to thank my supervisor Dr Andrei I. Smolyakov. You received me as a Master's student back in 2008. Since that time and going through an M.Sc and now a PhD, you have been my supervisor and helped me grow as a student and a researcher. I particularly appreciate your constant support and encouragement throughout the most difficult times during these years, during which I may have doubted about whether I would have been able to successfully complete this project. I believe that it would not have been possible if you had not dedicated the amount of time and effort that you dedicated to me as your student. I am really grateful and if I have the chance in the future to be someone's supervisor, I wish I can be as good a supervisor as you have been to me.

I also wish to thank Dr Maxim Umansky and the people at the Physics division of the LLNL. Maxim hosted me during a visit to LLNL in 2012. He was an excellent host and taught me a lot about BOUT++. He has also been really eager and ready to help me during the times I have had difficulties with BOUT++. Without your help, this project would have been much more difficult to complete. In this regard I cannot leave without thanking Dmitry Meyerson who has also helped me a lot with BOUT++.

I also thank Drs. Yevgeny Raitses and Igor Kaganovich from the PPPL. We have collaborated with them during the realization of this project and their suggestions as well as the discussions we have had with them have greatly influenced the content of this dissertation. Many thanks are also owed to the members of my committee for their input and suggestions that have contributed to the improvement of this dissertation.

I believe that in order to be successful as a student, the other aspect of one's life need to be taken care of. for this reason I am grateful to all those I have been lucky to meet during my time as a student at the University of Saskatchewan, my fellow graduate students, Louis Hthwu, Lorin Briand, Koloman Varady, Sayf Gaymudi, Yue Ding, Kurt Krueger, Yelu Liu, Carl Dunlea, Sandeep Litt, Oleksandr Koshkarov and Ivan Romadianov. You have made my time at school more enjoyable. Deep appreciations also go to all the faculty and staff I have met at the Physics department, Drs Akira Hirose, Chijin Xiao, Aleksandr Koustov, Gap Soo Chang and Pasha Ponomariov, Dave

McColl, Marje Granjude and Debbie Parker.

I would like to also thank my friends outside of school, Leonardo, Joel, Maria and Pedro, Marco and Danny, Vicky and Alejandro, Carlos and Jenny. The time I have shared with you has enriched and made very pleasant my stay in Saskatoon, gracias muchachos!

I also thank my parents as well as my sister for giving me their love and for providing me with an environment where my curiosity and desire to learn and be a better person was always fostered. I love you very much, you are the main reason I am the person that I am today.

Last but not least, I want to thank my lovely wife Lili. There is a before and after in my life since you came to Saskatoon. You are my constant support and encouragement. You make me try to become a better person every day, I love you very much.

DEDICATION

A mis padres y mi hermana, a mi Lili y a mis amigos de aquí y de allá, gracias por todo, sin ustedes a mi lado nada de esto hubiera sido posible.

CONTENTS

LIST OF TABLES

LIST OF FIGURES

CHAPTER 1

HALL THRUSTERS

1.1 Introduction and motivation

The future of humankind depends on space exploration. Modern civilization and technology rely on satellites for communications, remote sensing and navigation. In the future, humankind will try to explore the different planets and asteroids in our solar system and beyond. Since the currently used chemical rocket technology is not well suited for deep space exploration, new and better technologies need to be developed.

A spacecraft changes its velocity by expelling a part of its mass at some exhaust velocity v_{ex}. The resulting thrust force acting on the spacecraft is given by the expression

$$T = \frac{d\left(m_p v_{ex}\right)}{dt} = \dot{m}_p v_{ex}. \tag{1.1}$$

In 1903, Russian scientist Konstantin E. Tsiolkovsky, derived a formula that relates the maximum change in velocity a rocket can attain to the exhaust velocity of the propellant and the mass of the rocket [14],

$$\Delta v = -v_{ex} \ln\left(\frac{M_d}{M_d + m_p}\right), \tag{1.2}$$

where Δv is the change in velocity of the spacecraft, M_d is the "dry" mass of the spacecraft or the payload, and m_p is the mass of the propellant. The total initial mass of the spacecraft is the sum of the mass of the payload and the mass of the propellant.

From Tsiolkovsky's equation, it can be seen that a high exhaust velocity is needed to achieve a high Δv. In a chemical rocket, the exhaust velocity is limited by the temperature of the combustion gases, which is a fraction of an eV [1]. This comparatively low exhaust velocity means that very high

[1] 1 eV = 11604.5 K. The temperature inside a rocket combustion chamber is around 3500 - 5000 K

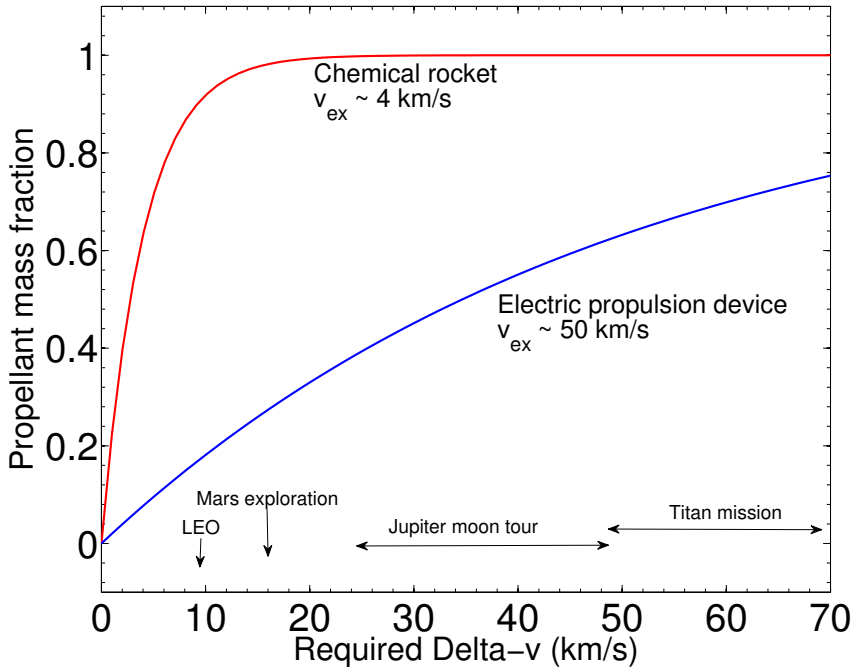

Figure 1.1: Propellant mass fraction as function of required Δv for different space missions.

propellant mass ratios are needed to reach useful Δv values (see Fig. 1.1), making chemical rockets impractical for deep space exploration. To obtain higher exhaust velocities, electromagnetic fields can be used to accelerate a propellant. This technology is known as electric propulsion.

1.2 Electric propulsion

Electric propulsion is a technology that uses electric and magnetic fields to achieve high propellant exhaust velocities [1]. The concept of electric propulsion was first discussed by Goddard (1906) and later by Tsiolkovsky (1911) and Oberth (1926) [15]. Electric propulsion devices can be divided into three categories, depending on how the electric and magnetic fields are used to generate thrust. These three categories are electrothermal, electrostatic and electromagnetic propulsion [1]. Electrothermal propulsion uses an electric discharge to heat a propellant, which is then expelled through a nozzle to generate thrust, similar to a chemical rocket. Electrostatic propulsion uses an electrostatic electric field to accelerate ions, which are then expelled from the spacecraft to pro-

duce thrust. In electromagnetic propulsion, electromagnetic fields accelerate the ions to generate the thrust.

Electric propulsion devices operate at voltages of several hundred volts. This voltage allows the propellant ions to be accelerated to velocities more than ten times higher than the exhaust velocities in a conventional rocket [1]. An electric propulsion device can then generate as much as ten times more impulse per unit of propellant consumed as a chemical rocket. The ratio of impulse generated per weight of consumed propellant is known as specific impulse, I_{sp}

$$I_{sp} = \frac{T}{\dot{m}g} = \frac{v_{ex}}{g}, \tag{1.3}$$

where g is the gravitational constant at the Earth surface. The higher value of the specific impulse of an electric propulsion device, around 1000 - 10 000 s, means that electric propulsion devices need less propellant to reach a given Δv than a chemical rocket. The electric field in an electric propulsion device is generated by an external power source. Modern electric propulsion devices can use onboard batteries and/or solar arrays [1]. The power available to the electric propulsion device limits the amount of thrust it can generate. For the typical values of specific impulse and available power, the thrust of a typical electric propulsion device is of the order of a few millinewtons. The combination of low thrust and the possibility of a precise control of the propellant usage makes electric propulsion devices very useful for complicated and high precision maneuvers in outer space [1]. One upcoming mission that will take advantage of the capabilities of Hall thrusters is the Asteroid Retrieval Mission (ARM), whose goal is to redirect near Earth asteroids to a stable orbit around the Moon [16]. Additional goals of the mission include possible applications to planetary defense and asteroid mining [16].

In electric propulsion devices the ions are generated by ionizing a propellant gas. The electric field that accelerates the produced ions also acts on the electrons, accelerating them in the opposite directions to the ions. The electron current reduces the efficiency of the electric propulsion device since the power source (the battery) sustains both the ion and electron currents, but only the ions generate thrust. One way to improve the efficiency of electric propulsion devices is to reduce the electron current. The electron current can be reduced by introducing a magnetic field perpendicular to the direction of the electric field. The magnitude of the magnetic field is chosen such that its effect on the ion motion is negligible. In this crossed field arrangement, the electrons move in

closed drift trajectories perpendicular to the electric and magnetic fields and are not accelerated in the direction of the electric field like the ions. A type of electric propulsion device that uses crossed electric and magnetic fields to confine the electrons is the Hall thruster shown in Fig. 1.2.

1.3 Hall thrusters

Hall thrusters are coaxial plasma accelerators used for spacecraft propulsion. Hall thrusters, also known as closed drift thrusters, were first developed in the former Soviet Union and in the USA in the 1960's. The first successful flight of a Hall thruster was in December 1971 with the launch of an SPT-50 aboard a Meteor satellite. Since that date over 240 Hall thrusters have been launched with a success rate of 100% [1]. Nowadays, intensive research on Hall thrusters is carried out by government and commercial organizations in the United States, the Russian Federation, Japan and Europe [1].

There are two main types of Hall thrusters, the thruster with extended acceleration zone, also known as stationary plasma thruster (SPT) and the thruster with anode layer (TAL) [1,2]. The SPT thruster configuration has a channel made of a ceramic material and has a channel length that is long compared to its width (distance between the channel walls). Collisions of electrons and ions from the plasma with the ceramic walls of the SPT produce low energy secondary electrons. These low energy secondary electrons help keep the channel plasma at a relative low temperature, which results in a more extended and gradual acceleration process [2]. This longer acceleration zone is the reason of the name thruster with extended ionization zone. A thruster with anode layer (TAL) is characterized by having conducting walls and a channel length short compared to the channel width [2]. In a TAL configuration, there is an increase of the plasma temperature towards the anode. The increase in plasma temperature towards the anode results in an increase in plasma potential, such that the ionization of the neutral propellant and acceleration of the ions occur mainly in this thin layer close to the anode [2]. This is the reason for the name thruster with anode layer. Most devices currently in operation and under development are of the stationary plasma type (SPT) [1,2]. In this dissertation, unless explicitly noted, Hall thruster refers to a thruster of the SPT type.

The cross section of a Hall thruster is shown in Fig. 1.2. A plasma discharge is created between the anode and the cathode. An axial electric field is then established between the anode and the

cathode. Initial electrons are produced by the cathode and become confined following closed azimuthal drifts perpendicular to both the external electric and magnetic fields. A propellant, most commonly xenon, is injected into the discharge chamber from the anode region. The neutral atoms are then ionized by collisions with the trapped electrons. These ions are accelerated by the axial electric field and expelled at the exit of the thruster, providing thrust. The cathode also supplies electrons that neutralize the expelled ion beam to maintain charge neutrality [1, 2].

The electrons in the discharge chamber diffuse to the anode by colliding with the neutral propellant gas atoms, electrons and ions [1, 2]. Plasma fluctuations are also an important source of electron current [1, 2]. The axial electron current to the anode greatly reduces the efficiency of the thruster [1, 3, 17] and the exhaust velocity [18]. Experimentally, it has been observed that the electron current to the anode is 10–100 times larger than what is expected from collisions alone [4, 17, 19–21]. Several mechanisms have been proposed to explain this anomalous current. The two main mechanisms thought to be responsible for the observed anomalous electron transport are collisions with the chamber walls [17, 22] and plasma fluctuations [20, 23, 24].

The magnetic field in a Hall thruster is such that the electron Larmor radius, ρ_e, is much smaller than the axial length of the thruster channel, L, while at the same time, the ion Larmor radius, ρ_i is larger than the channel length.

$$\rho_e = \frac{v_{th}}{\omega_{ce}} = \frac{m}{eB}\sqrt{\frac{8kT_e}{\pi m}} << L, \tag{1.4}$$

$$\rho_i = \frac{v_{\perp i}}{\omega_{ci}} = \frac{M}{eB}\sqrt{\frac{2eV_d}{M}} >> L. \tag{1.5}$$

Since the ion Larmor radius is larger than the channel length, the ions are considered unmagnetized.

The ratio of the electron cyclotron frequency, ω_{ce} to the electron collision frequency (with all species), ν_e, is known as the electron Hall parameter, Ω_{He}. For trapped electrons in a Hall thruster, the electron Hall parameter is much larger than one,

$$\Omega_{He} = \frac{\omega_{ce}}{\nu_e} >> 1. \tag{1.6}$$

[1]Image in Public Domain, taken from "Wfm hall thruster" by Finlay McWalter - Based on File:Wfm hall thruster.png by David Staack. Licensed under Public Domain via Commons.

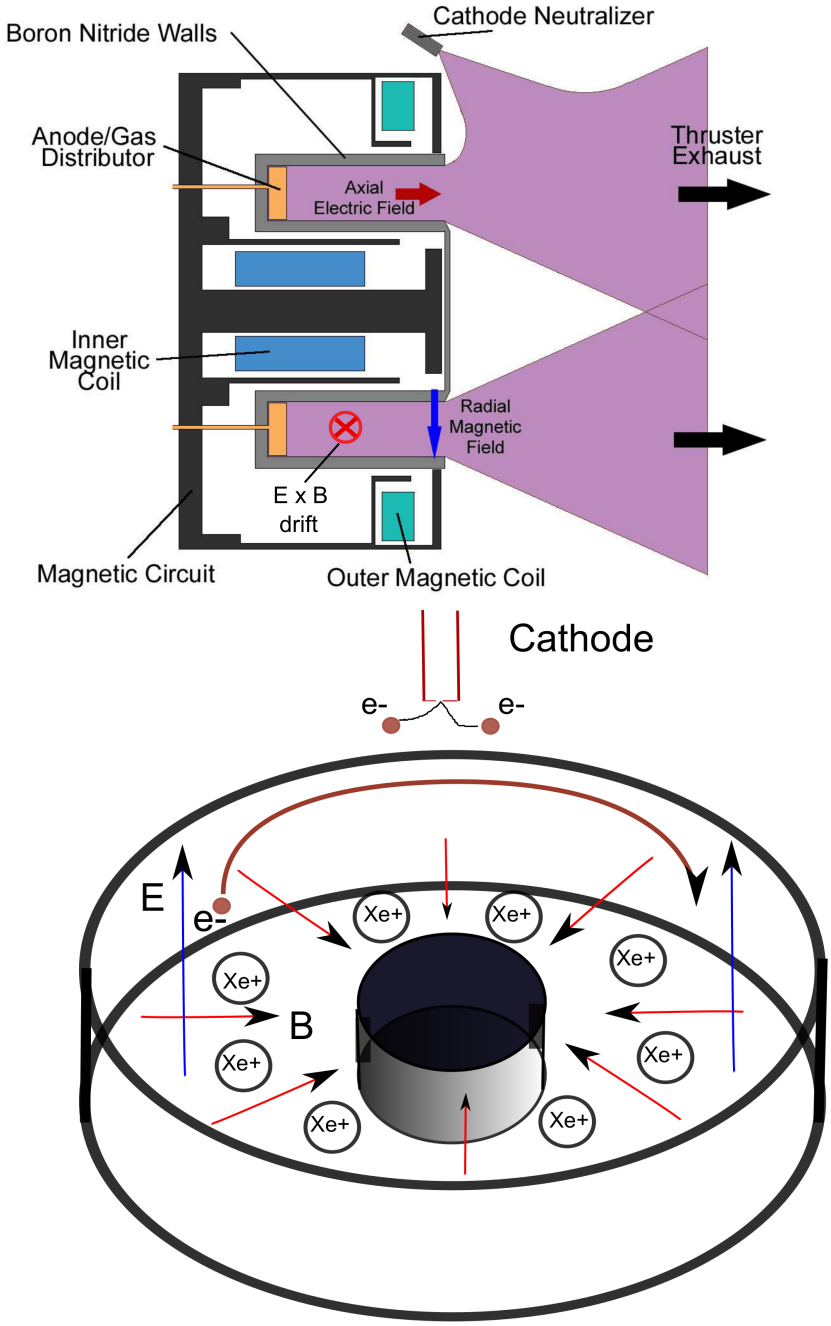

Figure 1.2: Axial cross section of a Hall thruster [1] (top) and view sideways showing the cylindrical geometry of a Hall thruster (bottom).

The ion Hall parameter can be defined in a similar form as the electron Hall parameter, as the ratio of the ion cyclotron frequency ω_{ci} to the ion collision frequency (with all species) ν_i. The ion Hall parameter is much smaller than one,

$$\Omega_{Hi} = \frac{\omega_{ci}}{\nu_i} << 1. \tag{1.7}$$

The magnitudes of the radial magnetic and the axial electric fields reach their maximum value near the exit of the thruster channel [1] (see Fig. 1.3). Electrons are injected at a relatively high energy to produce ionization of the neutral gas [1, 2], which combined with the high value of the electric field and the collision frequency at the channel exit provides for a peak of the electron temperature at this region. In a Hall thruster, most neutrals are ionized before they reach the exit of the channel, where they are accelerated by the electric field [1]. This results in an overlap between the ionization and acceleration regions. This overlap can create some divergence in the outgoing ion beam, which reduces the efficiency of the thruster [1, 2]. The ions produced after ionization leave the thruster channel without experiencing many more collisions (the ionization region is short) and are not substantially heated, resulting in a comparatively low ion temperature, compared to that of the electrons (T_i 1 ev) [1, 2].

In the crossed axial electric and radial magnetic fields, the electrons have an azimuthal velocity known as the $\mathbf{E} \times \mathbf{B}$ drift velocity [2]

$$\mathbf{v}_E = \frac{\mathbf{E} \times \mathbf{B}}{B^2} = -\frac{E_z}{B_r}\hat{\theta}. \tag{1.8}$$

The electrons moving with the $\mathbf{E} \times \mathbf{B}$ drift velocity generate a current density in the azimuthal direction, known as Hall current density [1]. The Hall current is calculated by integrating the Hall current density over the radial-axial cross section, that it traverses [2]

$$I_H = e\, n_e \int v_E dA_{rz} = e\, n_e w \frac{V_d}{B}, \tag{1.9}$$

where w is the radial width of the thruster channel and V_d is the potential difference supplied by the battery [3] [2].

The ion current that forms the ion beam leaving the thruster in the axial direction is given by

$$I_i = e\, n_i v_i A_{r\theta} = e\, n_i \sqrt{\frac{2eV_d}{M}}\, 2\pi R w, \tag{1.10}$$

[2] See Section 2.2

[3] The axial electric field is approximately the discharge voltage, V_d, divided by the axial length, L

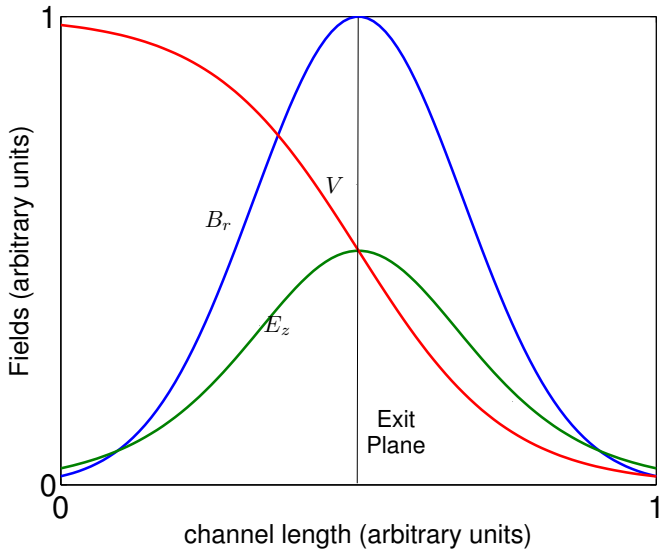

Figure 1.3: Typical profiles of the radial magnetic field, axial electric field and potential along the channel length of a Hall thruster.

where R is the mean radius of the thruster. The ion current is proportional to the Hall current as [1, 2]

$$I_i = I_H \, B \sqrt{\frac{2e}{MV_d}} \, 2\pi R, \tag{1.11}$$

where A is the cross sectional area of the beam.

In a Hall thruster the thrust is transferred from the ions to the spacecraft via the Lorentz force on the Hall current [1],

$$\mathbf{T} = \int \mathbf{J}_H \times \mathbf{B} \, dV = I_H \, B \, 2\pi R \, \hat{\mathbf{x}}. \tag{1.12}$$

The thrust can be calculated as a function of the ion beam current by using Eq. (1.11) [1, 2]

$$T = I_i \sqrt{\frac{MV_d}{2e}}. \tag{1.13}$$

The thrust is thus transferred from the outgoing ions to the thruster body via the force on the Hall current due to the magnetic field. This thrust is of the same form that the one derived from calculating the term $v_i dM/dt$. The expelled mass rate can be approximated as $dM/dt \approx I_i m_i/e$ [1], which produces a thrust of

$$\frac{dM}{dt} v_i \approx I_i \sqrt{\frac{2MV_d}{e}}, \tag{1.14}$$

which is similar (within a factor of $\sqrt{2}$) to the thrust calculated from the Hall current given by Eq. (1.13).

The efficiency of the thruster is defined as the ratio of the power in the outgoing ion beam (jet power) to the total input power provided by the battery [1].

$$\eta_T = \frac{P_{jet}}{P_{in}}. \tag{1.15}$$

The jet power is related to the thrust of the thruster as [1]

$$P_{jet} = \frac{1}{2}\dot{m}_p\, v_{ex}^2 = \frac{T^2}{2\dot{m}_p}, \tag{1.16}$$

and the power supplied to the thruster is the product of the discharge voltage, V_d and the discharge current, I_d produced by the battery,

$$P_{in} = V_d\, I_d. \tag{1.17}$$

Using Eqs. (1.16)–(1.17), the efficiency of the thruster is

$$\eta_T = \frac{T^2}{2\dot{m}_p\, V_d\, I_d}. \tag{1.18}$$

The axial current produced by the battery, I_d, is equal to the sum of the axial electron current and ion beam current (which produces the thrust). When the axial electron current to the anode is reduced, a larger fraction of the discharge current I_d is used to sustain the ion beam current, which increases the efficiency of the thruster. Modern Hall thrusters can operate at efficiencies of around 50% – 70% [1, 2].

In Table 1.1, the values for the most important parameters for a typical Hall thruster are presented.

1.4 Summary

Electric propulsion uses electric and magnetic fields to accelerate the propellant and provide thrust to an spacecraft. Electric propulsion devices have higher exhaust velocities and use less propellant than a chemical rocket. An electric thruster is then able to achieve a higher Δv than a chemical rocket, making them more useful for deep space exploration [1]. Electric propulsion devices produce low thrust and can use their propellant over long periods of time, which is why they are used

Parameter	**Value**
Plasma Density (n)	$10^{17} - 10^{18}$ m^{-3}
Neutral Density (n_n)	$10^{18} - 10^{19}$ m^{-3}
Electron Temperature (T_e)	$10 - 40$ eV
Ion Temperature (T_i)	~ 1 eV
Debye Length (λ_D)	$10^{-5} - 10^{-4}$ m
Electron-Neutral Collision Freq. (ν_{en})	$10^5 - 10^6$ s^{-1}
Electron-Ion Collision Freq. (ν_{ei})	$\sim 10^5$ s^{-1}
Electron-Wall Collision Freq. (ν_{ew})	$\sim 10^5$ s^{-1}
Ion-Neutral Collision Freq. (ν_{in})	$10^4 - 10^5$ s^{-1}
Electric Field ($\mathbf{E}$)	$2 \times 10^3 - 4 \times 10^4$ V/m
Magnetic Field ($\mathbf{B}$)	$0.010 - 0.020$ T ($100 - 200$ G)
$\mathbf{E} \times \mathbf{B}$ Drift Velocity ($\mathbf{u}_0$)	$\sim 10^5 - 10^6$ m/s
Electron Cyclotron Frequency (ω_{ce})	$\sim 10^9$ Hz
Ion Cyclotron Frequency (ω_{ci})	$\sim 10^4$ Hz
Electron Larmor Radius (ρ_e)	$\sim 10^{-3}$ m
Ion Larmor Radius (ρ_i)	~ 1 m
Inner Radius	35 mm
Outer Radius	50 mm
Channel Width	15 mm
Acceleration Region	~ 1 cm
Thrust ($\mathbf{T}$)	~ 80 mN
Exhaust Velocity (v_{ex})	~ 10000 m/s
Specific Impulse ($I_{sp} = v_{ex}/g$)	~ 1000 s

Table 1.1: Values of typical parameters of a Hall thruster [1–3].

for high precision maneuvers such as orbit transfer and keeping. Hall thrusters are the main type of electric propulsion device currently in use [1, 2, 25]. Since they were first developed in the 1960's, more than 240 Hall thrusters have successfully flown in space missions [1, 25].

Hall thrusters are currently being developed by government agencies and private companies in the USA, Russia, Europe and Asia. There is great interest in improving the lifespan of the thruster and increasing their overall efficiency [1, 2, 25, 26]. New and better materials, like aluminum oxide and boron nitride, are being used for the walls of the thruster. The use of these materials reduces the sputtering due to high energy electrons and ions impinging on the walls that affects the plasma density in the acceleration region and the transport properties inside the thruster [1]. There is also interest in designing new cathodes that improve the electron injection to the thruster channel and increase the efficiency of the thruster [1, 2, 26]. Research is being done on how to control the electric and magnetic fields inside the thruster in order to locate both the ionization and acceleration regions close to the exit plane of the thruster [2, 26]. This is done with the goal of minimizing the collisions of energetic ions with the dielectric walls of the thruster channel and thus achieve higher efficiencies and larger lifetimes for the thruster.

It has been experimentally observed that in Hall thrusters the electron current to the anode is 10–100 times the current that is expected from collisions alone. This higher than expected current is known as anomalous transport. Anomalous transport is one of the most important areas of Hall thrusters research since anomalous transport reduces the efficiency of the thruster. There are two mechanisms thought to be responsible for anomalous transport. The first one, known as near wall conductivity, was first proposed by Morozov [25]. Near wall conductivity explains the anomalous transport as a result of electron collisions with the walls. Another mechanism, known as fluctuation induced transport, explains anomalous transport as a result of plasma oscillations [1, 3, 4].

The plasma in a Hall thruster is full of oscillations over a wide range of frequencies [1, 3]. These oscillations can interfere with the electronics onboard of the thruster, affect the location of the ionization and acceleration regions, change the divergence of the outgoing ion beam, affect the electron transport in the thruster and even extinguish the plasma discharge [1–3]. The equilibrium $\mathbf{E}_0 \times \mathbf{B}_0$ electron drift acts as the energy source for several different types of oscillations and instabilities present in the plasma inside a Hall thruster [3, 4, 11, 13, 27–29]. The equilibrium $\mathbf{E}_0 \times \mathbf{B}_0$ electron drift and the inhomogeneities in plasma density, magnetic field and temperature

are sources of gradient drift instabilities. [9, 11, 27]. Such instabilities are studied in Chapter 3. Special emphasis is given to study the effect of the full compressibility of the electron drift velocity. The gradient drift instabilities result in azimuthally propagating structures, known as spokes, that affect the plasma transport in Hall thrusters [11, 30, 31].

The interaction of the bulk plasma with the walls of a Hall thruster is another area of ongoing research [5, 7, 22, 32, 33]. The interaction of the plasma with the wall is not limited to the sputtering and secondary electron emission produced by collisions of high energy ions and electrons with the thruster walls. Oscillations are excited due to the closure of the plasma current to the dielectric walls of the thruster and the interaction of the bulk plasma with the sheath region that exists between the bulk plasma and the channel walls [33, 34]. A theory of the sheath instabilities in a Hall thruster plasma and how they affect the electron transport in a Hall thruster is presented in Chapter 4.

In order to better understand how anomalous transport originates in a Hall thruster computer simulations of the nonlinear behavior of the plasma are needed. The numerical codes used for the plasma simulation in a Hall thruster belong to four different categories, fully kinetic, particle-in-cell, hybrid or fluid [4, 35–39]. In Chapter 5, a physics model for the plasma in a Hall thruster is developed and computer simulations based on this model are presented. The nonlinear physics model of the Hall thruster plasma consists of a system of partial differential equations that describe the time evolution of plasma density, ion and electron velocities. The simulations are performed using BOUT++, which is a high performance framework for writing fluid and plasma computer simulations. BOUT++ uses finite differences and a variety of numerical integration solvers to evolve a system of partial differential equation [40–42]. It was originally developed by the Lawrence Livermore National Laboratory to study edge turbulence in Tokamaks [40]. The model presented in this dissertation is the first use of BOUT++ to study the plasma dynamics and anomalous transport in a Hall thruster.

CHAPTER 2

COLLECTIVE PHENOMENA, FLUCTUATIONS AND TRANSPORT IN PLASMA

2.1 Introduction

As discussed in the previous chapter, electric propulsion is the application of electric and magnetic fields to accelerate charged particles to a high velocity. The accelerated charged particles are produced by the ionization of a neutral propellant gas. The electrons and the ionized gas in the chamber of the thruster create what is known as a plasma. The behavior of this plasma is affected not only by the externally applied electric and magnetic fields but also by the fields generated by the motion of the charged particles in the plasma itself. This "collective" behavior is what distinguishes a plasma from a mere collection of charged particles [43]. The plasma is, on average, almost electrically neutral, that is, the electron and ion charge densities are almost equal, $n_e \approx Z\, n_i$. This condition, known as quasineutrality, is satisfied over distances longer than the distance over which the charges are (electrostatically) shielded. This distance is known as the Debye length [43] [1]. The different particle species in the plasma are also characterized by some energy distribution with each species having a generally different electron and ion temperature, T_e and T_i.

The main goal of this chapter is to familiarize the reader with the relevant concepts used in describing the motion of charged particles and the behavior of the plasma inside a Hall thruster.

[1] The Debye length, λ_D, is defined as $\lambda_D = \left(\frac{\varepsilon_0 T_e}{e^2 n_0}\right)^{1/2}$. It is discussed in Section 2.4.

2.2 Charged particle drifts

The behavior of the plasma is determined by the motion of its particles. In this section the motion of a single charged particle under the influence of electric and magnetic fields is studied. The force acting on a particle of charge q and that has a velocity, $\mathbf{v}$, due to an electric and magnetic field is given by the Lorentz force

$$\mathbf{F}_L = m\frac{d\mathbf{v}}{dt} = q\left(\mathbf{E} + \mathbf{v} \times \mathbf{B}\right). \tag{2.1}$$

Consider first the case where there is no electric field and the charged particle has a finite velocity perpendicular to the magnetic field. The force on a moving charged particle due to the magnetic field is a central force. This magnetic field force is then equal to the centripetal force on the charged particle (see Fig. 2.1)

$$\mathbf{F}_c \;=\; q\,\mathbf{v}_\perp \times \mathbf{B} = \frac{mv_\perp^2}{r}\hat{\mathbf{r}}. \tag{2.2}$$

The circular motion described by the charged particle under the central force due to the magnetic field has a radius ρ_c, known as gyroradius or Larmor radius and an angular frequency ω_c, known as cyclotron or gyro frequency, given by

$$\rho_c \;=\; \frac{mv_\perp}{q\,B} = \frac{v_\perp}{\omega_c}, \tag{2.3}$$

$$\omega_c \;=\; \frac{qB}{m}. \tag{2.4}$$

As seen from Eq. (2.2), the sense of gyration is a function of the charge of the particle, that is, positively and negatively charged particle gyrate in opposite directions. The Larmor radius also depends on the mass of the particles, with a heavier particle having a larger Larmor radius. Similarly, the Larmor radius is shorter when the magnetic field is larger. The center of the circular orbit is known as the guiding center. For slowly changing fields, the motion of the guiding center gives a good approximation for the average particle location, that is different from the guiding center by a distance of the order of the Larmor radius [43].

In the presence of both an electric and magnetic field, the equation of motion of the charged

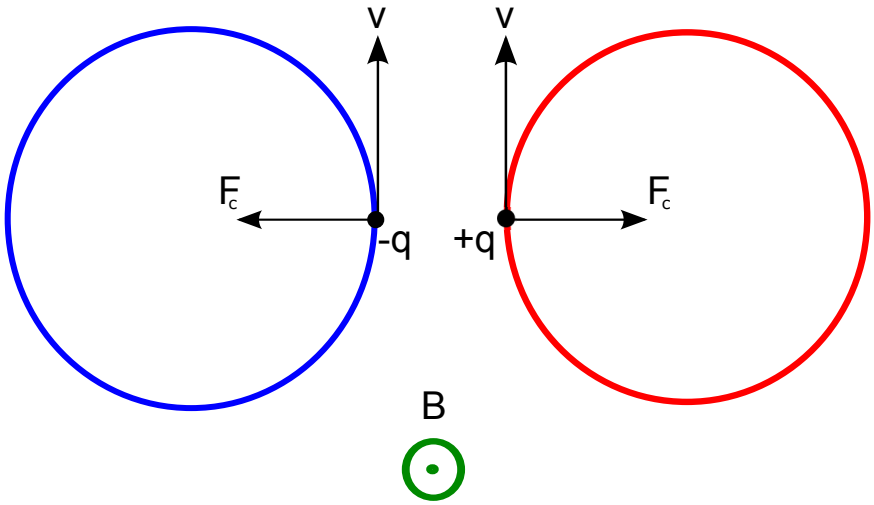

Figure 2.1: Motion of a charged particle in a magnetic field. The magnetic force $\mathbf{F}_c = q\mathbf{v} \times \mathbf{B}$ results in a circular motion with a gyro frequency $\omega_c = qB/m$ and radius given by the Larmor radius, $\rho_c = mv/qB$. Negatively charged particles (blue) gyrate in the opposite direction as the positively charged particles (red). The magnetic field is into the plane of the paper (green).

particle can be written as a first approximation as [2]

$$\mathbf{E}_\perp + \mathbf{v}_\perp \times \mathbf{B} = 0. \tag{2.5}$$

Solving this last equation, the particle velocity is obtained as

$$\mathbf{v} \;=\; \frac{\mathbf{E} \times \mathbf{B}}{B^2} \equiv \mathbf{v}_E. \tag{2.6}$$

The velocity calculated in Eq. (2.6), is known as the $\mathbf{E} \times \mathbf{B}$ drift velocity. This velocity is perpendicular to both the electric and the magnetic field. This velocity is the velocity of the guiding center of the particle during the drift motion and it is independent of the charge of the particle (positive charges drift in the same direction as negative charges). The drift arises due to the fact that the electric field accelerates the charged particle during one half of the orbital motion and decelerates the particle during the other half of the orbit, resulting in a net helical motion perpendicular to both the electric and the magnetic field [43]. Since the drift velocity $\mathbf{v}_E$ is perpendicular

[2] This is valid when the characteristic rate of change of the fields over time is much smaller than the cyclotron frequency.

to the electric field, it does not change the kinetic energy of the charged particle and does no work ($dU_k/dt \sim \mathbf{v} \cdot \mathbf{E} = 0$). A general picture of the drift motion can be seen in Fig. 2.2.

The $\mathbf{E} \times \mathbf{B}$ drift is an example of the more general force drift. When there is a force $\mathbf{F}$ on a charged particle and this force is perpendicular to the magnetic field, the charged particle will describe a helical motion with guiding center velocity given by

$$\mathbf{v}_{gc} = \frac{1}{q} \frac{\mathbf{F} \times \mathbf{B}}{B^2}. \tag{2.7}$$

The force drift velocity is generally dependent on the charge of the particle, meaning that, positive and negative charges drift in opposite directions. The $\mathbf{E} \times \mathbf{B}$ drift is the drift due to the electric field force, $F = qE$ and the charge dependance of this force cancels the charge dependence of the force drift, resulting in the $\mathbf{E} \times \mathbf{B}$ drift being independent of the charge overall. Other important guiding center drifts are due to the force that arises from a time varying electric field, known as polarization drift,

$$\mathbf{v}_{pol} = \frac{m}{qB^2} \frac{\partial \mathbf{E}}{\partial t}, \tag{2.8}$$

to the force from parallel gradients of the magnetic field, known as ∇B drift,

$$\mathbf{v}_{\nabla B} = \frac{m v_\perp^2}{2qB^3} \mathbf{B} \times \nabla B. \tag{2.9}$$

and from the curvature of the magnetic field lines, known as curvature drift

$$\mathbf{v}_R = \frac{v_{||}^2}{\omega_c} \mathbf{b} \times (\mathbf{b} \cdot \nabla) \mathbf{b}, \tag{2.10}$$

where $v_{||}$ and $\mathbf{b}$ are the velocity and the unit vector along the magnetic field.

2.3 Fluid description of plasma

The large amount of particles in a plasma makes it impractical to use the single particle picture to describe its behavior. It is then necessary to use some form of averaging over an ensemble of particles to describe the macroscopical properties of the plasma. The kinetic description of plasma is based on the plasma kinetic equation [44]. The plasma kinetic equation describes the evolution

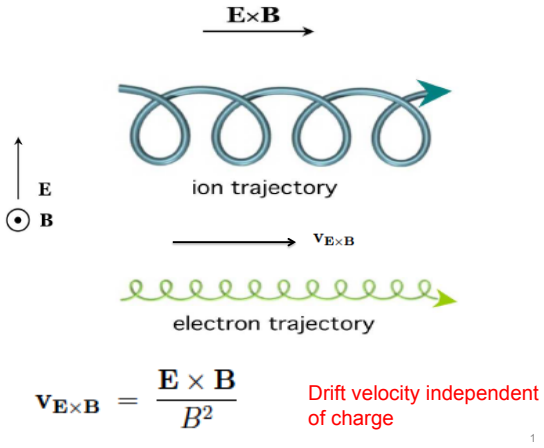

Figure 2.2: $\mathbf{E} \times \mathbf{B}$ drift of a charged particle. Electrons and ions drift in the same direction.

of the (macroscopic) plasma distribution function, $f = f(t, \mathbf{x}, \mathbf{v})$ [3]

$$\frac{df}{dt} = \frac{\partial f}{\partial t} + \mathbf{v} \cdot \frac{\partial f}{\partial \mathbf{x}} + \frac{q}{m} \left[\mathbf{E} + \mathbf{v} \times \mathbf{B}\right] \cdot \frac{\partial f}{\partial \mathbf{v}} = C(f). \tag{2.11}$$

The term on the right hand of the kinetic equation, that accounts for the close interactions between the particle species, is known as the collision operator [44]. The form of the collision operator is not generally simple and different forms of the collision operator are derived to study different phenomena [43, 45]. The kinetic equation (2.11) is an equation for the distribution function as a function of 6 (six) variables (three space and three velocity) plus time. The kinetic plasma description is complemented with the Maxwell equations for the electric and magnetic fields in the plasma

$$\nabla \cdot \mathbf{E} = \frac{\rho}{\varepsilon_0},\ \nabla \times \mathbf{E} = -\frac{\partial \mathbf{B}}{\partial t},\ \nabla \cdot \mathbf{B} = 0,\ \nabla \times \mathbf{B} = \mu_0 \mathbf{J} + \frac{1}{c^2} \frac{\partial \mathbf{E}}{\partial t},$$
$$\rho = \sum q_\alpha \int f_\alpha(t, \mathbf{x}, \mathbf{v}) d^3\mathbf{v},\ \mathbf{J} = \sum q_\alpha \int \mathbf{v} f_\alpha(t, \mathbf{x}, \mathbf{v}) d^3\mathbf{v} \tag{2.12}$$

The system of integral-differential equations (2.12) is rather difficult to solve even numerically. An alternative approach to study plasma phenomena is to use the moments of the distribution function.

[3] The macroscopic plasma distribution function is obtained from a smoothed average of the microscopic distribution function, $f = \langle f^m \rangle$, where $f^m = \sum_{i=1}^{N} \delta\left[\mathbf{x} - \mathbf{x}_i(t)\right] \delta\left[\mathbf{v} - \mathbf{v}_i(t)\right]$. The problem of calculating the average of the microscopic distribution function is a complicated one and it is beyond the scope and range of interest of this dissertation. For a very thorough description of this problem, the reader is referred to Ref. [44].

The generic moment of order j of the distribution function is defined as

$$\mathbf{M}_j(\mathbf{x},t) \equiv \int \mathbf{v}^j\, f(\mathbf{x},\mathbf{v},t)\, d^3\mathbf{v}. \tag{2.13}$$

The $j-th$ order moment is a tensor of rank j. These moments provide the average (expected) value of some physical quantity. The zeroth-order moment gives the particle density $n(\mathbf{x},t)$:

$$n(\mathbf{x},t) = \int f(\mathbf{x},\mathbf{v},t)\, d^3\mathbf{v}. \tag{2.14}$$

The first order moment gives the particle density flux $\mathbf{\Gamma} = n\,\mathbf{V}$:

$$n\mathbf{V} = \int \mathbf{v}\, f(\mathbf{x},\mathbf{v},t)\, d^3\mathbf{v}. \tag{2.15}$$

These two moments define the relations for the charge density and the current density

$$\rho = qn, \qquad \mathbf{J} = q\,n\,\mathbf{V}.$$

The second order moment or pressure tensor, can be calculated by defining $\mathbf{v}^{'} = \mathbf{v} - \mathbf{V}$ as

$$\mathbf{P} = \int M\,\mathbf{v}^{'}\mathbf{v}^{'}\, f(\mathbf{x},\mathbf{v},t)\, d^3\mathbf{v}^{'} = \mathbf{\Pi} + p\,\mathbf{1}, \tag{2.16}$$

where $\mathbf{\Pi}$ is the stress tensor and p is the scalar pressure ($\mathbf{1}$ is the unit tensor), defined as

$$\mathbf{\Pi} = \int M\,\left(\mathbf{v}^{'}\mathbf{v}^{'} - \frac{1}{3}\,v^{2'}\right)\, f(\mathbf{x},\mathbf{v},t)\, d^3\mathbf{v}^{'}, \tag{2.17}$$

$$p = \int \frac{1}{3}\,M\,v^{2'}\, f(\mathbf{x},\mathbf{v},t)\, d^3\mathbf{v}^{'}. \tag{2.18}$$

The third order moment of the distribution function is the energy flux $\mathbf{q}$, defined as

$$\mathbf{q} = \int \frac{1}{2}\,Mv^{2'}\,\mathbf{v}^{'}\, f(\mathbf{x},\mathbf{v},t)\, d^3\mathbf{v}^{'}. \tag{2.19}$$

In addition to the moments of the distribution function, the moments of the collision operator can be calculated. The first order moment of the collision operator defines the collisional frictional force as

$$\mathbf{F}_{coll} = \int M\mathbf{v}^{'}\, C(f)\, d^3\,\mathbf{v}^{'}. \tag{2.20}$$

The time evolution of the moments of the distribution function is calculated by taking the moments of the kinetic equation, Eq, (2.11). The zeroth-order moment of the kinetic equation yields the continuity equation or the equation of conservation of particle density

$$\frac{\partial n}{\partial t} + \nabla\cdot(n\,\mathbf{V}) = 0. \tag{2.21}$$

The first order moment of the kinetic equation gives the conservation of momentum equation

$$m\,n\left(\frac{\partial \mathbf{V}}{\partial t}+(\mathbf{V}\cdot\nabla)\,\mathbf{V}\right)-q\,n\,(\mathbf{E}+\mathbf{V}\times\mathbf{B})+\nabla p+\nabla\cdot\mathbf{\Pi}=\mathbf{F}_{coll}. \tag{2.22}$$

The second order moment of the kinetic equation gives the energy conservation equation

$$\frac{3}{2}\left(\frac{\partial p}{\partial t}+\nabla\cdot(p\,\mathbf{V})\right)+\mathbf{P}{:}\nabla\mathbf{V}+\nabla\cdot\mathbf{q}=W_{coll},^{4} \tag{2.23}$$

where W_{coll} defines the energy losses due to collisions (second order moment of the collision operator).

The set of equations (2.21)–(2.23) defines how the different macroscopic quantities change in plasma. These equations constitute the fluid description of the plasma and they will be used in the remainder of this dissertation [5].

2.4 Classical transport

As seen in the previous sections, the motion of a charged particle in the presence of electric and magnetic fields and neglecting interactions with other particles is governed by the Lorentz force. However, the exchange of momentum via collisions with other particles cannot be neglected and plays a very important role in the dynamics of plasma. Before proceeding further it is useful to take a look at the different collision processes that occur in plasma.

2.4.1 Collisions in plasmas

In a plasma, charged particles can interact with each other via Coulomb collisions and at the same time they can also interact via collisions with the neutral atoms. Collisions with neutrals can be elastic or inelastic.

The probability that a collision occurs is related to the effective cross section. Consider a thin slice filed with a neutral gas with some density n_n. This slice has an area of A and a thickness dx, so that the total number of neutral particles in the slice is $n_n A dx$. Considering the neutral particles

[4] For tensors $\mathbf{A}$ and $\mathbf{B}$, the double cross product $\mathbf{A}:\mathbf{B}$ is defined as $\mathbf{A}:\mathbf{B}=A_{ij}B_{ji}$.

[5] For a more thorough derivation and discussion of the plasma fluid equations the reader is referred to Refs. [44] and [45]

in the slice as spheres of cross-section σ, the total area occupied by these neutrals is $\sigma n_n A dx$. Now, consider an incoming flux of particles I. The probability that a particle from the incoming flux be stopped (collides with) by a neutral particle in the slice is the area of the neutral particles in the slice divided by the total area of the slice [1]

$$P = \frac{Area_{neutrals}}{Area_{slice}} = \sigma n_n dx. \tag{2.24}$$

This way, the change over dx of the incoming particle flux I is proportional to the flux multiplied by the probability that a particle from the incoming flux is stopped by a neutral in the slice

$$\frac{dI(x)}{dx} = -I\sigma n_n, \tag{2.25}$$

$$I(x) = I_0 e^{-\sigma n_n x} = I_0 e^{-x/\lambda}. \tag{2.26}$$

In this last equation, the quantity λ is known as the mean free path, which is the mean distance a particle will travel before a collision, [43], as illustrated in Fig. 2.3

$$\lambda = \frac{1}{n_n \sigma}. \tag{2.27}$$

The mean time between collisions is thus the distance traveled by a particle before a collision divided by its mean velocity

$$\tau_{coll} = \frac{1}{n_n \sigma \bar{v}}, \tag{2.28}$$

which defines a collision frequency of

$$\nu = \frac{1}{\tau_{coll}} = n_n \sigma \bar{v}. \tag{2.29}$$

The electron-neutral collision frequency in a plasma is given by Eq. (2.29) as [1]

$$\nu_{en} = \sigma_{en}(T_e) n_n \sqrt{\frac{8T_e}{\pi m_e}}, \tag{2.30}$$

where σ_{en} is the effective electron-neutral scattering cross-section. For Xe, the gas most often used as propellant in Hall thrusters, σ_{en} is given by [1]

$$\sigma_{en}(T_e) = 6.6 \times 10^{-19} \left[\frac{\frac{T_e}{4} - 0.1}{1 + \left(\frac{T_e}{4}\right)^{1.6}} \right] [m^2]. \tag{2.31}$$

Using Eq. (2.31) in Eq. (2.30) for typical values of electron temperature and neutral density results in an electron-neutral collision frequency of 10^5–10^6 s^{-1} (see Table 1.1).

Inelastic collisions between electrons and neutrals are responsible for ionization and excitation processes of neutral particles in a Hall thruster [1]. The ion production rate is given by [6] [1]

$$\frac{dn_i}{dt} = n_n n_e \left\langle \sigma_i v_e \right\rangle, \tag{2.32}$$

where σ_i is the ionization cross-section and $\langle \sigma_i v_e \rangle$ is the reaction rate (the ionization cross-section averaged over all electron velocities).

The excited neutrals production rate is similarly defined as [1]

$$\frac{dn^*}{dt} = \sum_j n_n n_e \left\langle \sigma_* v_e \right\rangle, \tag{2.33}$$

where σ_* is the excitation cross-section, $\langle \sigma_* v_e \rangle$ is the reaction rate for excited state j, and the summation is over all excited states j.

Another important type of collisions in a Hall thruster are charge exchange collisions (CXE). These collisions describe the resonant charge transfer between neutral atoms and ions [1]. In CXE collisions no kinetic energy is exchanged between the colliding particles. These collisions are also characterized by having large cross-sections and they can occur over long distances [1]. Since the ions are generally more energetic than the neutral particles, CEX collisions result in energetic neutrals and cold ions. CEX collisions are thought to play an important role in wall erosion and sputtering which can affect the lifetime and efficiency of the thruster [1, 2].

Charged particles can interact with each other via Coulomb collisions. The electron-ion and electron-electron Coulomb collision frequencies are given by (in SI) [46]

$$\nu_{ei} = 2.9 \times 10^{-12} \frac{n_e \ln \Lambda}{T_e^{3/2}}, \tag{2.34}$$

$$\nu_{ee} = 5.0 \times 10^{-12} \frac{n_e \ln \Lambda}{T_e^{3/2}}, \tag{2.35}$$

where $\ln \Lambda$ is the Coulomb logarithm [46]

$$\ln \Lambda = 23 - \frac{1}{2} \ln \left(\frac{10^{-6} n_e}{T_e^3} \right). \tag{2.36}$$

The electron-ion and electron-electron collision frequencies given by Eqs. (2.34)-(2.35) are similar, but due to the ions being more massive than the electrons, the energy transferred between

[6] This equation is not to be confused with the continuity equation.

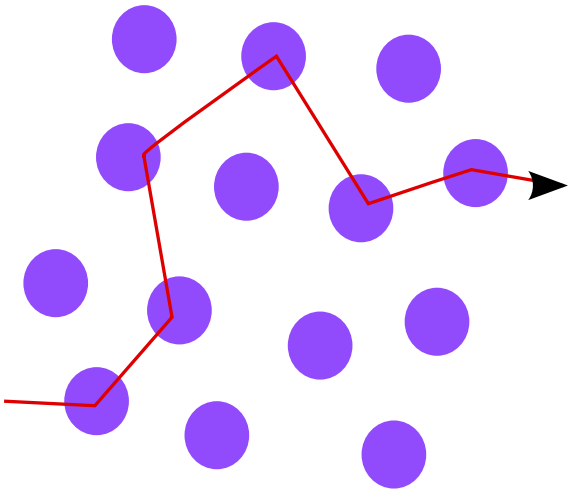

Figure 2.3: When particles collide with one another, they are displaced from their original trajectory. The mean distance covered by a particle between two successive collision events is known as mean free path.

electrons and ions after each collision is small and electrons do not thermalize rapidly with the ions [1].

The ion-ion collision frequency is given by [46] as

$$\nu_{ii} = Z^4 \left(\frac{m_e}{m_i}\right)^{1/2} \left(\frac{T_e}{T_i}\right)^{3/2} \nu_{ee}. \tag{2.37}$$

In a Hall thruster, the electron-neutral collision frequency is larger than the electron-electron and the electron-ion collision frequencies, which are larger than the ion-ion collision frequency.

Momentum exchange collisions between electrons and other particles in the plasma are responsible for resistivity and for electron heating (Joule's heating) [1]. These momentum exchange collisions are also important in transport phenomena in plasma such as diffusion and mobility as is discussed in the next sections.

2.4.2 Transport in absence of magnetic fields

Assuming steady-state, the fluid momentum equation taking into account (momentum exchange) collisions, can be written as

$$e\, n\, \mathbf{E} - \nabla p - m\, n\, \nu\, \mathbf{v} = 0. \tag{2.38}$$

Solving Eq. (2.38) for the velocity by assuming that the plasma is isothermal, such that $\nabla p = T\,\nabla n$, results in [43]

$$\mathbf{v} = \frac{e}{m\,\nu}\,\mathbf{E} - \frac{T}{m\,\nu}\,\frac{\nabla n}{n}. \tag{2.39}$$

Equation (2.39) states that the velocity is proportional to both the density gradients and the electric field. The coefficients of proportionality are known respectively as mobility and diffusion coefficients:

$$\mu \equiv \frac{e}{m\nu} \quad [m^2/Vs] \tag{2.40}$$

$$D \equiv \frac{T}{m\,\nu} \quad [m^2/s]. \tag{2.41}$$

Particle diffusion can be interpreted using a random walk model. Particles follow straight line trajectories before changing their trajectories after a collision event. The mean distance covered by a particle between collisions is the mean free path while the direction in which the particle is scattered after a collision is random. The diffusion coefficient can then be expressed as $D = \delta^2/\tau$, where δ is the average distance travelled by a particle between collisions (the mean free path) and τ is the time between collisions, that is, the inverse of the collision frequency, $\tau = 1/\nu$ [43]. Since the motion of the particles is thermal the diffusion coefficient is

$$D = \frac{\delta^2}{\tau} = \left\langle v^2 \right\rangle \frac{\tau^2}{\tau} = \frac{T}{m\,\nu}. \tag{2.42}$$

When an electric field exists, a charged particle is accelerated in the direction of the electric field. The electric field provides a bias in the motion of the charged particle such that the mean displacement is not exactly zero, $\langle \Delta \mathbf{x} \rangle \neq 0$ [47]. The mean velocity of the charged particle is

$$\langle v \rangle = \frac{qE}{m}\tau = \frac{qE}{m\nu},$$

from which the mobility is obtained as [47]

$$\mu = \frac{q}{m\nu}. \tag{2.43}$$

The mobility and the diffusion coefficients are related by the Einstein relation [43]

$$\mu = \frac{eD}{T}. \tag{2.44}$$

2.4.3 Transport across magnetic fields

When a magnetic field is present, the transport of particles in the direction perpendicular to the field is reduced because the magnetic field constrains the perpendicular displacement of the particles. A charged particle is said to be magnetized if the particle has to undergo many gyrations between collisions and unmagnetized otherwise. Particle motion can be characterized by the Hall parameter, defined as

$$\Omega_H = \frac{\omega_c}{\nu} = \omega_c \tau_{coll}. \tag{2.45}$$

For $\Omega_H >> 1$, the particle is magnetized and for $\Omega_H << 1$, it is unmagnetized.

In presence of a magnetic field, the mobility can be derived by using the fluid equation of motion [43]

$$e\, n\, (\mathbf{E} + \mathbf{v} \times \mathbf{B}) - \nabla p - m\, n\, \nu\, \mathbf{v} = 0. \tag{2.46}$$

Assuming that the plasma is isothermal and that the magnetic field is in the **z**-direction, the x and y components of the velocity can be written as

$$v_x = \frac{e}{m\nu} E_x - \frac{T}{m\nu} \frac{\partial n}{\partial x} + \frac{eB_z}{m\nu} v_y, \tag{2.47}$$

$$v_y = \frac{e}{m\nu} E_y - \frac{T}{m\nu} \frac{\partial n}{\partial y} - \frac{eB_z}{m\nu} v_x. \tag{2.48}$$

Solving the equations for v_x and v_y and using the free diffusion and mobility coefficients from Eqs. (2.40)–(2.41) yields

$$\begin{aligned}
v_x &= \frac{\mu}{1+\omega_c^2\tau_{coll}^2} E_x - \frac{D}{1+\omega_c^2\tau_{coll}^2} \frac{1}{n} \frac{\partial n}{\partial x} + \frac{\omega_c^2\tau_{coll}^2}{1+\omega_c^2\tau_{coll}^2} \frac{E_y}{B_z} - \frac{D\omega_c\tau_{coll}}{1+\omega_c^2\tau_{coll}^2} \frac{1}{n} \frac{\partial n}{\partial y}, \\
v_y &= \frac{\mu}{1+\omega_c^2\tau_{coll}^2} E_y - \frac{D}{1+\omega_c^2\tau_{coll}^2} \frac{1}{n} \frac{\partial n}{\partial y} - \frac{\omega_c^2\tau_{coll}^2}{1+\omega_c^2\tau_{coll}^2} \frac{E_x}{B_z} + \frac{D\omega_c\tau_{coll}}{1+\omega_c^2\tau_{coll}^2} \frac{1}{n} \frac{\partial n}{\partial x}, \\
\mathbf{v} &= \mu_\perp \mathbf{E} - D_\perp \frac{\nabla n}{n} + \frac{\omega_c^2\tau_{coll}^2}{1+\omega_c^2\tau_{coll}^2} \left(\frac{\mathbf{E} \times \mathbf{B}}{B^2} - \frac{T_e}{en} \frac{\nabla n \times \mathbf{B}}{B^2} \right).
\end{aligned} \tag{2.49}$$

From the velocity (2.49) the mobility and diffusion coefficient parallel to the density gradient

and the electric field are given by [7]

$$\mu_\perp \equiv \frac{\mu}{1+\omega_c^2\tau_{coll}^2} \quad [m^2/Vs] \tag{2.50}$$

$$D_\perp \equiv \frac{D}{1+\omega_c^2\tau_{coll}^2} \quad [m^2/s]. \tag{2.51}$$

For the case of low Hall parameter (unmagnetized particles), Eqs. (2.50)–(2.51) tend to Eqs. (2.40)–(2.41). For large Hall parameters, Eqs. (2.50)–(2.51) reduce to

$$\mu_\perp \equiv \frac{\nu}{\omega_c B}, \tag{2.52}$$

$$D_\perp \equiv \frac{T\nu}{m\omega_c^2}. \tag{2.53}$$

The diffusion and mobility coefficients across the magnetic field are proportional to the inverse of the square of the magnetic field, as can be seen Eqs. (2.52) and (2.53).

The perpendicular mobility and diffusion coefficients can be obtained from a simple random walk picture. The main difference with respect to the picture without magnetic fields is that in the presence of a magnetic field, the mean square displacement of the particles after a collision is of the order of the square of the Larmor radius, that is $\delta^2 \sim \rho_c^2$. The diffusion coefficient is

$$D_\perp = \frac{\delta^2}{\tau} = \frac{\langle v^2\rangle}{\omega_c^2}\frac{1}{\tau_{coll}} = \frac{T}{m}\frac{\nu}{\omega_c^2}. \tag{2.54}$$

The mobility across the magnetic field is calculated as

$$\begin{aligned} v_\perp = \frac{m\langle v_{E\times B}\rangle}{qB}\frac{1}{\tau_{coll}} &= \frac{m}{qB}\left(\frac{E}{B}\right)\frac{1}{\tau_{coll}} = \mu_\perp E, \\ \mu_\perp &= \frac{\nu}{\omega_c B}. \end{aligned} \tag{2.55}$$

In a Hall thruster, with typical parameters of neutral density $10^{18} - 10^{20}$ m^{-3}, $T_e = 20$ eV, the electron-neutral collision frequency is around 10^6/s, (the ion-electron collision frequency is around one order of magnitude smaller). The cyclotron frequency is around 10^9 Hz and the Hall parameter is around 400 [1], meaning that the classical mobility should be of about 0.01–0.1 m^2/Vs.

In the acceleration region, the mobility has been observed to have a value of around 10 m^2/Vs, which is three orders of magnitude higher than the value predicted by classical mobility. Classical

[7] The component of the velocity parallel to the electric field and the density gradient, which are both perpendicular to the magnetic field, define the Pedersen current. The component of the velocity perpendicular to the electric field, the density gradient and the magnetic field is responsible for the Hall current [43]

mobility predicts an electron current that is proportional to $1/B^2$, while experimentally a dependence on $1/B$ has been observed [20]. The fact that the experimentally observed mobility and electron current density in the acceleration region of a Hall thruster are significantly higher than the ones predicted by the classical theory is referred to as anomalous mobility (transport).

2.4.4 Near wall conductivity

Electron collisions with the walls have the same effect as the collisions with neutrals or other plasma species. The channel width in the chamber of a Hall thruster is much smaller than the mean free path for electron-neutral collisions ($\sim$2-3 cm vs $\sim$1 m), therefore the electron has a greater chance of colliding with the wall before colliding with another neutral. The transport due to electron collisions with the Hall thruster walls is known as near-wall conductivity [22]. The theory of near wall conductivity was developed by Morozov starting in the 1960's [17, 22].

For an electron, assuming that there is a wall at z =0 and in the presence of a magnetic field in the z-direction, the non specular collisions with the walls are responsible for the electron current. If the collision with the wall is specular, the sign of $v_{\parallel}$ (along the magnetic field) will change but v_x and v_y will be the same as before the collision. In a Hall thruster, the presence of an axial electric field [8] makes possible non specular collisions with the wall [2, 4] and the electron can change position in the plane $x - y$, being able to move in the axial direction as can be seen in Fig. 2.4.

An electron wall collision frequency can be estimated to be proportional to the average electron velocity $\bar{v}_e$ and the distance between walls h,

$$\nu_{ew} \sim \frac{\bar{v}_e}{h}.$$

The total number of electrons that will collide with the wall is proportional to the fraction of electrons that can overcome the sheath potential between the bulk plasma and the walls. Assuming that the electrons follow a Maxwell distribution, the effective electron wall collision frequency is then [4]

$$\nu_{ew} = \frac{\bar{v}_e}{h} \exp\left(-\frac{e\phi_s}{T_e}\right), \tag{2.56}$$

[8] Additionally, wall roughness contributes to non specular collisions [2].

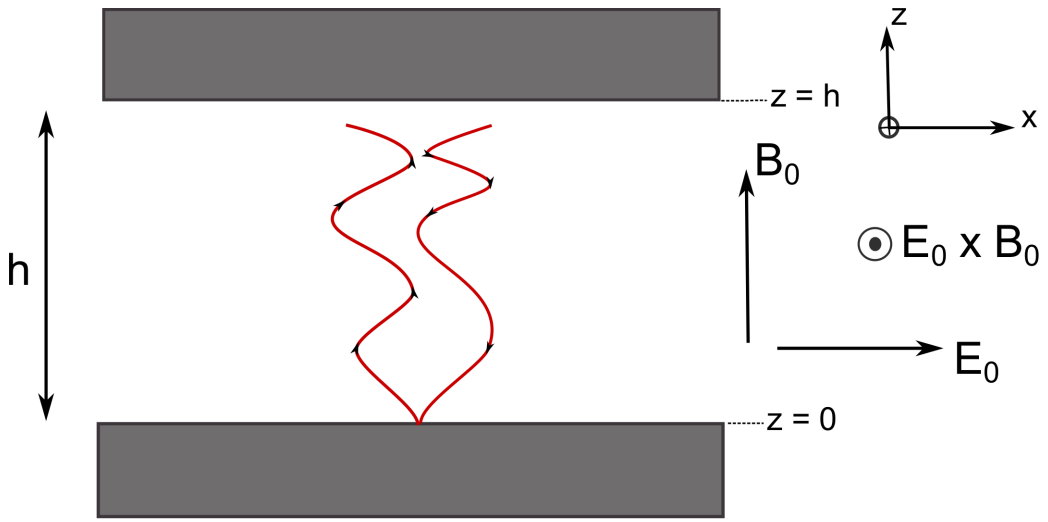

Figure 2.4: Simple illustration of near wall conductivity. When electrons collide with the wall they are displaced from their trajectories and a net axial transport arises. The axial displacement is due mainly to the presence of the axial electric field [4] with additional contribution due to roughness at the wall surface [2]. Figure adapted from Ref. [2].

where ϕ_s is the sheath potential given by [1]

$$\phi_s = \frac{T_e}{e} \ln\left(\sqrt{\frac{m_i}{2\pi m_e}}\right). \tag{2.57}$$

For a Hall thruster, the effective electron wall collision frequency (2.56) is around 10^5 s^{-1}, which is lower than the electron-neutral collision frequency.

Since only electrons with high enough energy can climb the sheath potential, the fast electrons found in measurements of the electron energy distribution seem to be a proof of this mechanism. The results from these experiments are not universally agreed upon [20], since the probes can cause disturbances in the discharge channel and also because obtaining the correct electron energy distribution can be very complicated [20] and the assumption that the energy distribution of the electrons is may be incorrect [48].

Another problem is that not all electrons striking the wall will have elastic scattering, since they can recombine with ions also hitting the wall or since they have high energy, they may induce secondary electron emission from the walls. This SEE can have significant importance in the cross-field transport process and increase near wall conductivity [48].

In general, the sheath potential that repels the electron has to be taken into account to precisely

know the fraction of electrons that actually collide with the wall, but the sheath potential is coupled to the SEE from the wall, so the problem of knowing the exact behavior of the electrons hitting the wall is a complex problem [48].

In conclusion, the role of the walls in the transport process in a Hall thruster is the subject of a heated debate. It is not clear if they will contribute via near-wall conductivity (Eqs. (2.56)) or by enhancing or damping the fluctuation-induced mobility in some way. Additional effects of the plasma wall interaction in Hall thrusters are presented and discussed in Chapter 4.

2.5 Collective behavior and waves in plasma

Plasma is a state of matter composed of a quasineutral gas of charged and neutral particles that exhibits collective behavior [43]. In a plasma a charged particle can interact with many other charged particles via their electromagnetic fields [44]. A very important consequence of the collective behavior of plasma is the shielding of the electric field generated by a charge perturbation over certain distance. This phenomenon is known as Debye shielding.

2.5.1 Debye shielding

The distance beyond which the electric field of any particular charged particle in a plasma is shielded by the other particles is known as the Debye length. Consider the potential around a test charged particle in a plasma. The electrostatic potential can be calculated from Poisson's equation, where the charge density around the charge particle is given by the polarization charge density and the (point) charge of the test particle [44]

$$\nabla^2\phi = -\frac{\rho_{pol}(\mathbf{x}) + q_t\delta(\mathbf{x}-\mathbf{x}_t)}{\varepsilon_0}. \tag{2.58}$$

The density of charged particles of charge q_α and temperature T_α follows the Boltzmann distribution

$$n_\alpha(\mathbf{x}) = n_0 e^{-q_\alpha\phi(\mathbf{x})/T_\alpha}. \tag{2.59}$$

The potential energy of the particles due to the test charged particle is smaller than their thermal energy (except close to the test particle) such that the particle density can be expanded as

$$n_\alpha \approx n_{0\alpha}\left(1 - \frac{q_\alpha\phi}{T_\alpha}\right), \tag{2.60}$$

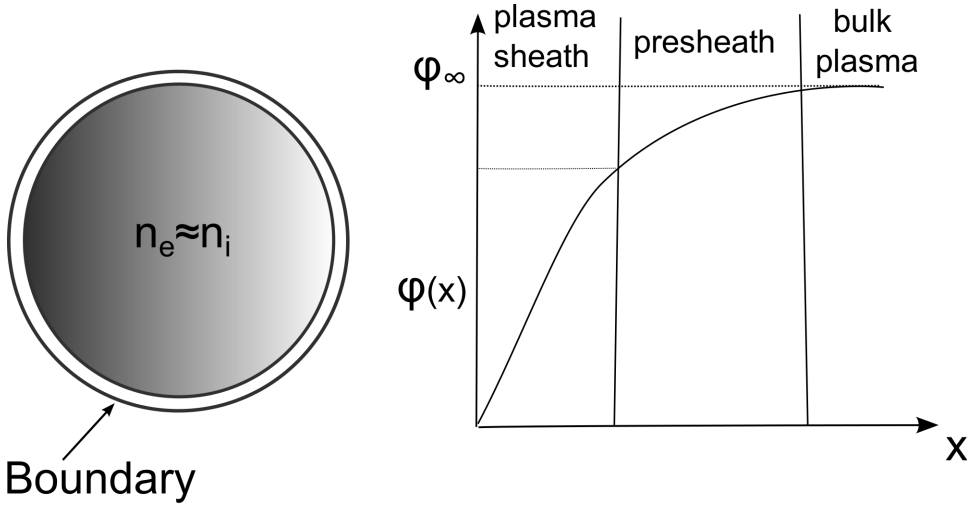

Figure 2.5: Right: Plasma region and its boundary. Left: Potential for plasma in contact with a boundary. Shown are the bulk plasma region, the presheath and the sheath regions.

resulting in a polarization charge density of

$$\rho_{pol} = -\sum_{\alpha=e,i} \frac{q_\alpha \phi}{T_\alpha}. \tag{2.61}$$

Equation 2.58 thus becomes

$$\left(\nabla^2 - \frac{1}{\lambda_D^2}\right)\phi = -\frac{q_t \delta(\mathbf{x}-\mathbf{x}_t)}{\varepsilon_0}, \tag{2.62}$$

whose solution is [44]

$$\phi(\mathbf{x}) = \frac{q_t\, e^{|\mathbf{x}-\mathbf{x}_t|/\lambda_D}}{|\mathbf{x}-\mathbf{x}_t|}, \tag{2.63}$$

where λ_D is the Debye length, given by [44]

$$\frac{1}{\lambda_D^2} \equiv \sum_{\alpha=e,i} \frac{n_{0\alpha} q_\alpha^2}{\varepsilon_0 T_\alpha} = \frac{n_{0e} e^2}{\varepsilon_0 T_e} + \frac{n_{0i} Z_i^2 e^2}{\varepsilon_0 T_i}. \tag{2.64}$$

From Eq. (2.63), the potential due to a charge perturbation is shielded out for distances longer than the Debye length.

2.5.2 Plasma sheaths

A plasma should be such that it extends over a region much larger than the Debye length. The plasma boundaries play an important role since particles and energy can go into or out of the plasma

through these boundaries. For this reason, understanding boundary effects is key to understanding the behavior of any plasma system.

Consider a plasma and its boundary, as shown in Fig. 2.5. The ion current density to the boundary can be given as a first approximation as $J_i = en_i v_i$, where n_i and v_i are the ion density and velocity and only single charged ions are assumed for simplicity. In a similar fashion, the electron current to the boundary can be given as a first approximation as $J_e = en_e v_e$, where n_e and v_e are the electron density and velocity. The ratio of electron and ion current densities is then (assuming quasineutrality)

$$\frac{J_e}{J_i} = \frac{en_e v_e}{en_e v_e} = \frac{v_e}{v_i}. \tag{2.65}$$

Assuming that the ion and electron velocities are the thermal velocities, this ratio becomes

$$\frac{J_e}{J_i} = \frac{v_e}{v_i} = \sqrt{\frac{T_e}{T_i}}\sqrt{\frac{m_i}{m_e}}. \tag{2.66}$$

Since the ions are much more massive than the electrons, the ion temperature would need to be orders of magnitude higher than the electron temperature to keep a balance between the ion and electrons current to the boundary. Since this conditions is generally not satisfied, it should be impossible to maintain quasineutrality in the plasma since electrons would leave the plasma at a much higher rate than the ions. If electrons leave the plasma much faster than the ions, there would be a net positive charge in the plasma that would create a potential gradient such that it would counter the electrons from leaving and maintain quasineutrality. This potential is a direct consequence of the different electron and ion velocities and would appear in the boundaries of the plasma (for example, near the channel walls and the electrodes in a Hall thruster). This region is known as the plasma sheath.

Consider a plasma in contact with a boundary as shown in Fig. 2.5. This plasma has three regions, the bulk plasma, a sheath region and a transition region known as presheath. The electrons density follows the Boltzmann distribution,

$$n_e(x) = n_\infty \exp\left(\frac{e\left(\phi_\infty - \phi(x)\right)}{T_e}\right), \tag{2.67}$$

where the quantities with the ∞ subscript correspond to the bulk plasma region ($x \to \infty$).

Neglecting ion temperature effects and single charged ions, the ion velocity is given by the conservation of energy,

$$\frac{1}{2}m_i v_i(x)^2 + e\phi(x) = \frac{1}{2}m_i v_{i\infty}^2 + e\phi_\infty. \tag{2.68}$$

The potential variation is such that the ions are accelerated towards the sheath to counter the outgoing electron flux. In steady state, the ion flux is conserved, such that

$$n_i(x)v_i(x) = n_{i\infty}v_{i\infty}. \tag{2.69}$$

Using Eqs. (2.68) and (2.69), the ion density is given as [44]

$$n_i(x) = \frac{n_\infty}{\sqrt{1 + \frac{2e}{m_i v_{i\infty}^2}\left(\phi_\infty - \phi(x)\right)}}. \tag{2.70}$$

Poisson's equation can then be written using Eqs. (2.67) and (2.70) as

$$\frac{d^2\phi}{dx^2} = -\frac{en_\infty}{\varepsilon_0}\left[\frac{1}{\sqrt{1 + \frac{2e}{m_i v_{i\infty}^2}\left(\phi_\infty - \phi(x)\right)}} - \exp\left(\frac{e\left(\phi_\infty - \phi(x)\right)}{T_e}\right)\right]. \tag{2.71}$$

Assuming that $2e\left(\phi_\infty - \phi(x)\right)/m_i v_{i\infty}^2 \ll 1$ and $e\left(\phi_\infty - \phi(x)\right)/T_e \ll 1$, Poisson's equation reduces to [44]

$$\frac{d^2\left(\phi_\infty - \phi(x)\right)}{dx^2} = \frac{e^2 n_\infty}{\varepsilon_0}\left(1 - \frac{T_e}{m_i v_{i\infty}}\right). \tag{2.72}$$

Since the potential is a monotonic function of x, the proper condition for sheath formation becomes from Eq. (2.72) [44]

$$v_{i\infty}^2 \geq \frac{T_e}{m_i} = c_s^2. \tag{2.73}$$

The criterion in Eq. (2.73) is known as the Bohm criterion. Bohm criterion states that the ions must enter the sheath with a velocity of at least the ion sound velocity [9] in order to have a stable (monotonic) sheath potential behavior [1]. Another form to interpret the Bohm criterion is that the charge density must decrease as the potential increases in x [44].

Using the Bohm criterion, the ion current density to the sheath is given by [44]

$$J_i = en_\infty c_s, \tag{2.74}$$

while the electron current density is given by [44]

$$J_e = -\frac{1}{4}en_\infty\sqrt{\frac{8T_e}{\pi m_e}}\exp\left(-\frac{e\phi_\infty}{T_e}\right). \tag{2.75}$$

[9] The ion sound velocity is discussed in the next section.

From Eqs. (2.74)–(2.75), the potential at which the plasma will self-bias in order to equilibrate the ion and electron currents ($J_i + J_e = 0$), known as floating potential, is given by

$$\phi_\infty = \frac{T_e}{e} \ln \sqrt{\frac{m_i}{2\pi m_e}}. \tag{2.76}$$

The effect of perturbations of the current to the sheath is studied further in Chapter 4.

2.5.3 Waves in plasma

Consider a plasma where the electrons are displaced with respect to a homogenous ion background. The plasma response is to create an electric field (due to the charge separation) that tries to restore the electrons to their original equilibrium position. Because of the finite inertia of the electrons, they do not return to their exact equilibrium position, but oscillate around it with certain frequency, known as plasma frequency [43]. This motion is akin to the harmonic motion of a mass attached to a spring around some equilibrium position. In the plasma case the restoring force is provided by the electric field

$$\frac{d^2\delta x}{dt^2} = -\frac{e\delta E}{m_e} = -\frac{e^2 n_{0e}}{\varepsilon_0 m_e}\delta x, \tag{2.77}$$

$$\omega_{pe}^2 \equiv \frac{e^2 n_{0e}}{\varepsilon_0 m_e}. \tag{2.78}$$

The plasma frequency can also be calculated using the plasma fluid equations. Since it is assumed that the ions are not moving, the only equations of interests are the electron continuity and momentum equations. For a cold, unmagnetized plasma, the electron continuity and momentum equations reduce to

$$\begin{aligned} \frac{\partial n_e}{\partial t} + \nabla \cdot (n_e \mathbf{u}_e) &= 0, \\ m\, n \left(\frac{\partial \mathbf{u}_e}{\partial t} + (\mathbf{u}_e \cdot \nabla)\, \mathbf{u}_e \right) &= -e\, n \mathbf{E}. \end{aligned}$$

The different quantities, $\mathbf{E}$, $\mathbf{u}_e$ and n_e, can be expressed as the sum of some equilibrium quantity plus some (small) perturbation around their equilibrium values,

$$\mathbf{E} = \mathbf{E}_0 + \mathbf{E}_1,\ \mathbf{u}_e = \mathbf{u}_{e0} + \mathbf{u}_{e1},\ n_e = n_{e0} + n_{e1}. \tag{2.79}$$

Since it is assumed that the electrons are initially at rest and then they are displaced, the equilibrium electric field $\mathbf{E}_0$, and the equilibrium electric velocity $\mathbf{u}_{e0}$ are zero. Substituting the expansion

for the plasma parameters, Eq. (2.79), into the electron continuity and momentum equation and keeping only the terms up to the order of the perturbations results in

$$\begin{aligned} \frac{\partial n_{e1}}{\partial t} + n_{e0}\nabla \cdot \mathbf{u}_{e1} &= 0, \\ m_e n_{e0}\frac{\partial \mathbf{u}_{e1}}{\partial t} &= -en_{e0}\mathbf{E}_1 = en_0\nabla\phi_1. \end{aligned} \tag{2.80}$$

The electrostatic potential is due to the charge separation between electrons and ions and satisfies Poisson's equation

$$\nabla^2\phi_1 = \frac{e\, n_{e1}}{\varepsilon_0}. \tag{2.81}$$

The equations for the perturbed plasma parameters are linear differential equations with constant parameters [10], which allows to write the time and space dependence of these parameters as proportional to $\exp\, i(\mathbf{k}\cdot\mathbf{r} - \omega t)$, that is $A_1 = A_1\, \exp\, i(\mathbf{k}\cdot\mathbf{r} - \omega t)$, where $\mathbf{k}$ is the wavevector and ω is the (angular) frequency. With this representation, the time and space derivatives can be replaced by multiples of the frequency and the wavevector, $\partial/\partial t \rightarrow -i\omega$ and $\nabla \rightarrow i\mathbf{k}$. The system of linear differential equations (2.80) and (2.81) reduces to the system of algebraic equations

$$-i\omega n_{e1} + in_{e0}\mathbf{k}\cdot\mathbf{u}_{e1} = 0, \tag{2.82}$$

$$-i\omega m_e \mathbf{u}_{e1} = ien_{e0}\mathbf{k}\phi_1, \tag{2.83}$$

$$-k^2\phi_1 = \frac{en_{e1}}{\varepsilon_0}. \tag{2.84}$$

Solving the system in Eq. (2.84) for the frequency, known as plasma frequency, gives

$$\omega \equiv \omega_{pe} = \left(\frac{e^2 n_{e0}}{\varepsilon_0 m_e}\right)^{1/2}. \tag{2.85}$$

The inverse of the plasma frequency is the time it takes the plasma to respond to changes in potential [43]. Similar to the (electron) plasma frequency, an ion plasma frequency can be defined as

$$\omega_{pi} = \left(\frac{e^2 n_{i0}}{\varepsilon_0 m_i}\right)^{1/2}. \tag{2.86}$$

[10] The parameters are assumed constant since their characteristic length of variation is longer than the characteristic lengths of the oscillations.

This ion plasma frequency defines the time scale of the ion response to perturbations in the plasma. Since the lightest ion (H^+) is 1836 times heavier than one electron, the ions respond to perturbations in the plasma much slower than electrons.

Another important type of oscillations is related to the inertial ion response coupled with a finite electron temperature. The ion continuity and momentum equations are

$$\begin{aligned} \frac{\partial n_1}{\partial t} + \nabla \cdot (n_i \mathbf{v}_i) &= 0, \\ m_i\, n_i \left(\frac{\partial \mathbf{v}_i}{\partial t} + (\mathbf{v}_i \cdot \nabla)\, \mathbf{v}_i \right) &= e\, n_i \mathbf{E}. \end{aligned}$$

Assuming small perturbations of the equilibrium plasma parameters and an electrostatic electric field, the linearized form of the ion continuity and momentum equations becomes

$$-i\omega m_i n_{i0} \mathbf{v}_{i1} = -e n_{0i} \mathbf{k} \phi_1 - i\mathbf{k} n_{i1} T_i, \tag{2.87}$$

$$-i\omega n_{i1} + i n_{0i} \mathbf{k} \cdot \mathbf{v}_{i1} = 0. \tag{2.88}$$

The electrons, due to their small mass compared to the ions are assumed to respond instantaneously and the electron momentum equation (2.80) gives, after adding the electron pressure term $p_e = n_e T_e$, [11]

$$0 = ie n_{e0} \mathbf{k} \phi_1 - i\mathbf{k} n_{e1} T_e. \tag{2.89}$$

Assuming quasineutrality $n_e = n_i$ and using Eqs. (2.87)–(2.88) for the ions and Eqs. (2.82) and (2.89) for the electron momentum, the dispersion relation for the waves in the plasma becomes

$$\omega^2 = k^2 \left(\frac{T_e + T_i}{m_i} \right) = k^2 c_s^2. \tag{2.90}$$

The velocity c_s in Eq. (2.90) is known as the ion sound velocity and these waves are known as ion sound waves. As mentioned before, in a Hall thruster the electron temperature is higher than the ion temperature ($T_e \gg T_i$), and the ion sound velocity from Eq. (2.90) becomes

$$c_s^2 = \frac{T_e}{m_i}. \tag{2.91}$$

The effect of the electron equilibrium $\mathbf{E}_0 \times \mathbf{B}_0$ drift on the ion sound waves in Hall thruster plasma is studies in Chapter 4.

[11] From this equation the perturbed electron density is given by the Boltzmann formula, $n_{e1} = n_{0e} \frac{e\phi_1}{T_e}$.

Two types of plasma oscillations have been discussed so far, oscillations that arise due to the inertial response of the electrons plasma electron oscillations with $\omega = \omega_{pe}$, and ion sound waves that arise when considering the effects of finite plasma temperature and the inertia of the ions. In studying these oscillations the magnetic field has so far not been taken into account. Consider now the high frequency electron longitudinal electrostatic waves with a magnetic field $\mathbf{B}_0$. Neglecting the ion dynamics and considering a cold plasma, the continuity and momentum conservation equations become

$$\begin{aligned} \frac{\partial n_e}{\partial t} + \nabla \cdot (n_e \mathbf{u}_e) &= 0, \\ m_e\, n_e \left(\frac{\partial \mathbf{u}_e}{\partial t} + (\mathbf{u}_e \cdot \nabla)\, \mathbf{u}_e \right) &= -e\, n_e (-\nabla\phi + \mathbf{u}_e \times \mathbf{B}_0), \\ \nabla^2 \phi &= \frac{e}{\varepsilon_0}(n_e - n_i). \end{aligned}$$

Assuming that the perturbations have a harmonic dependence, the linearized system of equations is

$$\begin{aligned} -i\omega n_{e1} + i n_{e0} \mathbf{k} \cdot \mathbf{u}_{e1} &= 0, \\ -i\omega \mathbf{u}_{e1} &= i\, \frac{e}{m_e}\, \mathbf{k}\phi - \frac{e}{m_e} \mathbf{u}_{e1} \times \mathbf{B}_0, \\ -k^2 \phi &= \frac{e}{\varepsilon_0} n_{e1}. \end{aligned} \tag{2.92}$$

Solving the system in Eqs. (2.92), the following dispersion relation is obtained

$$\omega^2 = \omega_{pe}^2 + \omega_{ce}^2 \equiv \omega_{uh}^2. \tag{2.93}$$

These oscillations are known as upper hybrid waves. The electrons oscillate in a magnetic field with the plasma frequency modified by the addition of the electron cyclotron motion [43].

Consider now the effect of the magnetic field on the ion sound waves. The linearized ion continuity and momentum conservation equations become

$$\begin{aligned} -i\omega n_{i1} + i n_{0i} \mathbf{k} \cdot \mathbf{v}_{i1} &= 0, \\ -i\omega \mathbf{v}_{i1} &= -\frac{e}{m_i} \mathbf{k}\phi + \frac{e}{mi} \mathbf{v}_{i1} \times \mathbf{B}_0. \end{aligned} \tag{2.94}$$

As it was the case with the ion sound waves, the electron density follows the Boltzmann distribution, $n_{e1} = n_{e0} e\phi / T_e$. Using quasineutrality $n_e = n_i$, the dispersion relation is given by

$$\omega^2 = k^2 c_s^2 + \omega_{ci}^2. \tag{2.95}$$

Equation (2.95) is the dispersion relation for the ion cyclotron waves. These waves have the ion sound frequency shifted by the ion cyclotron frequency [43].

An intermediate scale between the ion and electron cyclotron motion exists. In this intermediate scale the electrons are not free to move along the magnetic field and can only move in the direction perpendicular to $\mathbf{B}_0$. The electron response is not given by the Boltzmann distribution and needs to be calculated using the electron conservation equation in the direction perpendicular to the magnetic field [43]. The linearized electron conservation and continuity equation are

$$\begin{aligned} -i\omega n_{e1} + i n_{0e}\mathbf{k}_\perp \cdot \mathbf{u}_{e1} &= 0, \\ -i\omega \mathbf{u}_{e1} &= i\frac{e}{m_e}\mathbf{k}_\perp \phi - \frac{e}{m_e}\mathbf{u}_{e1} \times \mathbf{B}_0, \end{aligned} \tag{2.96}$$

where $\mathbf{k}_\perp$ is the wavevector in the direction perpendicular to the magnetic field. Using quasineutrality $n_e = n_i$ and solving the system of equations given by Eqs. (2.94) and (2.96), the dispersion relation is [43]

$$\omega^2 = \omega_{ce}\omega_{ci}. \tag{2.97}$$

The dispersion relation correspond to oscillations with a frequency equal to the product of the electron and ion cyclotron frequencies, known as the lower hybrid frequency [12]

$$\omega_{lh} = \left(\omega_{ce}\omega_{ci}\right)^{1/2}. \tag{2.98}$$

The oscillations that have been consider so far are stable and their amplitudes do not decrease or grow with time. Under certain conditions a plasma can sustain modes whose amplitudes grow with time, these modes are unstable. In a plasma with equilibrium electric and magnetic fields, the $\mathbf{E}_0 \times \mathbf{B}_0$ drift is very important for the plasma dynamics since this drift is the energy source of certain instabilities [4, 11, 13, 34]. In the case of a Hall thruster these instabilities are especially important since they affect the thruster performance and operation.

2.5.4 Negative energy instabilities in plasmas with flows

Normally, perturbations from the full thermodynamic equilibrium have positive energy, i. e. the kinetic energy $E = \int mv^2/2 \; d\tau > 0$, where $d\tau$ is the respective volume element, and v is the

[12] More on the lower hybrid mode and how it can be rendered unstable is presented in Section 5.3.1

perturbed velocity. In systems with a finite flow in the equilibrium state, the perturbations which have a phase velocity lower than the equilibrium velocity, $v_{ph} < \mathbf{v}_0$, may have a total energy in the perturbed state lower than the equilibrium energy related to the stationary flow, $\mathbf{v}_0$: $E^{'} = \int mv^2 d\tau/2 < E_0 = \int mv_0^2 d\tau/2$; here $v = v_0 + v^{'}$ is the total velocity, which includes an equilibrium part v_0 and a perturbation $v^{'}$. These are the so called negative energy perturbations [49, 50]. The amplitude of such perturbations increases when the energy is removed from the system and thus dissipation may destabilize the negative energy mode. Alternatively, the coupling of two modes, one with negative and other with positive energy, may lead to a reactive instability where both modes would grow via energy transfer from the negative energy mode to the mode with positive energy. A simple illustration of the negative energy modes and how they can be rendered unstable is shown in Fig. 2.6.

The simplest example of the negative energy instability in Hall plasma is the ion sound waves in presence of the equilibrium $\mathbf{E}_0 \times \mathbf{B}_0$ electron drift and electron collisions. The equilibrium electron $\mathbf{E}_0 \times \mathbf{B}_0$ velocity was not considered when the dispersion relation for the ion sound modes was derived. The effect of the equilibrium electron flow $\mathbf{u}_{e0}$ is hidden in the response of the electron current in the direction parallel to the magnetic field. Using the equilibrium $\mathbf{E}_0 \times \mathbf{B}_0$ electron velocity in the electron continuity equation gives

$$\frac{\partial n_{e1}}{\partial t} + \mathbf{u}_{e0} \cdot \nabla n_{e1} + n_{e0} \frac{\partial u_{e||}}{\partial z} = 0, \tag{2.99}$$

from which the electron current parallel to the magnetic field is

$$J_{e||} = -e(\omega - \omega_0) n_{e1}/k_{||}, \tag{2.100}$$

where $\omega_0 = \mathbf{k} \cdot \mathbf{u}_{e0}$ is the electron $\mathbf{E}_0 \times \mathbf{B}_0$ drift frequency.

The parallel electron current is affected by the magnetic field and exhibits a Doppler shift with respect to the density perturbations. In an infinite plasma (along the magnetic field), the parallel electron current remains arbitrary but finite. A coupling between the parallel electron current and the density and potential perturbations would modify the wave dynamics. The simplest feedback mechanism is provided by electron collisions. Including the electron collision frequency ν_e, the

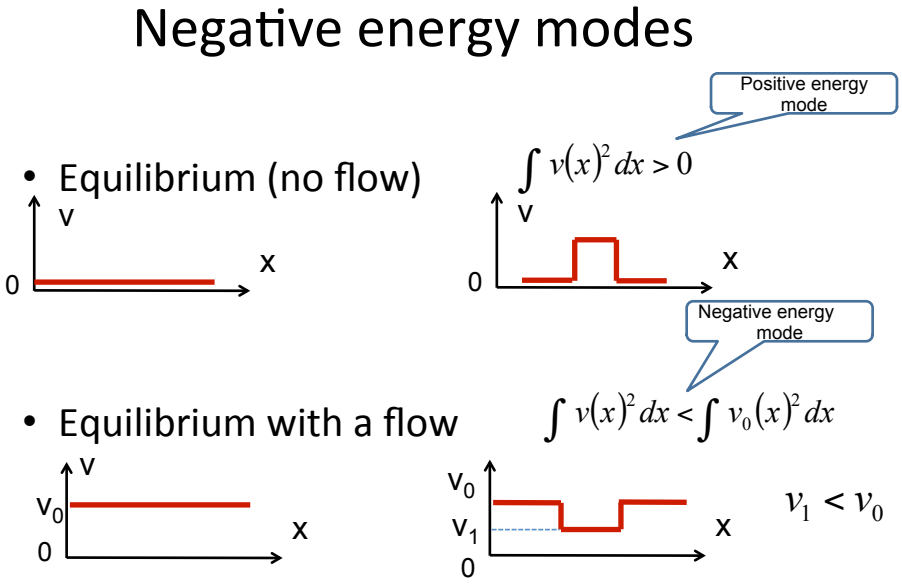

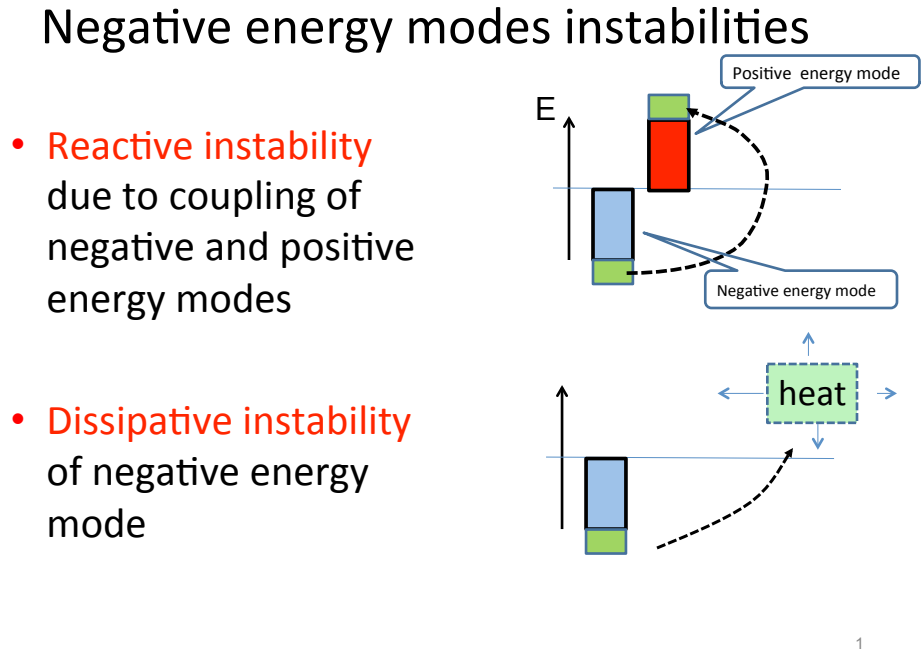

Figure 2.6: Negative energy modes. These modes arise when the velocity is less than some equilibrium flow velocity. Negative energy instabilities can be reactive where the amplitude of the instability grows due to energy transfer from the negative energy to the positive energy mode, or dissipative, the negative energy mode loses energy due to dissipation.

electron equation of motion can be written as

$$\begin{aligned} en_{e0}\nabla_{||}\phi - T_e\nabla_{||}n_{e1} - m_e n_{e0}\nu_e u_{e||} &= 0, \\ ik_{||}\left(\phi - \frac{T_e}{e}\frac{n_{e1}}{n_{e0}}\right) + \frac{m_e\nu_e}{e^2 n_{e0}}J_{e||} &= 0. \end{aligned} \tag{2.101}$$

The perturbed electron density can now be written from Eq. (2.101) as

$$\frac{n_{e1}}{n_{e0}} = \frac{e\phi}{T_e}\frac{1}{1 - i\nu_e(\omega - \omega_0)/k_{||}^2 v_{Te}^2/2}. \tag{2.102}$$

The ion response is due to the inertia and the effect of the magnetic field on the ions can be ignored, giving

$$\frac{n_{i1}}{n_{i0}} = \frac{k^2 c_s^2}{\omega^2}\frac{e\phi}{T_e}, \tag{2.103}$$

where $k^2 = k_\perp^2 + k_{||}^2$. Combining the ion and electron density perturbations from Eqs. (2.102) and (2.103), and using quasineutrality, produces the following dispersion relation

$$\omega = kc_s\left(1 - i\,\frac{\nu_e\,(\omega - \omega_0)}{2k_{||}^2 v_{Te}^2}\right). \tag{2.104}$$

The dispersion relation in Eq. (2.104) describes ion sound waves destabilized by electron collisions [33]. This mode is rendered unstable when $\omega < \omega_0$. In the ion sound instability, the dissipation is due to the electron collisions, which remove energy from the fluctuations. The coupling of the perturbed electron current, density and potential fluctuations creates the phase shift between current and potential which produces the instability via the positive feedback feeding the initial perturbations.

Additional examples of negative energy instabilities due to the equilibrium electron drift flow are the ones produced by gradients of plasma density, magnetic field and temperature. This type of instability is studied extensively in Chapter 3. Another type of negative energy instability is the one that arises due to effect of the sheath between the Hall thruster walls and the bulk plasma. This instability is studied in Chapter 4.

2.6 Anomalous transport

As seen in Section 2.4, the diffusion coefficient and the mobility across the magnetic field was predicted by the classical collisional based theory to change inversely proportional to B^2. In a

series of experiments beginning in the 1940's, performed by Bohm, working in isotope separation, it was observed that the diffusion coefficient did not follow the rule $D_\perp \sim B^{-2}$. Later, in the 1960's, in experiments in Hall thrusters, it was observed that the electron current to the anode was orders of magnitude higher than what was predicted by the purely collisional transport theory. Since the time of these first experiments, it is a well established fact that the observed electron current in Hall thruster cannot be explained by the purely classical collisional mechanism. This is one of the most long standing and important problems in Hall thruster research. The anomalous electron conductivity plays an important role in for the energy balance and thruster efficiency, that is why a clear picture of the main mechanisms responsible for the cross field transport in Hall thruster is necessary.

The anomalous electron transport is induced by correlated fluctuations of plasma potential and density. To see how exactly plasma oscillations can produce transport in plasma without the collisions, consider azimuthal oscillations (in the direction of $\mathbf{E}\times\mathbf{B}$) of plasma density and plasma potential. The momentum equation in the azimuthal direction is given by

$$m_e\,\tilde{n}\frac{du_y}{dt} = -e\tilde{n}\,\tilde{E}_y + J_{ax}B_z, \tag{2.105}$$

$$J_{ax} = -e\tilde{n}u_{ax}. \tag{2.106}$$

The time average of current density in the axial direction, given by

$$\langle J_{ax}\rangle = \frac{e}{B_z}\left\langle \tilde{n}\,\tilde{E}_y\right\rangle, \tag{2.107}$$

will be finite if the time average of the product of the plasma density and the perturbed electric field in the azimuthal direction is finite.

Oscillations of the plasma density and plasma potential in the azimuthal direction, $\hat{\mathbf{y}}$, are given by

$$\phi = \phi_0 + \tilde{\phi} = \phi_0 + \phi\,\cos\left(k_y y - \omega t\right), \tag{2.108}$$

$$n = n_0 + \tilde{n} = n_0 + n\,\cos\left(k_y y - \omega t + \eta\right), \tag{2.109}$$

where η is the phase difference between the plasma potential and density. The time averaged axial

current from Eq. (2.107) becomes

$$\langle J_{ax} \rangle = \frac{e}{B_r} \langle (n_0 + n \cos(k_y y - \omega t + \eta)) (-k_y \phi \sin(k_y y - \omega t)) \rangle , \tag{2.110}$$

$$= -k_y \frac{e\, n\, \phi}{B} \sin \eta. \tag{2.111}$$

This last equation says that for a finite phase difference between the plasma potential and density ($\eta \neq 0, n\pi$), there is a finite axial current. This can be seen in Fig. 2.7. In order to calculate the fluctuation induced current density, the first step is calculate the dispersion relation for the plasma in the Hall thruster. This is done to determine the growth rate of the instabilities that are responsible for the anomalous transport.

In fluctuation induced transport, the displacement is due to the perturbed $\mathbf{E} \times \mathbf{B}$ drift, that is

$$\delta = \langle \tilde{u}_{E\times B} \tau \rangle = \tau \frac{\nabla \phi}{B} \sim \tau \frac{1}{B} \frac{\tilde{\phi}}{\delta}, \quad \delta^2 = \frac{\tilde{\phi}}{B} \tau. \tag{2.112}$$

Bohm postulated that there is an equilibrium reached between the exponential growth of the amplitude of the perturbed potential due to the instabilities and the damping that occurs due to the diffusion process [51]. The equilibrium is reached at some saturation amplitude of the potential, ϕ_{sat}, that Bohm calculated empirically to satisfy $e\phi_{sat}/T_e = 1/16$ [51]. An estimate of the Bohm diffusion coefficient is then

$$D = \frac{\delta^2}{\tau} = \frac{\phi_{sat}}{B} = \frac{1}{16} \frac{T_e}{eB}. \tag{2.113}$$

Using Einstein's relation from Eq. (2.44), the Bohm mobility is given by

$$\mu_B = \frac{1}{16B}. \tag{2.114}$$

In numerical simulations of Hall thrusters, the anomalous transport is assumed a priori, and accounted for by the introduction by hand of a mobility given by the Bohm mobility, or some mobility of the type in Eq. (2.114).

The axial electron current can be characterized by introducing an effective collision frequency in the expression for the axial electron current

$$J_{ex} = -e\, n_e\, \mu_B E_x = -e\, n_e \frac{E_x}{B_z} \frac{\nu_{eff}}{\omega_{ce}} = -e\, n_e \frac{E_x}{B_z} \frac{1}{\omega_{ce} \tau_{eff}}. \tag{2.115}$$

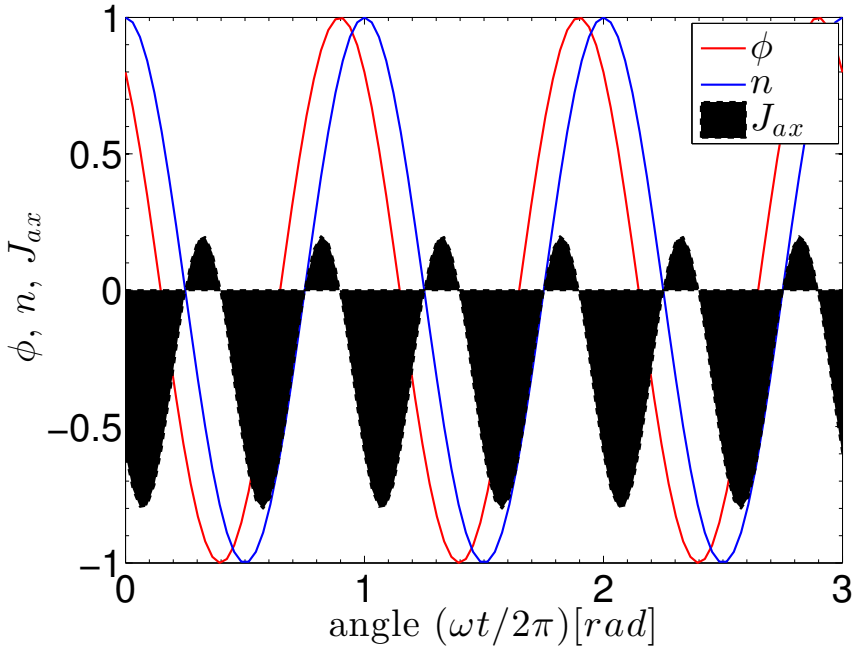

Figure 2.7: Density (blue), potential (red) and current density fluctuations (black filled). It is clear that when a phase difference exists between the plasma density and potential, the time averaged current density is finite.

From the experimentally measured electron current and plasma density, the effective collision frequency can be calculated as

$$\nu_{eff} = \frac{B_z}{E_x}\frac{J_{ex}}{e\,n_e}\omega_{ce}. \tag{2.116}$$

The electron current density on the right hand side of Eq. (2.116) is measured by subtracting the total discharge current density, that is defined as the discharge current divided by the Hall thruster channel exit area (the discharge current comes from the external power source) and the ion discharge current density [52]

$$J_{ex} = \frac{I_d}{A} - qn_iV_i. \tag{2.117}$$

The ion current density qn_iV_i can be measured directly from an ion flux probe or via measurements of the ion density using a Langmuir probe and ion velocity using laser induced fluorescence (LIF) [52, 53].

2.7 Summary

In the presence of a constant magnetic field a moving charged particle experiences a force such that its trajectory is circular. This circular motion is characterized by a radius known as Larmor radius and has an angular frequency known as gyro or cyclotron frequency. When an electric field is included, the center of the circular orbit, known as guiding center, moves in the direction perpendicular to the electric and magnetic field. This velocity is known as drift velocity and the drift motion as the $\mathbf{E} \times \mathbf{B}$ drift. This particular drift motion is charge independent with the ions and the electrons moving in the same direction. The $\mathbf{E} \times \mathbf{B}$ drift is an special case of the force generated drift. Other types of drift motion experienced by charged particles are the polarization, ∇B and curvature drifts.

It is impractical to describe the dynamics of the plasma as a function of the individual motion of the particles due to the large amount of particles present. For this reason a basic description of the plasma as a function of certain macroscopic parameters is needed. One such description is based on the fluid equations coupled with the Maxwell equations for the electric and magnetic fields. The fluid equations describe the time evolution of the plasma density and the conservation of momentum and energy of the different plasma species.

A key feature of plasma is that it exhibits a collective behavior product of the long range Coulomb interaction among charged particles. For distances longer than the Debye length, the electric field of any particular charged particle in the plasma is shielded by the action of the other charged particles and the plasma can be considered neutral. Changes in plasma parameters can excite different oscillations and waves in plasma. Examples of these waves are plasma oscillations, the ion sound, the electron and ion cyclotron waves and many other.

In plasmas with crossed electric and magnetic fields, perturbations can gain energy from the $\mathbf{E}_0 \times \mathbf{B}_0$ drift and become unstable. The negative energy long wavelength $\mathbf{E}_0 \times \mathbf{B}_0$ instability driven by the combination of magnetic field and density gradients is thought to be responsible for the appearance of certain structures observed in Hall thrusters known as spokes [30, 31]. This instability, that has also been experimentally and theoretically identified as a possible cause of anomalous transport in Hall plasma thrusters [27, 54], is studied in Chapter 3. Additional instabilities in Hall thrusters that have been theoretically and experimentally studied include the unstable

low-hybrid and Alfven waves due to collisions [13], instabilities caused by ionization [55, 56] and Rayleigh type shear flows [12] and high-frequency instabilities driven by the resonance between the electron cyclotron harmonics and the $\mathbf{E}_0 \times \mathbf{B}_0$ drift [28]. These modes play an important role in different physical processes in a Hall thruster, such as ionization, configuration of the electric potential and particle acceleration. In Chapter 4, the effect of the plasma wall interactions is reviewed. In that chapter, the effect that the closure current to the wall has on destabilizing the ion sound mode with equilibrium $\mathbf{E}_0 \times \mathbf{B}_0$ flow is studied. That effect is studied using an average of the plasma parameters in the direction parallel to the magnetic field as well as by considering the local structure of the fields in such direction. The effect of the dielectric and conducting walls is also studied. The complexity of the different processes that occur in a Hall thruster is such that certain phenomena need to be understood from computer simulations. One of such processes is the nonlinear dynamics of Hall thruster plasma that is thought to be responsible for the anomalous transport. The results of nonlinear simulations of Hall thruster plasma and anomalous electron transport are presented in Chapter 5.

CHAPTER 3

GRADIENT DRIFT INSTABILITIES

3.1 Introduction

In this chapter the problem of the long wavelength $\mathbf{E}_0 \times \mathbf{B}_0$ instability in plasmas with inhomogeneous magnetic field and gradients of plasma density gradients is reviewed. This problem was originally studied by Morozov [54] and more recently by Kapulkin [9]. It is expected that long wavelength modes will dominate the anomalous transport of electrons. These modes have been originally proposed [27, 54] as a possible cause of turbulent fluctuations and anomalous transport in Hall thruster. Recent experimental observations have confirmed the presence of high frequency long wavelength modes [57, 58], however it is not clear whether the standard criteria for gradient density magnetic field driven instability [9, 27, 54] are satisfied everywhere inside the thruster channel [59]. The problem of gradient instability is revisited and it is shown that quantitative corrections (to the previous theory) are required for an accurate determination of the conditions for the instability and its characteristics (real part of the frequency and the growth rate). Furthermore, it is shown that in an inhomogeneous magnetic field the studied modes have finite perturbations of the electron temperature. A three-field fluid model describing the fluctuations of the electric field, density, and electron temperature is developed and it is studied how finite temperature perturbations may affect the quantitative picture of the instabilities. General stability criteria and the picture of the instabilities for some realistic profiles of plasma parameters in Hall thrusters are investigated.

In this chapter, the concentration is on long wavelength modes existing in neglect of electron inertia and assuming $k_{\|} = 0$, when low hybrid and modified two-stream instabilities are not operative. These assumptions are similar to those in previous works [9, 54]. The instability of short wavelength modes in application to Hall thruster conditions (but without gradient effects) was

considered in kinetic theory and numerical simulations in Refs. [28, 36]. It was shown that short wavelength modes are excited with some features similar to those observed by collective light scattering [60,61]. The analysis in Refs. [28,36] also included in part the effects of $k_{\|} \neq 0$, which may be required in some Hall thruster experiments.

3.2 Long wavelength instability due to gradients of density and magnetic field

The gradients of plasma density and magnetic field were earlier identified as a source of robust instability in Hall thruster plasma with electron drift due to the equilibrium electric field. This instability is considered in this section and it shown that a more accurate analysis leads to a quantitatively different result as compared to previous works, though the physical mechanisms behind the instability remain similar.

Consider the simplified geometry of a coaxial Hall thruster with the equilibrium electric field $\mathbf{E}_0 = E_0\widehat{\mathbf{x}}$ in the axial direction $\mathbf{x}$ with $E_{0x} > 0$ and inhomogeneous density $n = n_0(x)$. Locally, Cartesian coordinates (x, y, z) are introduced with the z coordinate in the radial direction and y in the symmetrical azimuthal direction. The magnetic field is assumed to be predominantly in the radial direction, $\mathbf{B} = B_x(z)\widehat{\mathbf{x}} + B_0(x)\,\widehat{\mathbf{z}}$, with $B_0 \gg B_x$.

The ions are assumed unmagnetized so that the magnetic field is omitted in the ion momentum equation

$$m_i n_i \frac{d\mathbf{v}_i}{dt} = e n_i \mathbf{E} - \nabla p_i. \tag{3.1}$$

The ion density is found from the continuity equation

$$\frac{\partial n_i}{\partial t} + \nabla \cdot (n_i \mathbf{v}_i) = 0. \tag{3.2}$$

Assuming $n_i = n_0 + \widetilde{n}_i$ and $\mathbf{v}_i = \mathbf{v}_0 + \widetilde{\mathbf{v}}_i$, with the zeroth order ion velocity defined as $v_0\hat{\mathbf{x}}$, Eqs. (3.1)–(3.2) can be linearized as

$$\frac{\partial \widetilde{\mathbf{v}}_i}{\partial t} + v_0 \frac{\partial \widetilde{\mathbf{v}}_i}{\partial x} = e\mathbf{E} - \frac{\nabla p_i}{m_i n_0}, \tag{3.3}$$

$$\frac{\partial \widetilde{n}_i}{\partial t} + \mathbf{v}_0 \frac{\partial \widetilde{n}_i}{\partial x} + n_0 \nabla \cdot \widetilde{\mathbf{v}}_{\mathbf{i}} = 0. \tag{3.4}$$

Solution in Fourier form, $\sim\ e^{i(\mathbf{k}\cdot\mathbf{r}-\omega t)}$, are looked for, which requires the Boussinesque quasi-classical approximation $k_x L_x \gg 1$, where $\mathbf{k} = (k_x, k_y, 0\ )$ is the wavevector of the perturbations. Considering only electrostatic perturbations and isothermal ions, Eqs. (3.3)–(3.4) give

$$\frac{\widetilde{n}_i}{n_0} = \frac{e}{m_i}\frac{k_\perp^2\,\phi}{(\omega - k_x v_0)^2 - k_\perp^2 v_{Ti}^2/2}, \tag{3.5}$$

where $v_{Ti}^2 = 2T_i/m_i$, and $k_\perp^2 = k_x^2 + k_y^2$.

The second term in the denominator of Eq. (3.5) is responsible for ion thermal effect and Landau wave resonance. Note that perturbations aligned along the equilibrium magnetic field are not considered, so the conditions $\omega \gg (k_z v_{Te}, k_z v_{Ti})$ are satisfied both for ions and electrons.

In a Hall thruster, the ions can be considered cold ($T_i \approx 0$) and therefore the term $k_\perp^2 v_{Ti}^2$ is ignored, so that Eq. (3.5) can be approximated as [1]

$$\frac{\widetilde{n}_i}{n_0} = \frac{e}{m_i}\frac{k_\perp^2\,\phi}{(\omega - k_x v_0)^2}. \tag{3.6}$$

The general electron momentum equation is

$$m_e n_e \frac{d\mathbf{v}_e}{dt} = -e n_e\,(\mathbf{E} + \mathbf{v}_e \times \mathbf{B}) - \nabla p_e. \tag{3.7}$$

The electrons are magnetized and the conditions

$$\omega \ll \omega_{ce},\ \rho_e \ll L \tag{3.8}$$

are satisfied. The electron inertia term on the left hand side can be neglected for relatively low frequency long wavelength modes. This assumption eliminates low hybrid and modified two-stream instabilities. Under these conditions, the electron velocity can be found in the form

$$\mathbf{v}_e = \mathbf{v}_E + \mathbf{v}_{pe}, \tag{3.9}$$

where $\mathbf{v}_E$ is the is the $\mathbf{E}\times\mathbf{B}$ drift and $\mathbf{v}_{pe}$ is the is the diamagnetic drift, given by

$$\mathbf{v}_E = \frac{\mathbf{b}}{B_0}\times\nabla\phi, \tag{3.10}$$

$$\mathbf{v}_{pe} = -\frac{\mathbf{b}}{enB_0}\times\nabla p_e. \tag{3.11}$$

[1] As stated before, the term $k_\perp^2 v_{Ti}^2$ is responsible for ion thermal and Landau damping effects. These effects are better studied using a kinetic approach [44]. Since the ions are cold, it is safe to neglect these effects.

The fluid velocity from Eq. (3.9) is used in the continuity equation

$$\frac{\partial n_e}{\partial t} + \nabla \cdot (n_e \mathbf{v}_e) = 0, \tag{3.12}$$

giving the following equation for perturbed electron density

$$\frac{\partial}{\partial t} n + \mathbf{v}_E \cdot \nabla n - 2n\mathbf{v}_E \cdot \nabla \ln B - 2n\mathbf{v}_{pe} \cdot \nabla \ln B = 0. \tag{3.13}$$

Here, the terms with gradients of magnetic field appear as a result of compressibility of the $\mathbf{E} \times \mathbf{B}$ and diamagnetic velocity. The compressibility is calculated assuming a low pressure plasmas so that terms due to the equilibrium plasma current are neglected, $\nabla \times \mathbf{B} = 0$, that is, the equilibrium magnetic field is assumed to be the vacuum field. This results in

$$\nabla \cdot \mathbf{V}_E \simeq -2\mathbf{V}_E \cdot \nabla \ln B, \tag{3.14}$$

$$\nabla \cdot (n\mathbf{V}_{pe}) \simeq -2n\mathbf{V}_{pe} \cdot \nabla \ln B. \tag{3.15}$$

It is worth noticing that in a number of previous papers, such as Refs. [9, 54], the compressibility is calculated by assuming a strictly one- dimensional magnetic field in the form $\mathbf{B} = B_0(x)\,\widehat{\mathbf{z}}$ and the compressibility of electron flow was taken to be in the form $\nabla \cdot \mathbf{V}_E \simeq -\mathbf{V}_E \cdot \nabla \ln B$. A one-dimensional magnetic field $\mathbf{B} = B_0(x)\,\widehat{\mathbf{z}}$ has to be supported by a finite plasma current, which is not typical for Hall thruster conditions where the magnetic field with high accuracy is very close to the vacuum field.

Neglecting electron temperature fluctuations, the electron continuity equations results in the following form of the perturbed electron density

$$\frac{n_e}{n_0} = \frac{\omega_n - \omega_D}{\omega - \omega_0 - \omega_D} \frac{e\phi}{T_e}. \tag{3.16}$$

Here, $\omega_D = k_y v_D$, $\omega_0 = k_y u_0$ and $\omega_n = k_y v_n$; v_D is the magnetic drift velocity, v_n is the electron diamagnetic drift velocity and u_0 is the electric drift velocity in the equilibrium electric field,

$$v_D = -2\frac{T_e}{eB_0 L_B},\ v_n = -\frac{T_e}{eB_0 L_N},\ \mathbf{u}_0 = -\hat{\mathbf{y}}\frac{E_{0x}}{B_0}, \tag{3.17}$$

where

$$\frac{1}{L_B} = \frac{\partial}{\partial x} \ln B(x),\ \frac{1}{L_n} = \frac{\partial}{\partial x} \ln n_0(x).$$

Invoking quasineutrality and using Eqs. (3.6) and (3.16), the following dispersion relation is obtained [62]

$$\frac{\omega_n - \omega_D}{\omega - \omega_0 - \omega_D} = \frac{k_\perp^2 c_s^2}{(\omega - k_x v_{0i})^2}, \tag{3.18}$$

whose solutions are given by

$$\omega - k_x v_0 = \frac{1}{2}\frac{k_\perp^2 c_s^2}{\omega_n - \omega_D} \pm \frac{1}{2}\frac{k_\perp^2 c_s^2}{\omega_n - \omega_D}\sqrt{1 + 4\frac{k_x v_0}{k_\perp^2 c_s^2}(\omega_n - \omega_D) - 4\frac{k_y^2}{k_\perp^2}\rho_s^2\Delta}, \tag{3.19}$$

where

$$\Delta = \frac{\partial}{\partial x}\ln\left(\frac{n_0}{B_0^2}\right)\left[\frac{eE_0}{T_e} + \frac{\partial}{\partial x}\ln\left(B_0^2\right)\right].$$

The instability will occur (neglecting the ion flow term v_0) when

$$\frac{k_y^2}{k_\perp^2}\rho_s^2\frac{\partial}{\partial x}\ln\left(\frac{n_0}{B_0^2}\right)\left[\frac{eE_0}{T_e} + \frac{\partial}{\partial x}\ln\left(B_0^2\right)\right] > \frac{1}{4}, \tag{3.20}$$

where $\rho_s^2 = T_e m_i c^2/e^2 B_0^2$ is the so called ion-sound Larmor radius.

The frequency in Eq. (3.19) is similar to the electrostatic limit in Refs. [27,54]. However those authors did not include the compressibility of the electron diamagnetic drift due to a finite electron temperature so the ω_D term in the denominator of the right hand side of Eq. (3.19) was absent. The electron diamagnetic drift was included in Ref. [9], however part of the electron compressibility was omitted as described above. As a result, our dispersion equation (3.19) is similar in structure to the equation (18) in Ref. [9], but numerical factors are different. The difference occurs precisely because of the incomplete account of electron flow compressibility in Refs. [9, 54].

Typically the electric field in the acceleration zone is large so that

$$\frac{eE_{0x}}{T_e} > \frac{\partial}{\partial x}\ln\left(B_0^2\right). \tag{3.21}$$

The condition for the instability then becomes

$$\frac{\partial}{\partial x}\ln\left(\frac{n_0}{B_0^2}\right) > l_c^{-1}, \tag{3.22}$$

where the parameter l_c is defined as

$$l_c \equiv \frac{k_y^2}{k_\perp^2}\rho_s^2\left(\frac{eE_{0x}}{T_e} + \frac{\partial}{\partial x}\ln\left(B_0^2\right)\right), \tag{3.23}$$

and it is assumed that $E_{0x} > 0$.

For a weak electric field

$$\frac{eE_{0x}}{T_e} < \frac{\partial}{\partial x} \ln\left(B_0^2\right), \tag{3.24}$$

the weaker instability may set in for

$$4\frac{k_y^2}{k_\perp^2}\rho_s^2 \frac{\partial}{\partial x} \ln\left(\frac{n_0}{B_0^2}\right) \frac{\partial}{\partial x} \ln\left(B_0^2\right) > 1. \tag{3.25}$$

Equations (3.22) and (3.25) define the instability boundary in the (L_N, L_B) space. For purely azimuthal propagation (k_x =0), and L_N and L_B of the same sign, the instability occurs when $L_B > 2\,L_N$. When L_N and L_B are of opposite signs, the instability occurs for negative L_B. There is no instability when L_B is positive but L_N is negative. Figure 3.1 shows the contour plot of the growth rate as a function of L_N and L_B for typical Hall thruster parameters ($B_0 = 150$ G, $n_0 = 10$ ^{12} cm $^{-3}$, u_0 = -4.75 $\times$ 10 ^{7} cm/s, $T_e = 10$ eV, channel length=2.5 cm) and typical characteristic lengths of the order of the channel length. The instability growth rate is in the megahertz range, increasing towards the marginal instability boundary $L_B = 2\,L_N$, close to which, the maximum growth rate is of the order of 50 MHz. The growth rates are smaller in the region where L_B is negative and L_N is positive. The growth rate for fixed values of L_B, as a function of L_N is shown in Fig. 3.2 and in Fig. 3.3 as a function of L_B. The growth rate sharply peaks as plasma parameters approach the instability boundary. Away from this boundary the growth rate decreases to values of the order of 0.5-1 MHz.

A characteristic feature of the dispersion relation (3.19) is a weak dependence of the real part of the frequency on the value of the equilibrium electric field, which enters only via the $k_x v_0$ term. For the generic case $L_N \simeq L_B \simeq L_T \simeq L_\phi$, the real and imaginary parts of the frequency scale as

$$\omega_r \simeq \omega_{ci} k_y L, \tag{3.26}$$

and

$$\gamma \simeq k_\perp c_s \sqrt{\frac{eE_{x0}}{\left(L_B^{-1} - L_N^{-1}\right)}} \simeq k_\perp c_s \sqrt{\frac{e\phi_0}{T_e}}. \tag{3.27}$$

A notable feature of this instability is that the growth rates are maximal near the marginal stability boundary. The real part of the frequency also increases near the stability boundary and does not scale with the equilibrium $\mathbf{E} \times \mathbf{B}$ electron drift velocity. It is important to note that the density gradient parameter L_N is intrinsically related to the electric field and, effectively, the electric field enters the dispersion relation (3.18) also via L_N.

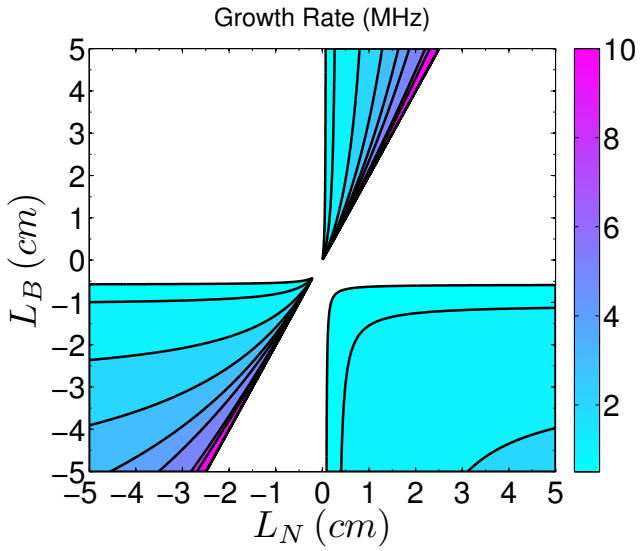

Figure 3.1: Contour plot of the growth rate as a function of L_N and L_B.

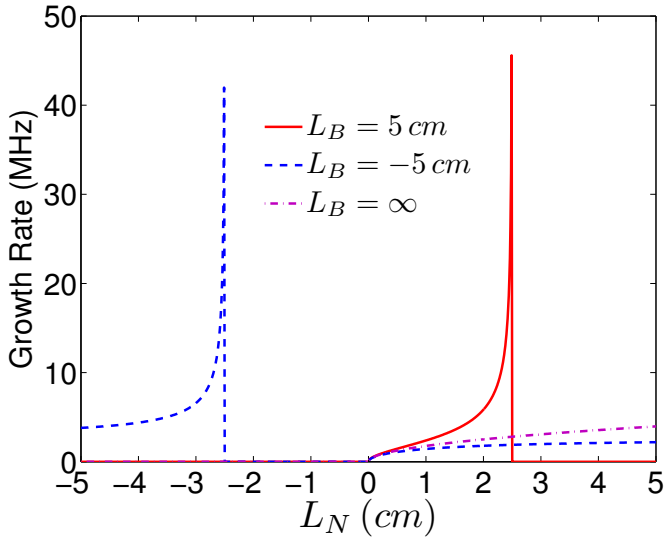

Figure 3.2: Growth rate as a function of L_N for different values of L_B.

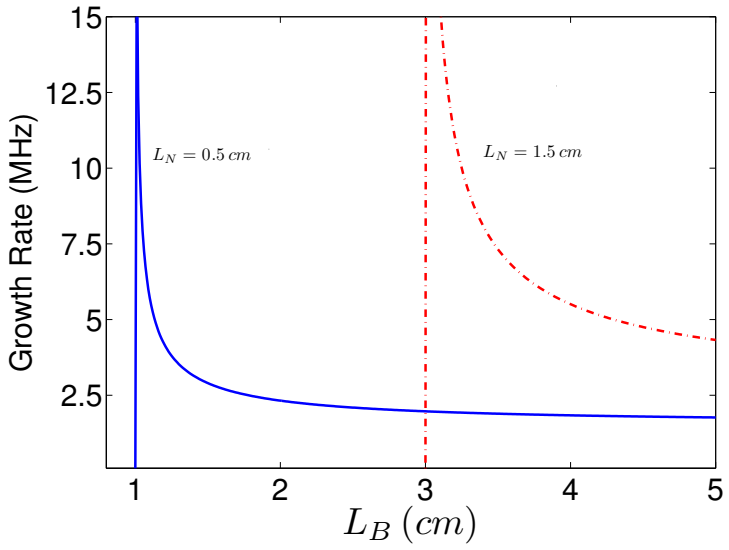

Figure 3.3: Growth rate as a function of L_B for different values of L_N as given by the two-fluid model. The vertical lines correspond to the instability boundary. As can be seen from the plots, the growth rate tends asymptotically to the values 1.56 MHz and 2.66 MHz, which correspond to the straight horizontal lines in Fig. 3.7.

The gradient-drift instability described by Eq. (3.18) persists also in the case when there is no gradient of the magnetic field. In this case, and assuming $k_x = 0$, the dispersion relation reduces to

$$\frac{\omega_n}{\omega - \omega_0} = \frac{k_\perp^2 c_s^2}{\omega^2}. \tag{3.28}$$

The solution of the dispersion relation (3.28) is

$$\omega = \frac{k_\perp^2 c_s^2}{2\omega_n}\left(1 \pm \sqrt{1 - \frac{4\omega_n\omega_0}{k_\perp^2 c_s^2}}\right). \tag{3.29}$$

From Eq. (3.29), the conditions for instability can be obtained as $(\partial/\partial x)\ln(n_0)\,E_0 > 0$ and

$$\frac{4|u_0|}{\omega_{ci}}\frac{1}{L_N} > 1. \tag{3.30}$$

Instabilities driven by plasma density gradient and $\mathbf{E}_0 \times \mathbf{B}_0$ drifts were studied in ionospheric physics [63–65], though under different conditions, either with magnetized ions [64] or unmagnetized but strongly collisional ions [65].

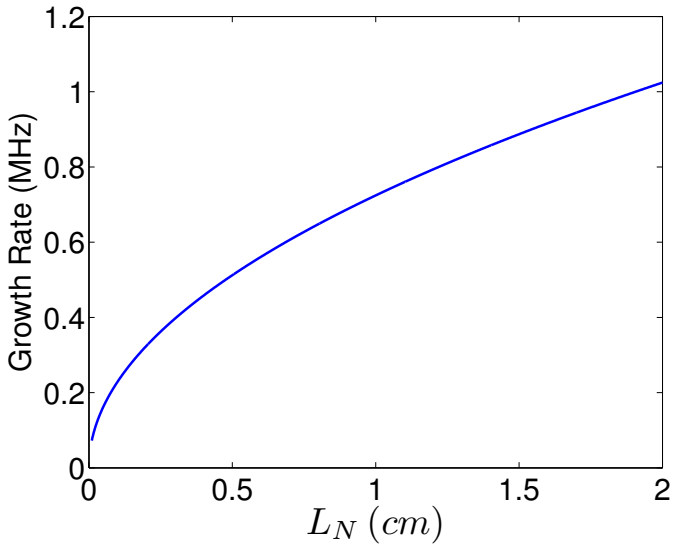

Figure 3.4: Growth rate as a function of L_N for the case with no gradients of the magnetic field.

3.3 Electron temperature fluctuations effects

The instability described in Refs. [9,54] and revisited here is caused by an unfavorable combination of plasma density and magnetic field gradients. It is well known however that such instabilities can be affected by temperature gradients which were neglected by the authors of Refs. [9, 54]. Temperature gradient instabilities [66] are the main source of anomalous plasma transport in fusion plasmas [67] and may occur both in configurations with inhomogeneous magnetic field as well as in configurations with a uniform field. [68,69] In this section it is considered how the gradient drift instability in inhomogeneous magnetic field may be affected by temperature gradients, which are known to be significant for typical Hall thruster parameters [70].

When fluctuations of the electron temperature are included, the electron continuity and momentum equations are complemented by the electron energy balance equation in the form

$$\frac{3}{2}\frac{dp}{dt} + \frac{5}{2}p\nabla\cdot\mathbf{v} + \nabla\cdot\mathbf{q} = 0, \tag{3.31}$$

which includes the electron diamagnetic heat flux

$$\mathbf{q} = -\frac{5}{2}\frac{p}{eB_0}\mathbf{b}\times\nabla T. \tag{3.32}$$

The electron energy equation together with the electron continuity equation, quasineutrality and the equations for the ion component constitutes a three-field (n, T, ϕ) fluid model for the gradient-drift instability, while in the two-field model, only the electron density and electrostatic potential were included, (n, ϕ) . Taking into account finite electron temperature fluctuations, the electron density equation (3.13) results in

$$-\left(\omega-\omega_0-\omega_D\right)\frac{\widetilde{n}_e}{n_0}+\omega_D\frac{\widetilde{T}_e}{T_0}=-\left(\omega_n-\omega_D\right)\frac{e\phi}{T_e}. \tag{3.33}$$

The temperature evolution can be found from the energy balance equation (3.31) or equivalently from the temperature equation

$$\frac{3}{2}n\frac{dT}{dt}+p\nabla\cdot\mathbf{v}+\nabla\cdot\mathbf{q}=0. \tag{3.34}$$

Using Eqs. (3.9) and (3.32), Eq. (3.34) is reduced to the form

$$\frac{3}{2}n\left(\frac{\partial T}{\partial t}+\mathbf{v}_E\cdot\nabla T\right)-2p\mathbf{v}_E\cdot\nabla\ln B+\frac{2T}{eB_0}\nabla\ln B\cdot\mathbf{b}\times\nabla p+\frac{5p}{eB_0}\nabla\ln B\cdot\mathbf{b}\times\nabla T=0. \tag{3.35}$$

After linearization, the following equation is obtained

$$\omega_D\frac{\widetilde{n}_e}{n_0}+\left(\frac{7}{2}\omega_D-\frac{3}{2}\left(\omega-\omega_0\right)\right)\frac{\widetilde{T}_e}{T_e}=\left(\omega_D-\frac{3}{2}\omega_{*T}\right)\frac{e\phi}{T_e}, \tag{3.36}$$

where

$$\omega_{*T}=-\frac{k_y T_{e0}}{eB_0L_T},\quad \frac{1}{L_T}=\frac{\partial\ln T_{e0}}{\partial x}. \tag{3.37}$$

The coupled equations (3.33) and (3.36) for density and temperature can be solved giving the following equations for the electron temperature and density

$$\frac{\tilde{T}_e}{T_e}=\frac{\left(\omega-\omega_0-\omega_D\right)\omega_{*T}-\frac{2}{3}\left(\omega-\omega_0-\omega_n\right)\omega_D}{(\omega-\omega_0)^2-\frac{10}{3}\omega_D(\omega-\omega_0)+\frac{5}{3}\omega_D^2}\frac{e\phi}{T_e}, \tag{3.38}$$

$$\frac{n_e}{n_0}=\frac{-\left(\omega-\omega_0\right)\left(\omega_D-\omega_n\right)+\omega_D\left(\omega_{*T}-\frac{7}{3}\omega_n\right)+\frac{5}{3}\omega_D^2}{(\omega-\omega_0)^2-\frac{10}{3}\omega_D(\omega-\omega_0)+\frac{5}{3}\omega_D^2}\frac{e\phi}{T_e}. \tag{3.39}$$

It should be noted that the models for the electron density and electron temperature used here completely neglect the parallel electron dynamics in the direction of the equilibrium magnetic field. Using Eqs. (3.39) and (3.6), along with the quasineutrality condition, the following cubic dispersion relation is obtained

$$\frac{-\left(\omega-\omega_0\right)\left(\omega_D-\omega_n\right)+\omega_D\left(\omega_{*T}-\frac{7}{3}\omega_n\right)+\frac{5}{3}\omega_D^2}{(\omega-\omega_0)^2-\frac{10}{3}\omega_D(\omega-\omega_0)+\frac{5}{3}\omega_D^2}=\frac{k_\perp^2c_s^2}{(\omega-k_xv_{0i})^2}. \tag{3.40}$$

The dispersion relation in Eq. (3.40), can be written as

$$a\omega^3 + b\omega^2 + c\omega + d = 0, \tag{3.41}$$

where the coefficients a, b, c and d are given by

$$\begin{aligned}
a &= \omega_n - \omega_D, \\
b &= -k_y^2 c_s^2 - \omega_n\omega_0 - \frac{7}{3}\omega_n\omega_D + \omega_0\omega_D + \frac{5}{3}\omega_D^2 + \omega_{*T}\omega_D, \\
c &= 2k_y^2 c_s^2\omega_0 + \frac{10}{3}k_y^2 c_s^2\omega_D, \\
d &= -k_y^2 c_s^2\omega_0^2 - \frac{10}{3}k_y^2 c_s^2\omega_0\omega_D - \frac{5}{3}k_y^2 c_s^2\omega_D^2.
\end{aligned}$$

It is well known that Eq. (3.41) has complex roots (one real and two complex conjugate) if the following condition is met:

$$\Delta = 18abcd - 4b^3 d + b^2 c^2 - 4ac^3 - 27a^2 d^2 < 0. \tag{3.42}$$

As can be seen from Eq. (3.42), the three-field model instability condition cannot be easily expressed in a succinct way, similar to Eq. (3.20).

It is important to note that temperature fluctuations remain finite even in plasmas without temperature gradients. Finite temperature fluctuations occur as a result of plasma compression in an inhomogeneous magnetic field. Note that the plasma dynamics is not adiabatic due to the finite compressibility of the heat flux, $\nabla \cdot \mathbf{q} \neq 0$. In magnetized plasmas with nonuniform magnetic field the flow of plasma density and energy are different. As a result, even in the limit of $L_T = \infty$, the three-field model predicts a different stability picture compared to the two-field model. In a homogeneous magnetic field, when $\omega_D = 0$, the dispersion relation given by Eq. (3.40) reduces to Eq. (3.28) and temperature gradient effects are not important.

Equation (3.40) is solved numerically to study the effect of the gradients of the electron temperature in the three-field model. The qualitative landscape of the instability in the (L_N, L_B) plane is similar to the results obtained from the two-field model, shown in Fig. 3.1, though quantitatively, the growth rate values and the behavior change.

The growth rate profile as a function of L_B and L_T is shown on the contour plot in Fig. 3.6 for $L_N = 0.5$ cm and $L_N = 1.5$ cm. For this characteristic density gradient lengths, the maximum growth rates for positive values of L_T is of the order of 15 MHz and 22 MHz, attained close to the

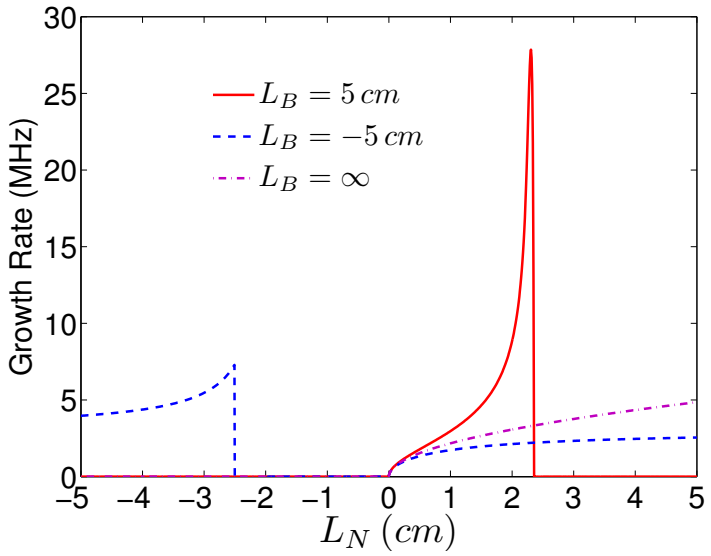

Figure 3.5: Growth rate as a function of L_N for different values of L_B when L_T is 1 cm.

instability boundary. It is also clear that the stability window widens for increasing positive values of L_N. For the (positive) values of L_N used, the instability is also possible for negative gradients of temperature. The value of the growth rate in this case is smaller than for positive values of L_B.

Figure 3.7 shows the effects of temperature in the three-field model. For lower values of L_B (strong magnetic field gradient) the instability occurs only for a narrow window of L_T values. When the characteristic length L_B increases, the instability regions becomes wider and the growth rate decreases from a maximum value of around 10 MHz to a value of 1.56 MHz when L_N =0.5 cm, and from around 20 MHz to 2.66 MHz when L_N =1.5 cm. These latter values correspond to the limit of no magnetic field gradient ($L_B \rightarrow \infty$). The same limit is recovered from the two-field model as shown in Fig. 3.3. One of the important results obtained from the three-field model is the stabilization of the instability for larger temperature gradients. On the other hand, in unstable regions, the three-field model predicts higher growth rates than the ones obtained from the two-field model. A comparison between the two-field and three-field models can be seen in Fig. 3.7, which shows the growth rate as a function of the temperature gradient L_T for different values of L_B and L_N. This behaviour is to be compared with the results of the two-field model, shown in Fig. 3.3, where the growth rate is shown as a function of L_B, for two values of L_N , namely L_N = 0.5 cm and L_N = 1.5 cm. Another important difference between the two-field and

the three-field models is in the growth rates predicted for small values of the electric field, such as the values of the electric field near the anode in a Hall thruster. The dependence of the growth rate on the electric field is drawn in Fig. 3.8. In both cases, the growth rate increases with increasing electric field and decreases with increasing value of L_B. This corresponds to regions away from the instability boundary. In regions where the value of the electric field is close to zero, the two-field model predicts a non-zero growth rate. The three-field model predicts a small stable region close to E_0=0. This stable region becomes narrower as the value of L_B increases. The growth rate increases sharply close to this stability boundary. It reaches a peak and then falls and continues to grow with the electric field. When the parameter L_T increases, while L_B and L_N remain fixed, the growth rate decreases, but the stable region becomes wider. This shows that the effect of the temperature gradients is to reduce the instability when L_T grows, but at the same time, regions of stability are created in regions where L_T is small, as can be seen in Fig. 3.9. This situation can be clearly appreciated in Fig. 3.10, where the growth rate as a function of the electric field is plotted for the parameters L_N =1.5 cm and L_B =2.9 cm. For these parameters, the two-field model predicts stability, while the three-field model predicts instability for certain values of the electric field.

The long wavelength instabilities described by Eqs. (3.18) and (3.40) have the equilibrium electron flow as the main driving source of the instability, which is triggered by the presence of the gradients of plasma density, temperature and magnetic field. The Hall plasma with equilibrium electron current can be destabilized by the density gradient alone. The corresponding instability became known as the Simon-Hoh instability [63, 71, 72]. In the purely collisionless case, it was called the anti-drift instability [73], because of the inverse dependence of the real part of the frequency on the drift frequency. The dispersion relation for the anti-drift mode follows from Eq. (3.18), assuming no magnetic field gradients,

$$\frac{\omega_n}{\omega - \omega_0} = \frac{k_\perp^2 c_s^2}{(\omega - k_x v_{0i})^2}. \tag{3.43}$$

The condition $\mathbf{E}_0 \cdot \nabla n_0 > 0$ was noted as required for the Simon-Hoh instability [10]. A more accurate condition follows from (3.18), $(eE_0/T_e)\,(\partial/\partial x)\ln(n_0) > 1/(4\rho_s^2)$.

Sakawa *et al.* [10] have considered the so called modified Simon-Hoh instability by including the finite equilibrium ion velocity (in azimuthal direction) that may occur due to the partial mag-

netization of the ion motion. The amplitude of this ion drift velocity with large Larmor radius was estimated for Maxwellian plasma by averaging the $\mathbf{E} \times \mathbf{B}$ drift over the ion gyroradius [10],

$$v_{\theta i} = \frac{E_0}{B_0} e^{-b} I_0(b), \tag{3.44}$$

where $b = k_\perp^2 \rho_i^2 >> 1$ is the parameter characterizing the large (ion) Larmor radius parameter, $k_\perp \sim L^{-1}$, L is the characteristic length scale of the electric field inhomogeneity. The resulting dispersion relation [10] then is

$$\frac{\omega_n}{\omega - \omega_0} = \frac{k_\perp^2 c_s^2}{(\omega - k_x v_{0i} - k_y v_{\theta i})^2}. \tag{3.45}$$

Essentially this is the anti-drift mode equation (3.43) with an additional azimuthal ion velocity. The addition of the finite $v_{\theta i}$ to the ion response changes the real part of the frequency by an additional factor of $k_y v_{\theta i}$, but does not affect the growth rate of the long wavelength modes in a significant way as long as $v_{\theta i} < u_0$. The $v_{\theta i}$ velocity from Eq. (3.44) has a value of around 0.1% - 5% of u_0 for the plasma parameters used here and will be neglected for the most part.

The authors of Refs. [27, 54] considered the related mode in plasma with inhomogeneous magnetic field. They also included the electromagnetic effects and electron inertia which are not important for typical plasma parameters in Hall thrusters. Esipchuk and Tilinin [54] have also included the electron drift effects related to plasma density gradient. However, they have made an additional assumption that plasma density gradient can be related to the gradient of the electric potential via the density conservation equation and assuming the ballistic acceleration of ions. Thus, they have used the relations

$$n_0(x) v_{0i}(x) = const, \tag{3.46}$$

$$v_{0i} \frac{dv_{0i}}{dx} = -\frac{e}{m_i} E_0(x), \tag{3.47}$$

to find the density gradient in terms of the electron equilibrium drift velocity u_0

$$\frac{\partial \ln n_0}{\partial x} = u_0 \frac{\omega_{ci}}{v_{0i}^2}. \tag{3.48}$$

They also defined the magnetic drift velocity u_B via the relation

$$u_B = \frac{v_{0i}^2}{\omega_{ci}} \frac{\partial \ln B_0}{\partial x}. \tag{3.49}$$

With these definitions, the dispersion relation derived by Esipchuk and Tilinin [54] has the form

$$\frac{\omega_{pi}^2}{(\omega - k_x v_{0i})^2} = \frac{\omega_{pi}^2 (k_y u_0 - k_y u_B)}{k^2 v_{0i}^2 (\omega - k_y u_0)}. \tag{3.50}$$

The electron inertia, electromagnetic and non-quasineutrality effects have been omitted here for ease of comparison. As it was noted above, the latter effects are small for the typical parameters here considered. The dispersion equation (3.50) does not contain the drift due to density gradient explicitly since it has been replaced via the relation (3.48).

Equation (3.50) can be rewritten explicitly retaining the drift frequency so it takes the form

$$\frac{\omega_n - \omega_D^{'}}{\omega - \omega_0} = \frac{k_\perp^2 c_s^2}{(\omega - k_x v_{0i})^2}. \tag{3.51}$$

Here the magnetic drift frequency is defined as $\omega_D^{'} = -k_y T_e / (eB_0 L_B)$, compare this equation with the two-fluid model equation (3.18). The difference between $\omega_D^{'}$ in Eq. (3.51) and ω_D in our two-fluid model, Eq. (3.18), is due to an incomplete account of the electron flow incompressibility in Ref. [27]. Morozov has also neglected the compressibility of the electron diamagnetic flow [27]. As a result, an additional ω_D is missing in the denominator of Eq. (3.51), compared with Eq. (3.18).

3.4 General stability analysis

In order to study the instabilities predicted by the two- and three-field models realistic profiles of the magnetic field, electric field, plasma density and electron temperature are used. In this section the dispersion relation for each model is solved using the plasma parameters obtained in three different experiments [5, 6, 8] and simulations [7].

The main goal of this section is to apply the analytical results obtained earlier in this chapter to realistic configurations of Hall thrusters [11]. It is also discussed here how the previous models [10, 63, 71, 73] for gradient drift type modes are related to the advanced model put forward in Ref. [11]. It is investigated how plasma parameters, such as the equilibrium $\mathbf{E} \times \mathbf{B}$ drift, gradients of plasma density, temperature and magnetic field affect the characteristics, excitation conditions and localization of the linear instabilities and it is discussed how these may be related to some experimentally observed features, such as spoke generation. Experimental data for a 2 kW Hall thruster from the Hall Thruster experiment (HTX) at Princeton Plasma Physics Laboratory (PPPL)

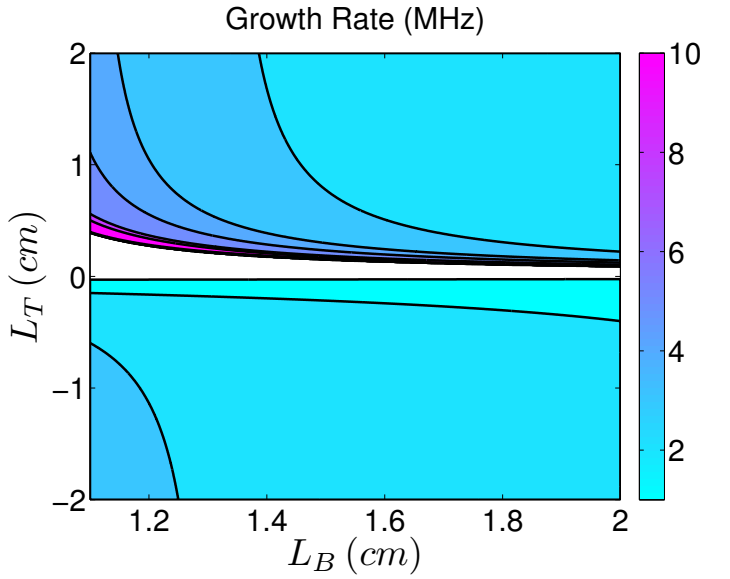

(a)

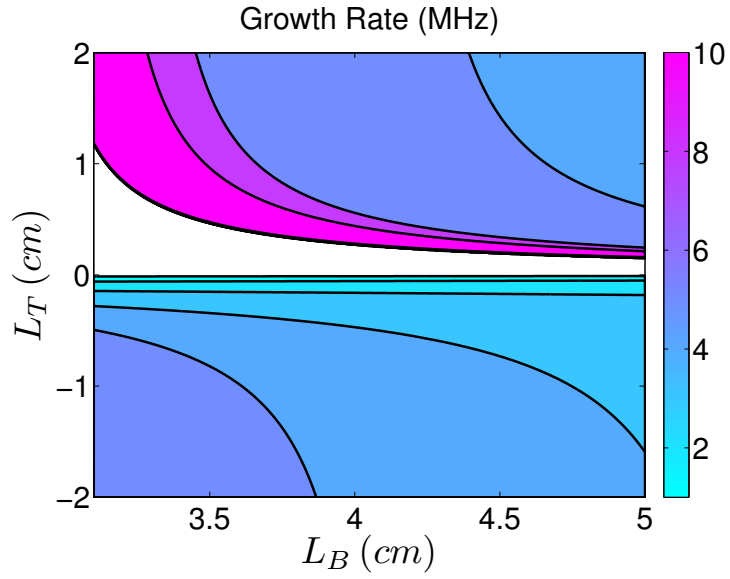

(b)

Figure 3.6: Contour plot of the growth rate as a function of L_B and L_T for L_N =0.5 cm and L_N =1.5 cm.

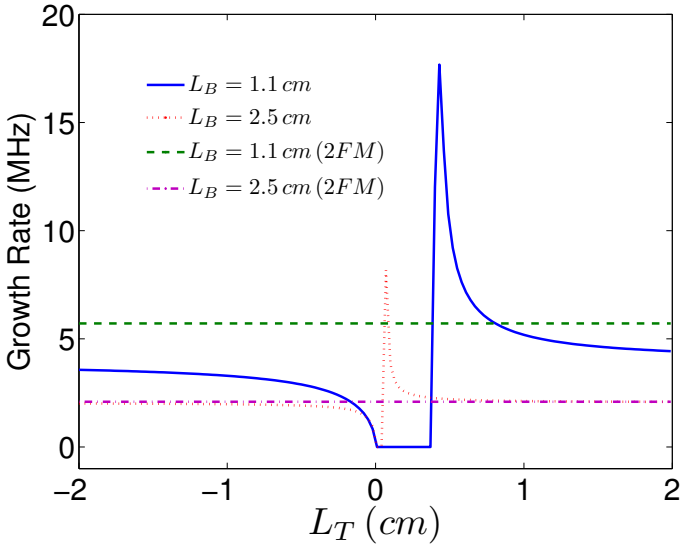

(a)

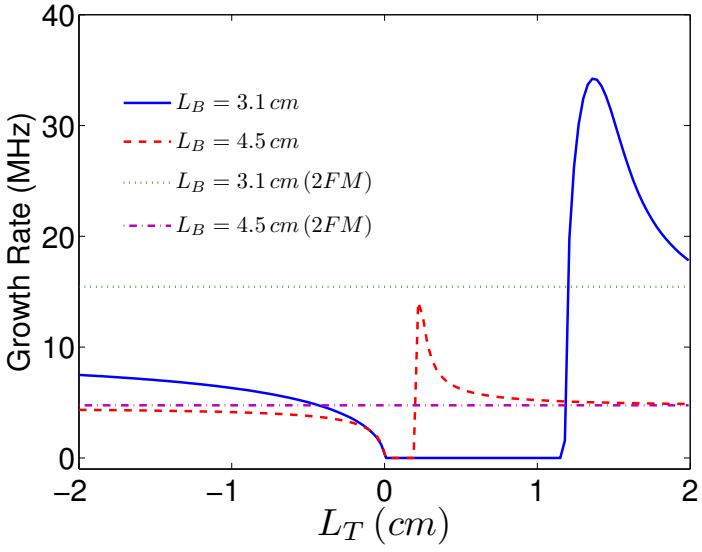

(b)

Figure 3.7: Growth rate as a function of L_T for a) L_N =0.5 cm and b) L_N =1.5 cm, for different values of L_B. The straight lines correspond to the values predicted by the two-field model.

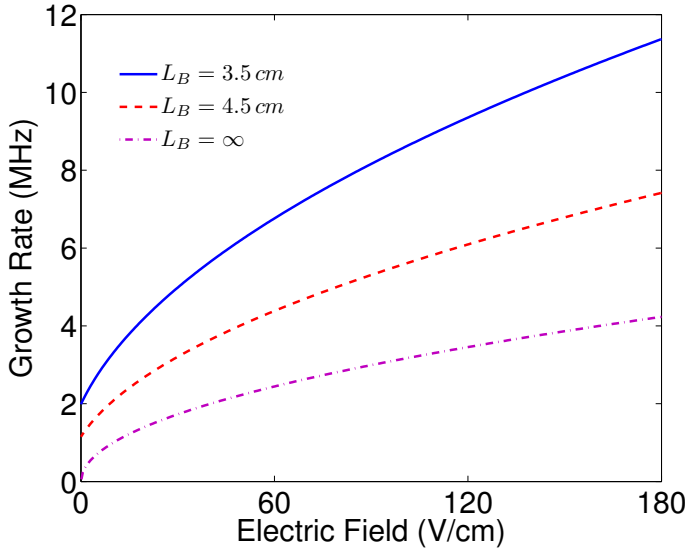

(a)

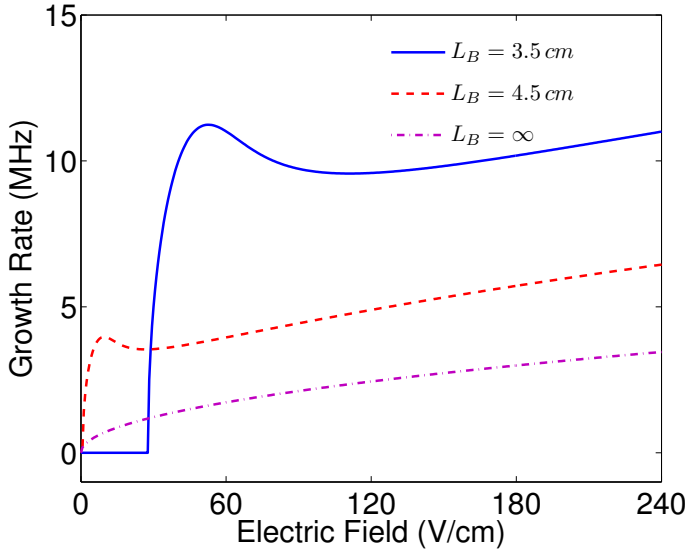

(b)

Figure 3.8: Growth rate as a function of the electric field for L_N =1.5 cm as predicted by a) the two-field model and b) the three-field model, L_T =1 cm.

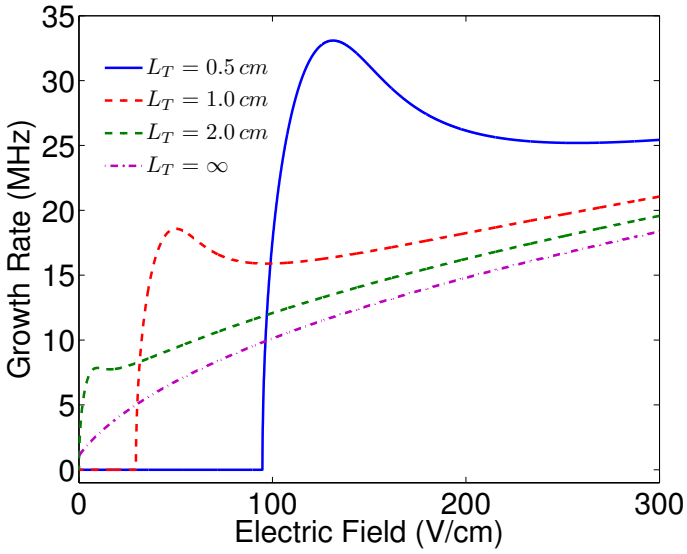

Figure 3.9: Growth rate as a function of electric field for L_N= 2.0 cm, $L_B = 4.5$ cm and different values of L_T.

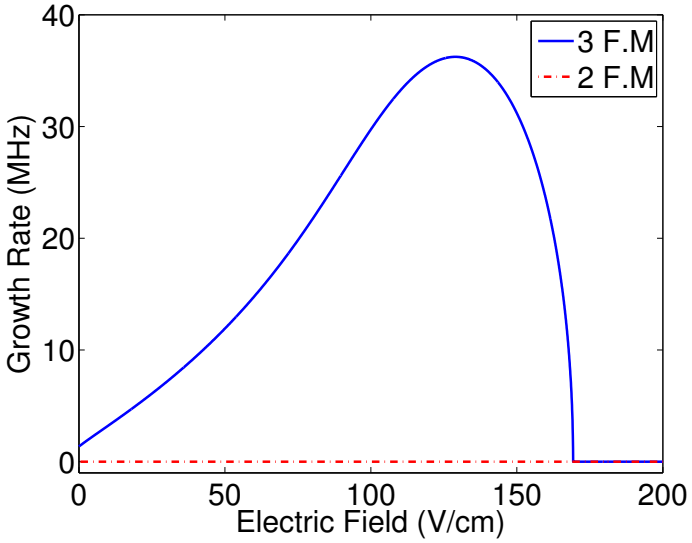

Figure 3.10: Growth rate as a function of electric field as predicted by the three-field model: $L_N = 1.5$ cm, $L_B = 2.9$ cm, $L_T \to \infty$. Two-field model predicts no instability for these parameters.

[5, 6], numerically simulated profiles for the plasma density, potential, electron temperature and magnetic field obtained using the numerical code HPHall-2 for the SPT-100 thruster [7] as well as data from the CAMILA Hall thruster at the Technion-Israel Institute of Technology [8] are used. The analytical results show a complex interaction of plasma and magnetic field gradients in destabilizing the $\mathbf{E} \times \mathbf{B}$ drift flow. In a previous study [54], the density gradient was absent as an independent parameter controlling the instability because the authors of Ref. [54] assumed absence of ionization and neglected the ion flux divergence. Experimental data show that these assumptions are not valid, and, as a result, the theory of Ref. [54] is inapplicable in such regions. The plasma density gradient is retained as an independent parameter, which is critically important for valid predictions of the stability of Hall thrusters.

3.4.1 PPPL Hall Thruster Experiment (HTX)

In Ref. [5], plasma parameters are measured for a 2 kW laboratory Hall thruster at the Princeton Plasma Physics Laboratory. The Hall thruster has a channel length of 46 mm, an outer diameter of 123 mm and a width of 15 mm due to the addition of two boron nitride spacers added to the inner and outer channel walls of the channel. Plasma parameters inside the thruster were measured using emissive and non-emissive electrostatic probes. Plasma parameters in the thruster plume were measured using a flat electrostatic probe of 2.54 cm diameter. The detailed discussion of the experiments and measurements are available from Ref. [5]. The plasma parameters used here are obtained from measurements made at the midpoint between the channel walls. The plasma density, equilibrium $\mathbf{E}_0 \times \mathbf{B}_0$ velocity, $\mathbf{u}_0$, and electron temperature obtained in the experiments reported in Ref. [5] are shown in Fig. 3.11. There are more than 400 measurement points with a distance between each point of 0.02 cm. In these experiments, measurements were done mainly outside the thruster channel, in the plume region from $x = -0.8$ cm to $x = 8.0$ cm (the exit plane is at x=0). The corresponding gradients were calculated by taking a nine-point finite difference numerical derivative (thus with a characteristic averaging length scale of 0.2 cm). The resulting values of the gradients were again averaged. The resulting profiles are shown in Fig. 3.12. For these profiles, the magnetic and electric field reach their peak at around x= 0 and then decay. The plasma density is monotonically decaying as well as the temperature, except for a small region close to x=0. This results in mainly negative gradient lengths in this region as can be seen in Fig. 3.12. With the

gradient lengths, Eqs. (3.18) and (3.40) can be solves and a position dependent growth rate for the instabilities predicted by the two- and three-field models can be obtained. The calculated growth rates are shown in Fig. 3.13 for the two-field model and in Fig. 3.14 for the three-field model.

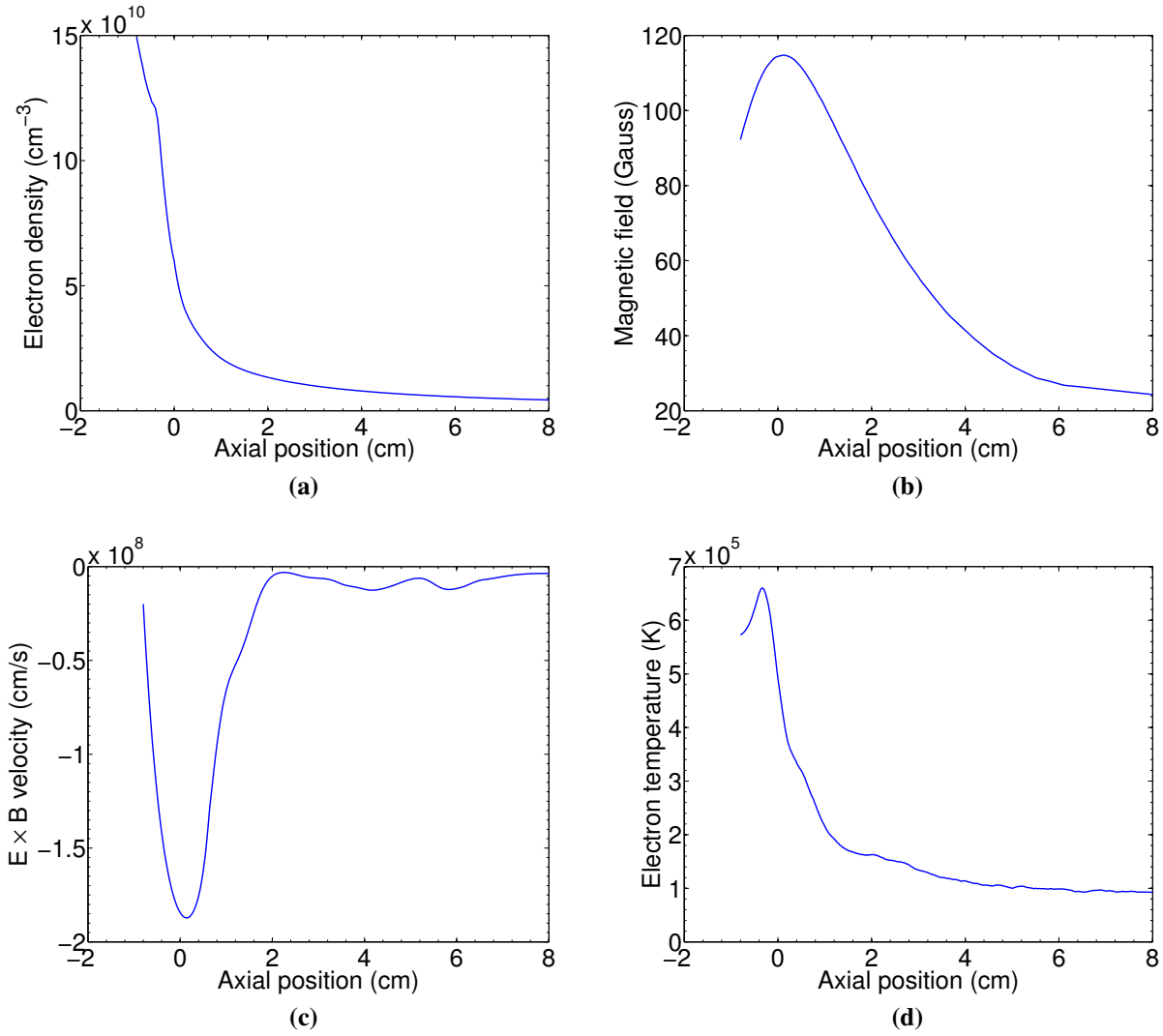

Figure 3.11: Experimental profiles of the plasma density, magnetic field, electron equilibrium drift velocity, u_0, and electron temperature for the HTX thruster [5]. The exit plane is at x=0.

As can be seen from Fig. 3.13, the instability predicted by the two-field model is concentrated in two narrow regions: from x=1.22 cm to x=1.82 cm and from x=5.54 cm to x= 6.22 cm. For the instability to occur, the condition expressed above in Eq. (3.20) have to be met. For the profiles in Fig. 3.11, it is clear that in the region x$<$1.22 cm, the second factor in Eq. (3.20), namely $1/L_N - 2/L_B$ is negative but the first one, $eE_0/T_e + 2/L_B$ is positive, resulting in this region being

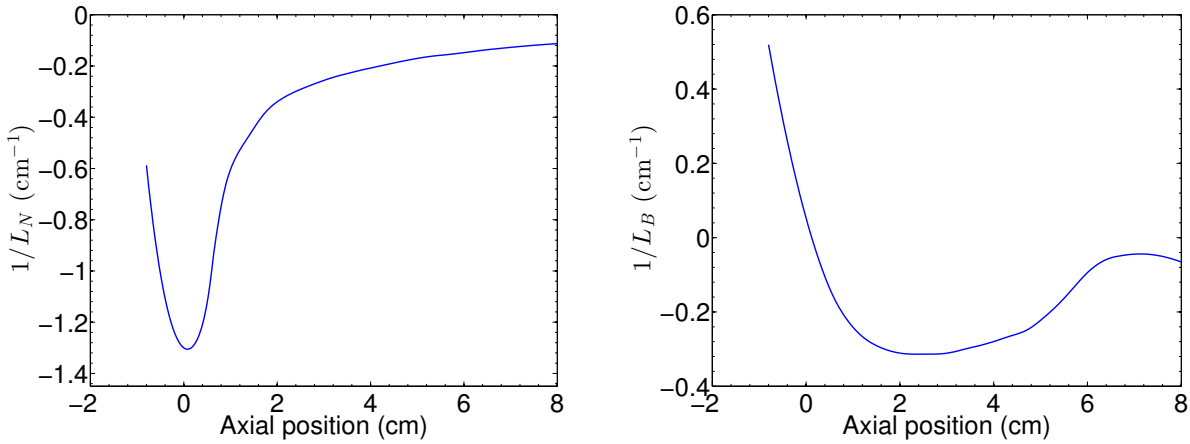

(a)

(b)

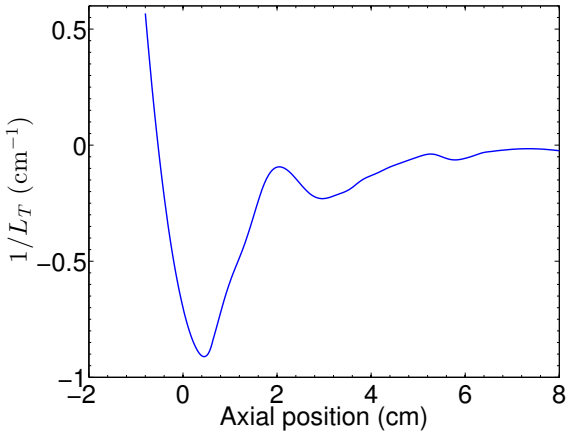

(c)

Figure 3.12: Characteristic gradient lengths for the plume region of the HTX thruster [5]. The exit plane is at x=0.

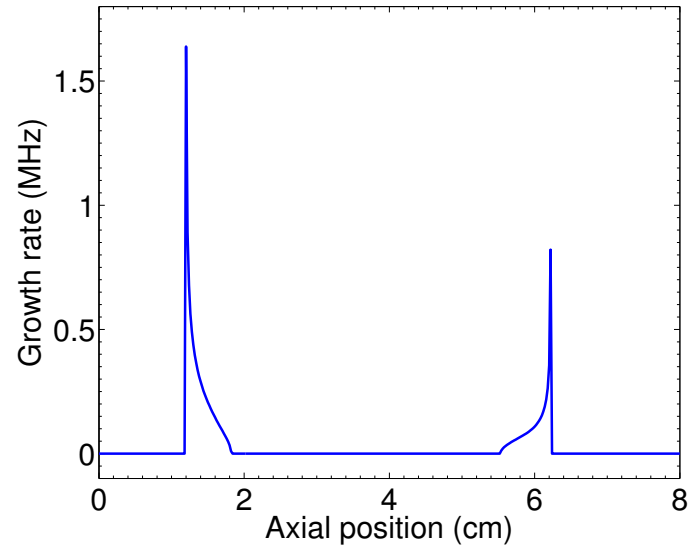

(a)

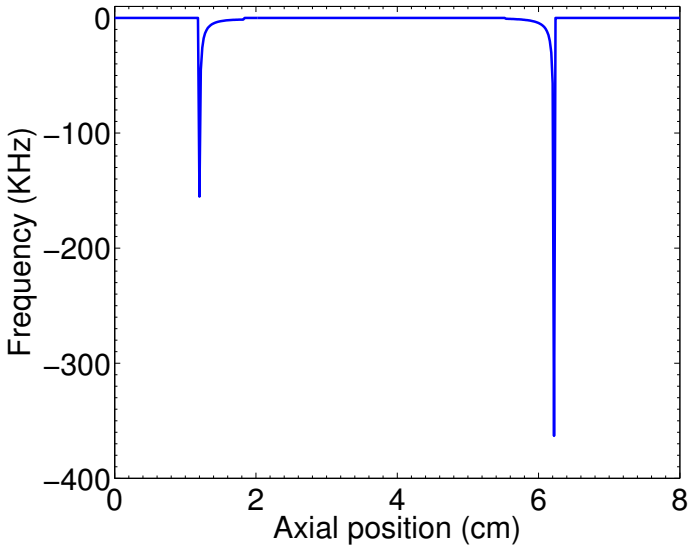

(b)

Figure 3.13: Growth rate and frequency of the instabilities in the HTX thruster [5] as a function of axial distance as predicted by the two-field model. The exit plane is at x=0.

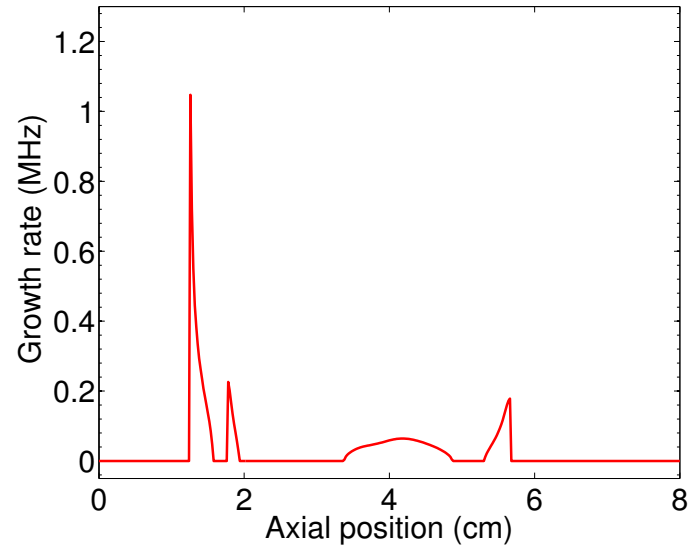

(a)

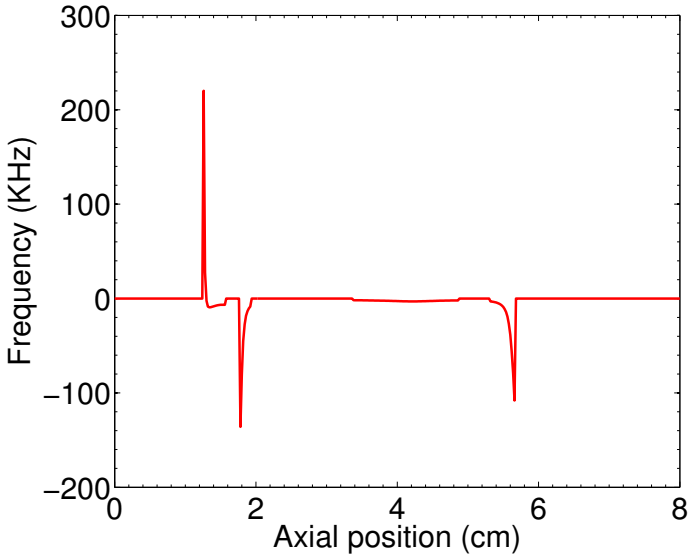

(b)

Figure 3.14: Growth rate and frequency of the instabilities in the HTX thruster [5] as a function of axial distance as predicted by the three-field model. The exit plane is at x=0.

stable. The region between x=1.22 cm and x=1.82 cm is characterized by $1/L_N - 2/L_B > 0$, and $eE_0/T_e + 2/L_B > 0$, resulting in instability. In this region, since the magnetic field is decreasing with distance, L_B is negative and the electric field satisfies the following inequality

$$E_0 > \frac{T_e}{e}\left|\frac{2}{L_B}\right|. \tag{3.52}$$

This last condition suggests that in the plume region, when the magnetic field gradient length L_B is larger than twice the density gradient length L_N, the instability will occur if the electric field is larger than a certain threshold value as expressed by Eq. (3.52). Also, $1/L_N - 2/L_B$ changes sign from negative to positive at x=1.22 cm and $eE_0/T_e + 2/L_B$ changes sign from positive to negative at x=1.82 cm. In the region between x=1.82 cm and x=5.54 cm, $1/L_N - 2/L_B > 0$ but the electric field is smaller than the threshold value, resulting in the instability disappearing in this region. In the region from x=5.54 cm to x=6.22 cm, the electric field is larger than the threshold value and the instability settles again. For x$>$ 6.22 cm, there is that $1/L_N - 2/L_B < 0$ and the instability disappears.

The real part of the frequency predicted by the two-field model is negative, which is to be expected since the real part of the frequency is determined by the sign of $1/L_N - 2/L_B$. This negative frequency suggests that the azimuthal phase velocity is in the same direction as the equilibrium drift velocity u_0.

The instability predicted by the three-field model is concentrated in four regions, from x=1.26 cm to 1.56 cm, from x=1.76 cm to x=1.94 cm, from x=3.34 cm to x=4.88 cm and from x=5.30 cm to 5.68 cm. The maximum growth rate is smaller compared to the growth rate from the two-field model. Also, apart from the region from x=3.34 cm to x=4.88 cm, the unstable region is narrower compared with the unstable region from the two-field model. In the central unstable region, the instability is driven by an unfavorable combination of the different gradient drift velocities. The real part of the frequency is mainly negative except in the region from x=1.26 cm to x=1.30 cm. For typical parameters, the stability conditions are very sensitive to the temperature gradient (within the three-field model). In the region from x=1.26 cm to x=1.30 cm, the product of the temperature and magnetic field gradients, the factor $\omega_D\omega_{*T}$, reaches its maximum value over all other unstable regions (around 3×10^{12} Hz^2), which result in the mode destabilization and change in the rotation direction. However, this feature in the temperature gradient profile, seen Fig. 3.12, is difficult to

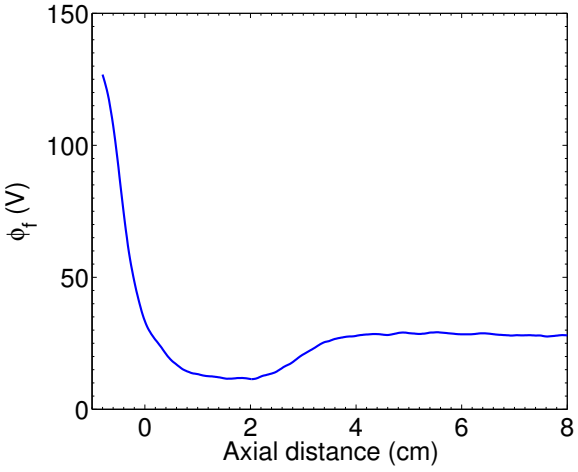

Figure 3.15: Floating plasma potential for the HTX thruster [5]. The well of the plasma potential coincides with the regions where the gradient drift instabilities are strongest. The exit plane is at x=0.

confirm within the experimental measurements error.

The measurements in the HTX thruster reveal the existence of a special feature in the measured floating potential, which is below the plasma potential (for Xe, 5.77 T_e) [6], and shown in Fig. 3.15. The well of the floating potential is located in the region where the growth rate of the instabilities is strongest. This well in the floating potential is related to electron injection and this suggests that there may be a connection between the excitation of the instabilities in the plume region and efficiency of the electron injection in the thruster, which at the same time determines the general discharge characteristics of the device.

3.4.2 Near-anode region of HTX Thruster

There are limited measurements of plasma parameters in the near-anode region of a 12.3 cm, 2 kW Hall thruster. In Ref. [6] measurements of plasma parameters in the near-anode region are presented. In these experiments, three different configurations of the magnetic field were used to study the influence of the magnetic field profile on the anode fall in a Hall thruster. The magnetic field in the thruster is created by one inner and two outer electromagnetic coils. The currents in the inner and in one of the outer coils is kept constant while the current supplied to the another outer

coil, which is placed near the anode, is changed in order to produce three different configurations of the magnetic field, B_0, B_{pos} and B_{neg} [6], as shown in Fig. 3.17. The magnetic field configuration B_0 has negligible magnetic field in the near anode region, the magnetic field for configuration B_{pos} is between 60 and 80 Gauss in the near anode region and between -60 and -80 Gauss for the B_{neg} configuration. In the B_{pos} and B_{neg} configurations, the magnetic field in the near anode region is comparable to the magnetic field in the acceleration region. The cusp configuration of the magnetic field B_{neg} is similar to the magnetic field in other devices such as the Cylindrical Hall Thruster (CHT) [6]. The magnetic field lines for the three configurations can be seen in Fig. 3.16. Plasma measurements were performed in three different axial positions, at 2 mm, 7 mm and 12 mm from the anode and at three different radial positions, at the outer wall, R=62 mm, at the midpoint of the channel, R=49 mm and near the inner wall, R=41 mm. The measured electron temperature and plasma density at the midpoint of the channel are shown in Fig. 3.17 [6]. In this near anode region, the instability seems to be dominated by the gradients in magnetic field, since the variation of electron temperature and density are in general smaller. Because of this reason, only the two-field model is used to study the instabilities in this region. The corresponding growth rates and frequencies are plotted in Figs. 3.18 and 3.19

It is clear that the growth rate for profile B_0 is zero, which can be expected since the equilibrium $\mathbf{E} \times \mathbf{B}$ velocity is zero. For the B_{pos} configuration, both the magnetic and density gradient lengths are positive and the growth rate has the values 1.64 MHz, 2.69 MHz and 3.96 MHz at the axial positions x=2 mm, 7 mm and 12 mm from the anode respectively. For the B_{neg} configuration the magnetic field and density gradients are both positive and the growth rates at axial positions x=2 mm, 7 mm and 12 mm from the anode are 0.99 MHz, 2.0 MHz and 2.5 MHz, respectively. The frequencies are -4.38 KHz, -13.33 KHz and -31.92 KHz for B_{pos} at x=2 mm, 7 mm and 12 mm and 1.47 KHz, 6.89 KHz and 11.65 KHz at x=2 mm, 7 mm and 12 mm.

3.4.3 SPT-100 thruster simulations

To investigate the plasma stability plasma parameters in the discharge chamber and the near plume region obtained from simulations of SPT-100 Hall thruster with the HPHall-2 code as reported in Ref. [7] are used. HPHall-2 is a modification [74] of the hybrid fluid/PIC axisymmetric code HPHall [75] that includes more up-to-date wall-sheath and electron mobility models. As reported

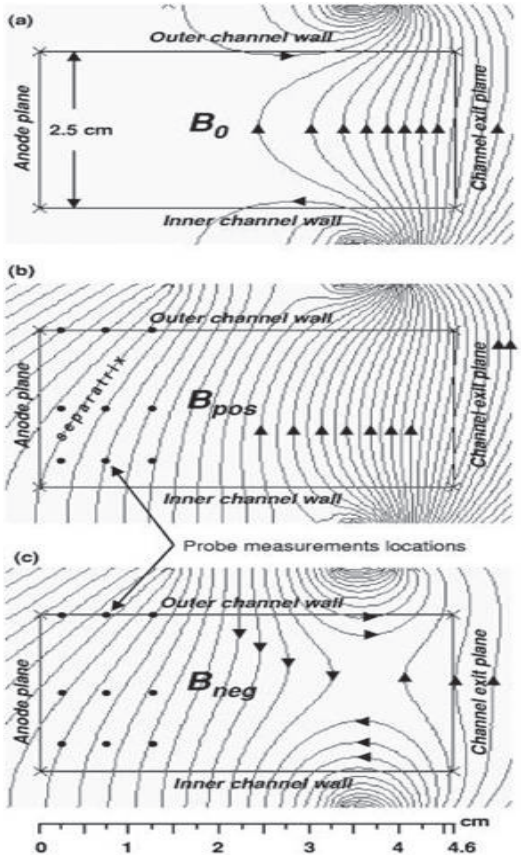

Figure 3.16: Magnetic field lines in the 12.3 cm Hall thruster for three magnetic field configurations: B_0, B_{pos}, and B_{neg}. All diagrams are drawn to scale. Figure taken from [L. Dorf $etal.$, Phys. Plasmas **13**, 057104 (2006)] [6].

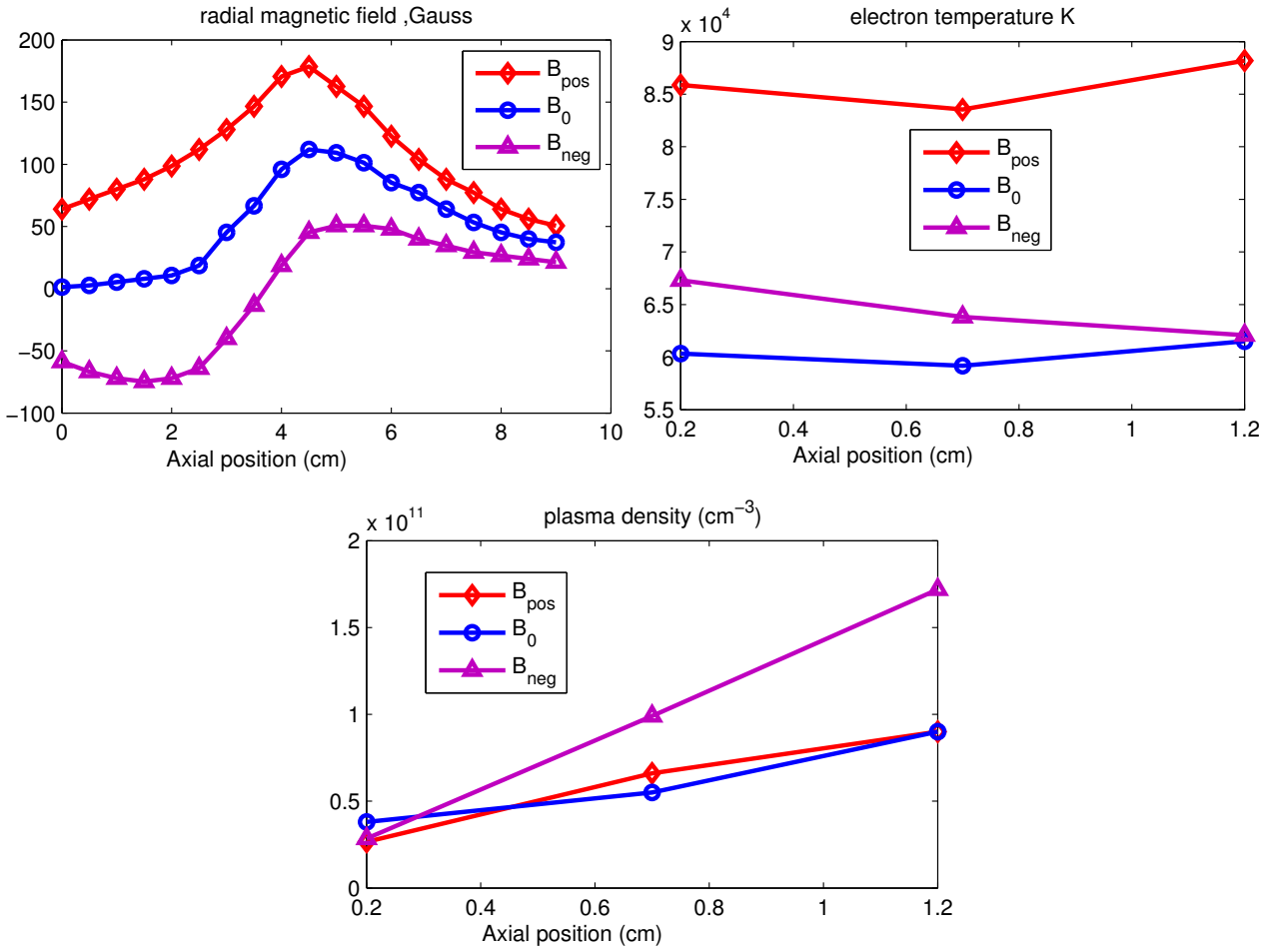

Figure 3.17: Three different profiles for magnetic field configuration and electron density and temperature measured at the midpoint between the channel walls as reported in Ref. [6].

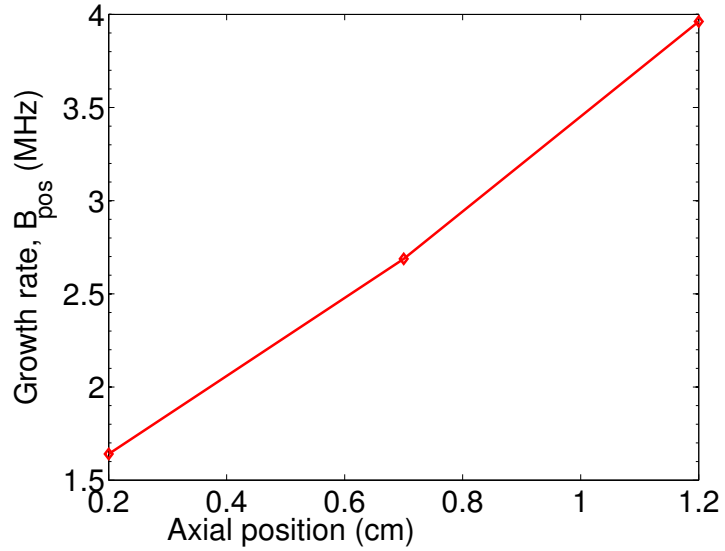

(a)

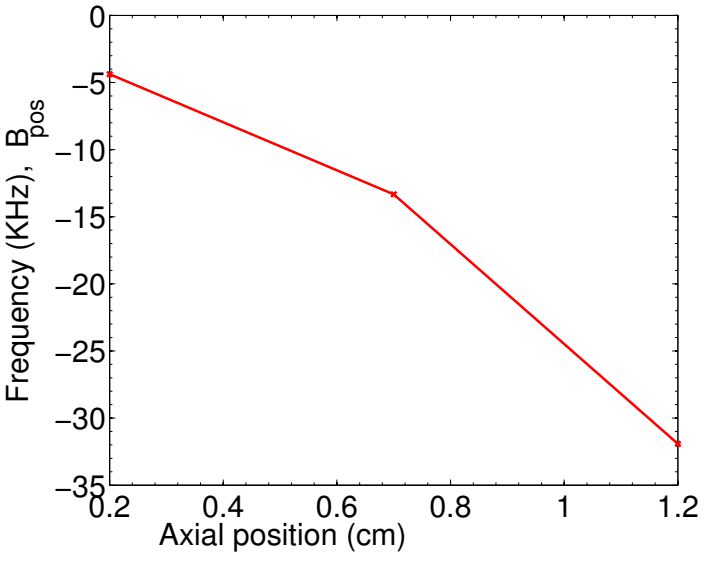

(b)

Figure 3.18: Growth rate and frequency of the instabilities as a function of axial distance as predicted by the two-field model for the positive magnetic field profile in Fig. 3.17.

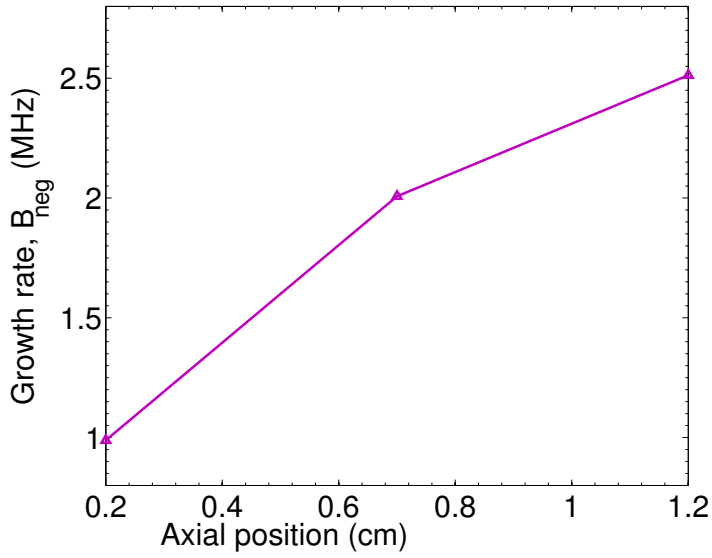

(a)

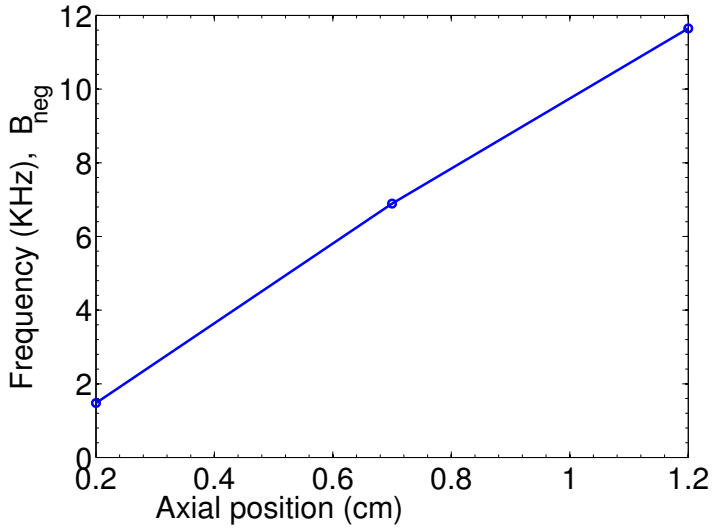

(b)

Figure 3.19: Growth rate and frequency of the instabilities as a function of axial distance as predicted by the two-field model for the negative magnetic field profile in Fig. 3.17.

in Ref. [7], the obtained plasma profiles are in good agreement with the available experimental data for the SPT-100 thruster. Furthermore, the code has been able to reproduce with good agreement the performance parameters of the SPT-100 thruster [7]. The numerically obtained plasma parameters profiles are shown in Fig. 3.20.

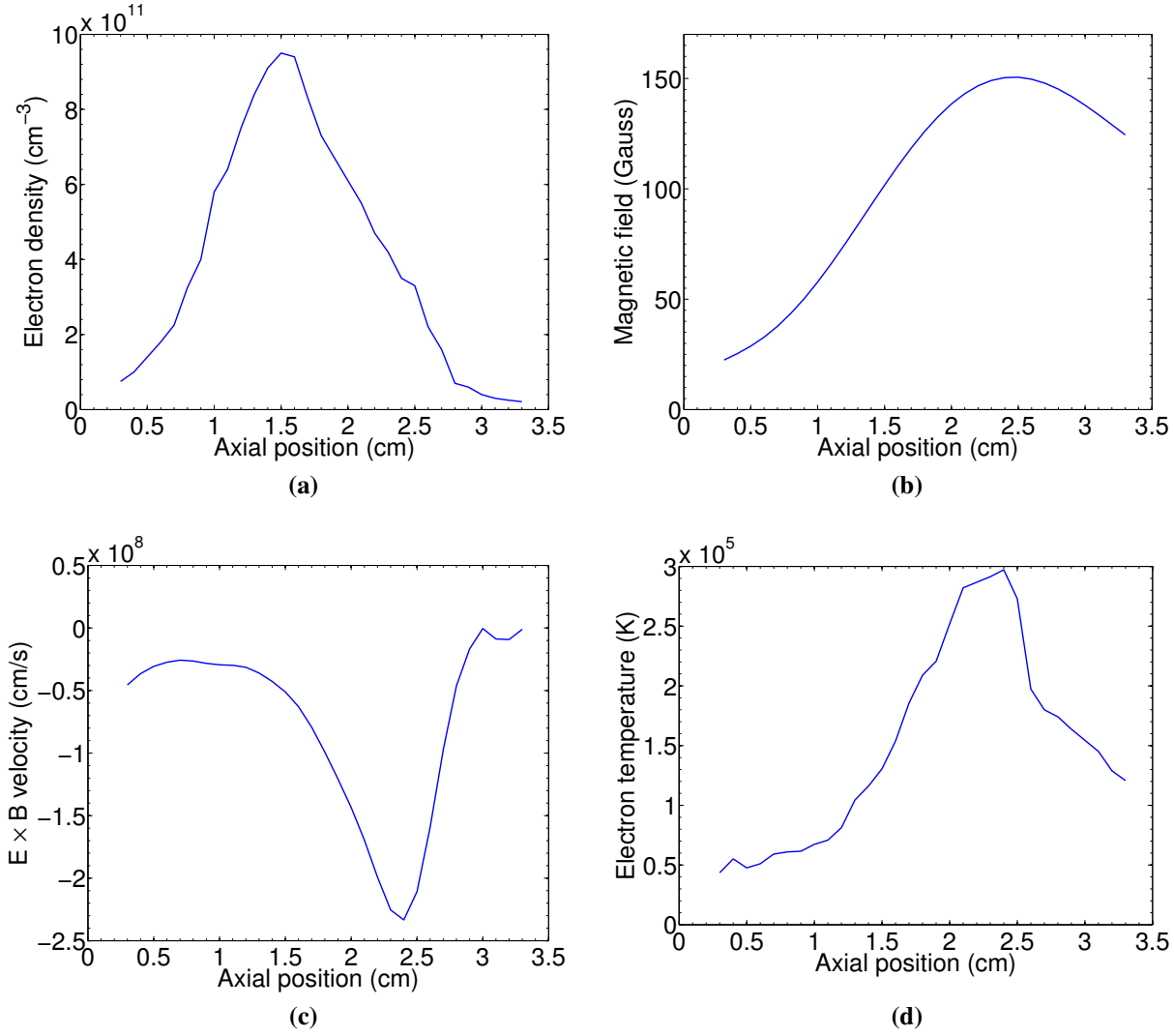

Figure 3.20: Plasma density, magnetic field, electron equilibrium drift velocity, u_0, and electron temperature profiles in SPT-100 Hall thruster obtained from HPHall-2 simulations as shown in Fig. 10 from Ref. [7]. The exit plane is at x=2.5 cm.

The magnetic field is positive and increasing with distance in the channel region, reaching a maximum at the channel exit and decreasing in the plume region, which results in a positive magnetic field gradient length $L_B = (\partial \ln B/\partial x)^{-1} > 0$ inside the channel and in a negative magnetic field gradient length $L_B = (\partial \ln B/\partial x)^{-1} < 0$ in the plume region. The plasma den-

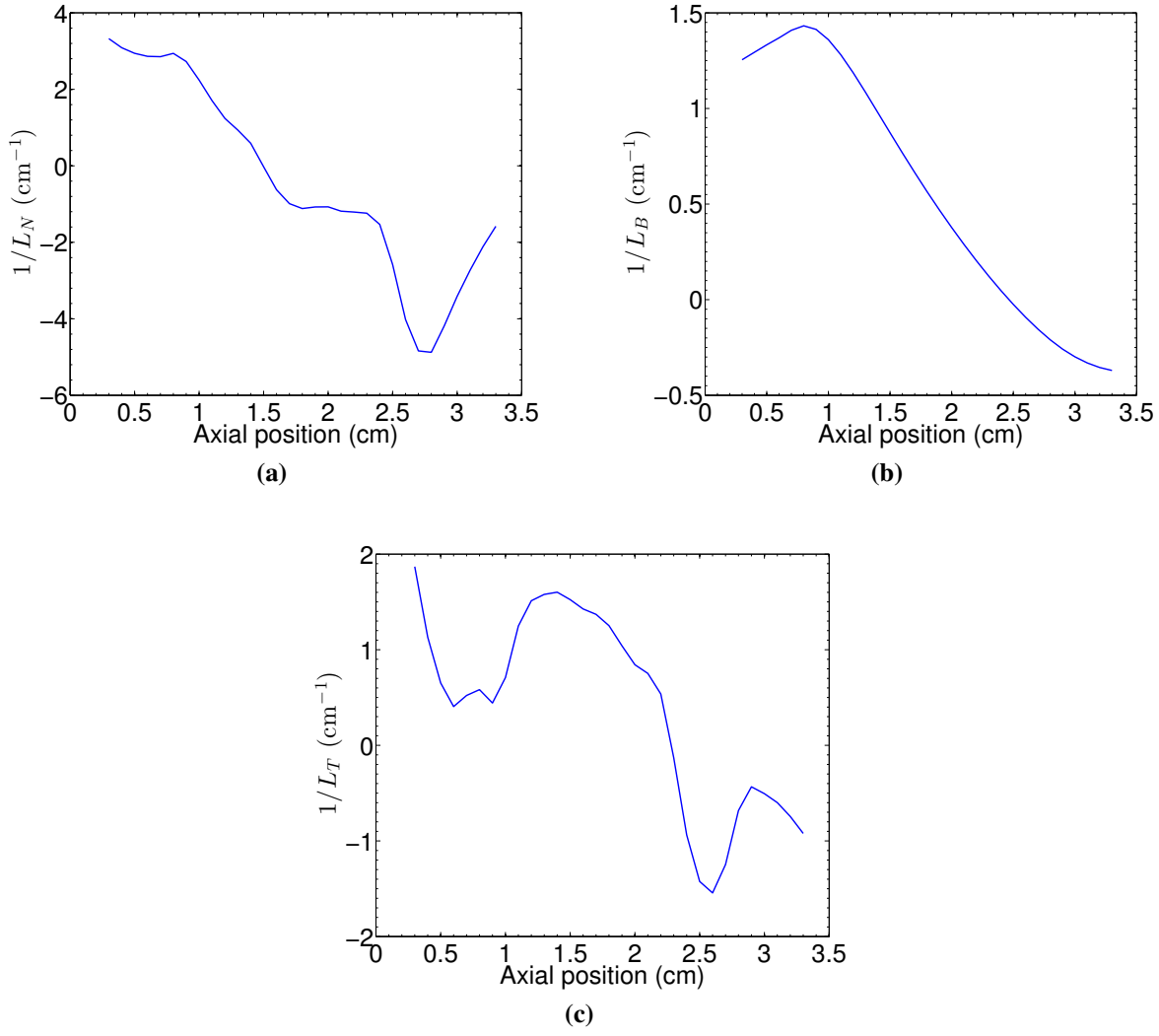

Figure 3.21: Gradient lengths for the SPT-100 Hall thruster. The exit plane is at x=2.5 cm.

sity reaches its maximum value at a distance of x=1.5 cm from the anode, decreasing afterwards, resulting in a positive density gradient length $L_N = (\partial \ln n/\partial x)^{-1} > 0$ from x=0.03 cm to x= 1.5 cm and in a negative density gradient length $L_N = (\partial \ln n/\partial x)^{-1} < 0$ after x=1.5 cm. There is, then, a region between x=1.5 cm to x=2.5 cm where the density and magnetic field gradient lengths are of opposite signs, with the density gradient length being negative and the magnetic field gradient length being positive. This region is expected to be stable. The electron temperature reaches its maximum value also at the exit plane, resulting in a positive temperature gradient length $L_T = (\partial \ln T_e/\partial x)^{-1} > 0$ inside the channel and in a negative temperature gradient length $L_T = (\partial \ln T_e/\partial x)^{-1} < 0$ in the plume. Similarly to the magnetic field and electron temperature, the electric field reaches its maximum value at the exit plane. The gradient lengths for the plasma parameters from Fig. 3.20 are plotted in Fig. 3.21.

The growth rate and frequency (of the unstable modes only) calculated by solving Eqs. (3.18) and (3.40) are shown in Figs. 3.22 and 3.23.

For the profiles shown in Fig. 3.20, there is an unstable region inside the channel from x=0.03 cm to x=0.8 cm, that is close to the anode. This instability growth rate is in the 100-450 KHz range, the growth rate being larger when the temperature gradients are not considered. In this region, $1/L_N - 2/L_B > 0$ and since the electric field and the magnetic field gradient length are both positive, the factor $eE_0/T_e + 2/L_B$ is positive, resulting in instability. The real part of the frequency is determined by the sign of $1/L_N - 2/L_B$. In the unstable region from x=0.03 cm to x=0.8 cm, the frequency is negative due to the factor $1/L_N - 2/L_B$ being positive. For x between 0.8 cm and 2.5 cm (exit plane), the plasma density decreases with distance while the magnetic field is still increasing, resulting in density and magnetic field gradient lengths of opposite signs. In this region, $1/L_N - 2/L_B$ changes sign, becoming positive, while at the same time $eE_0/T_e + 2/L_B$ remains positive, killing the instability. After the magnetic field reaches its maximum value at the exit plane, the magnetic field gradient length becomes negative. From x=2.5 cm to x=3.0 cm, $1/L_N - 2/L_B < 0$, but the electric field is larger than the threshold value $2T_e/e|L_B|$ resulting in this region being stable.

The growth rate predicted by the three-field model is concentrated in the regions from x=0.03 to x=0.9 cm and from x=3.0 to x=3.2 cm. In the first region the growth rate predicted by the three-field model is considerably smaller than the one predicted by the two-field model (maximum

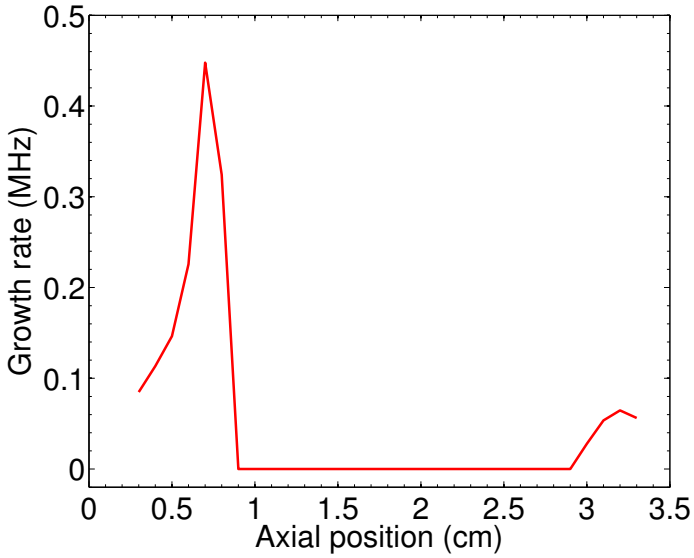

(a)

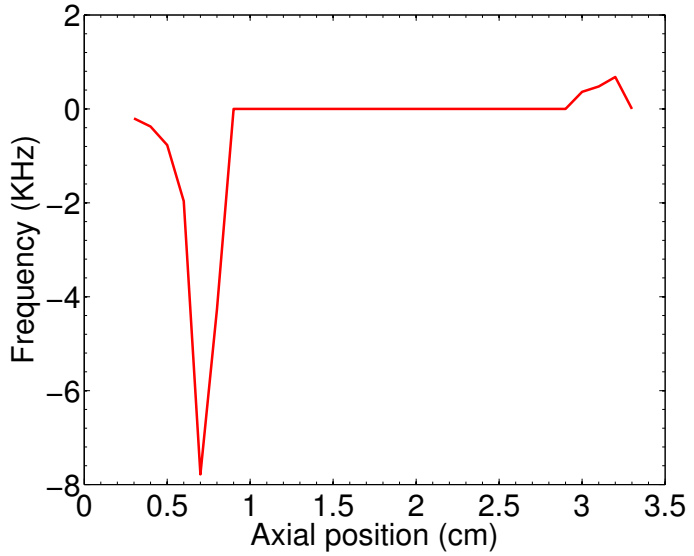

(b)

Figure 3.22: Growth rate and frequency of the instabilities in a SPT-100 thruster [7] as a function of axial distance to the anode as predicted by the two-field model. The exit plane is at x=2.5 cm.

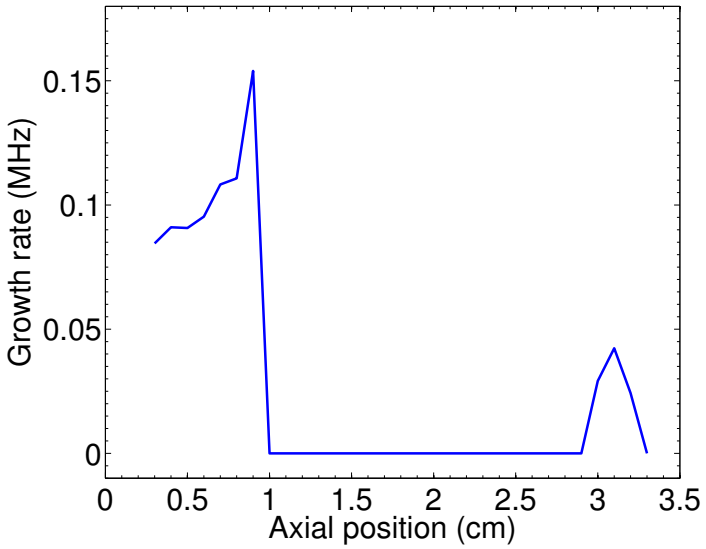

(a)

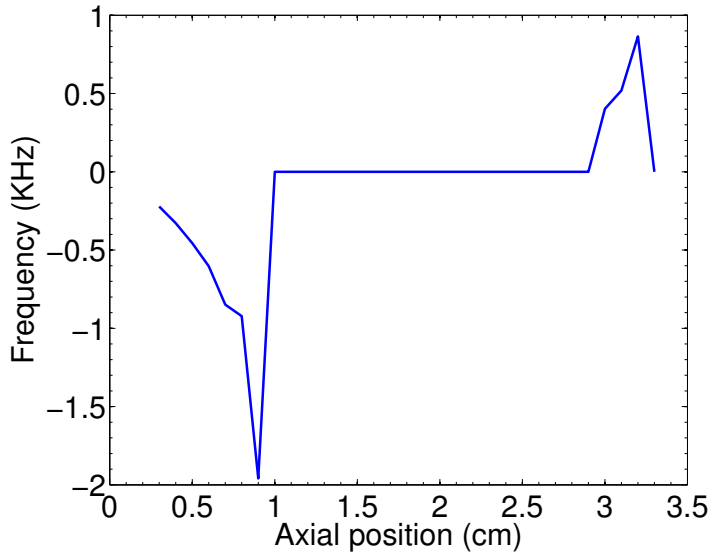

(b)

Figure 3.23: Growth rate and frequency of the instabilities in a SPT-100 thruster [7] as a function of axial distance to the anode as predicted by the three-field model. The exit plane is at x=2.5 cm.

values of 450 KHz and 154 KHz), whereas in the second region, the growth rate predicted by the two-field model is just slightly larger (maximum values of 64 KHz and 43 KHz). The real part of the frequency predicted by the three-field model follows the same pattern as the one predicted by the two-field model. In the unstable region in the near anode region, from x=0.03 cm to x=0.8 cm, the frequency is negative.

There is an interesting feature in the region between x=3.0 cm and x=3.2 cm, where the unstable modes propagate with positive frequency. The change of the direction of the rotation is not related to temperature gradients (as was the case in the HTX plume region, see Fig. 3.13b)), which is small in this region and, therefore, the two- and three-field model give similar results. In this region, the electric field, within the accuracy of the measurements, is smaller than the threshold electric field, $E < E_{thr}$ (situation unique among all the investigated regions), and the instability criterion is simply determined by the sign of the factor $1/L_N - 2/L_B$; the mode is unstable for $1/L_N - 2/L_B < 0$. The sign of the real part of the frequency is only determined by the sign of $1/L_N - 2/L_B$, so that the unstable modes propagate with positive frequency (in the direction opposite to $\mathbf{E}_0 \times \mathbf{B}_0$). Generally, the two-field model predicts that the direction of propagation of unstable modes is directly linked to the sign of the quantity $(\mathbf{E}_0 - \mathbf{E}_{thr}) \times \mathbf{B}_0$, thus negative (in the direction of $\mathbf{E}_0 \times \mathbf{B}_0$ flow) for $E_0 > E_{thr}$, and positive when $E_0 < E_{thr}$. Some experiments with $\mathbf{E}_0 \times \mathbf{B}_0$ plasmas do show the presence of fluctuations with rotation in the direction opposite to $\mathbf{E}_0 \times \mathbf{B}_0$ drift [76]. Since the results here presented are very sensitive to the details of plasma parameters profiles, at this time it cannot be confirmed that profiles measurements and postprocessing, (e.g. profiles gradients) are accurate enough to make conclusive statements regarding the robustness of the rotation against the direction of $\mathbf{E}_0 \times \mathbf{B}_0$ in the experimental conditions here discussed. Indeed, a small perturbation of the plasma plume (induced by the probe, for example) could alter these measurements. More accurate measurements are needed to corroborate the predictions of our model.

3.4.4 CAMILA thruster simulations

The coaxial magnetoisolated longitudinal anode thruster (CAMILA), developed at the Technion's Asher Space Research Institute is an effort to adapt Hall thruster technology to low power regimes [8]. In this device, two concentric cylindrical electrodes are used as an anode. The thruster channel

consists of the anode cavity and the dielectric walls of the thruster. The magnetic circuit produces a longitudinal magnetic field inside the anode cavity, thus reducing the electron mobility in the radial direction. A radial electric field is created in the direction towards the center of the channel. The radial electric field will increase electron energy in such a way that the gas inside the cavity will be ionized. One advantage of this configuration is that the whole length of the channel can be used for ionization. Two configurations are currently under development, simplified CAMILA, without anode coils and full CAMILA, with anode coils. The following discussion refers to the simplified version of the thruster. A more detailed description of the CAMILA concept can be found in Ref. [8] and references therein. The plasma parameter profiles for the CAMILA thruster are shown in Fig. 3.24.

The magnetic field is positive and increasing with distance in the channel region, reaching its maximum value at the channel exit, located at x=0, which results in a positive magnetic field gradient length $L_B = (\partial \ln B/\partial x)^{-1} > 0$ inside the channel, except for the region from x=-3.0 to -2.9 cm. The plasma density reaches its maximum value at a distance of x=-0.8 cm from the exit plane, decreasing afterwards, resulting in a positive density gradient length $L_N = (\partial \ln n/\partial x)^{-1} > 0$ from x=-3.0 cm to x=-0.8 cm and in a negative density gradient length $L_N = (\partial \ln n/\partial x)^{-1} < 0$ from x=-0.8 cm up to the exit plane. There is, then, a region between x= -3.0 and -2.9 and x=-0.8 cm to x=0 where the density and magnetic field gradient lengths are of opposite signs, with the density gradient length being negative and the magnetic field gradient length being positive. The instability is not present in this region. The electron temperature reaches its maximum value close to the exit plane, at x=-0.4 cm, resulting in a positive temperature gradient length $L_T = (\partial \ln T_e/\partial x)^{-1} > 0$ for most of the region under consideration. Similarly to the magnetic field and electron temperature, the electric field reaches its maximum value at the exit plane. The gradient lengths for the plasma parameters from Fig. 3.24 are plotted in Fig. 3.25.

One peculiarity of the CAMILA magnetic field is the additional presence of an axial component. This way, the magnetic field B_0 in the dispersion relations, Eqs. (3.18) and (3.40) refers to the magnitude of the field. The growth rate and frequencies of the unstable modes calculated by solving Eqs. (3.18) and (3.40) are shown in Figs. 3.26 and 3.27.

For the profiles shown in Fig. 3.24, there are two unstable regions close to the anode. The first of these regions corresponds to the interval from x=-2.8 cm to x=-2.5 cm, where the maximum

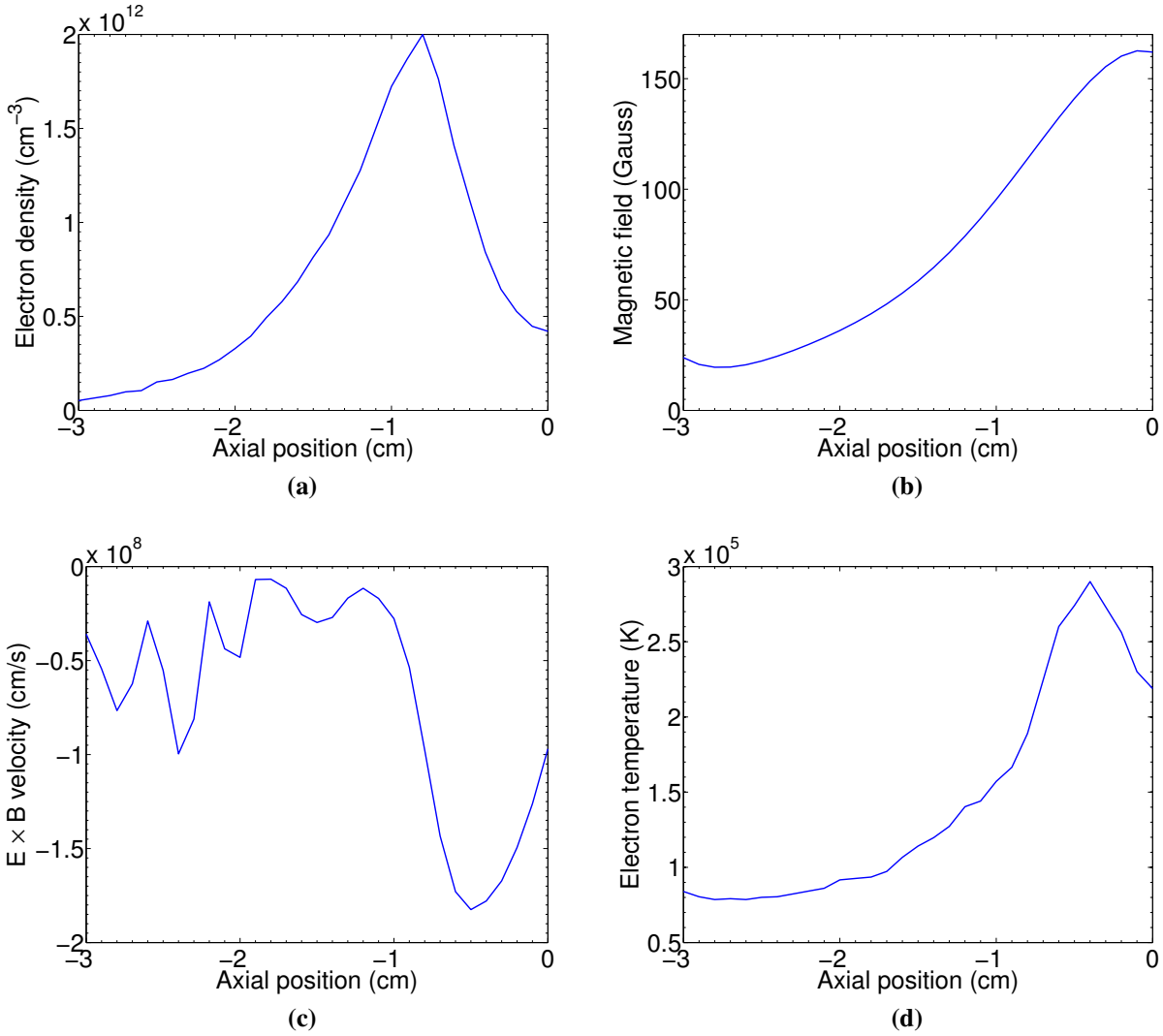

Figure 3.24: Plasma density, magnetic field, electron equilibrium drift velocity, u_0, and electron temperature profiles in CAMILA Hall thruster from Ref. [8]. The exit plane is at x=0.

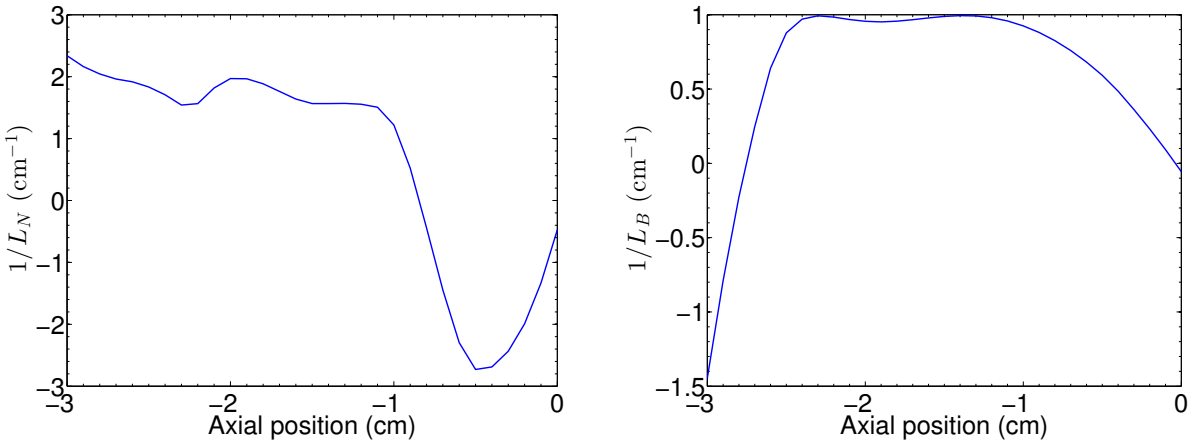

(a)

(b)

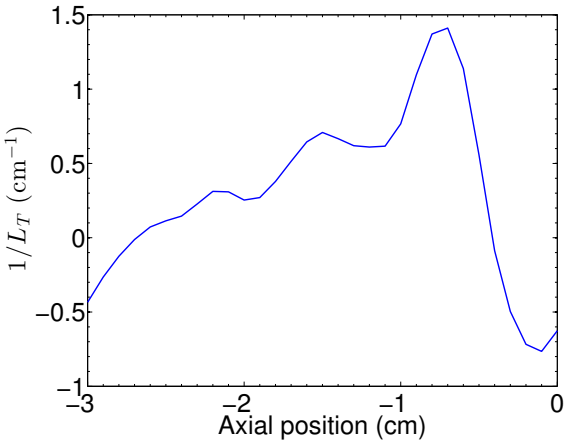

(c)

Figure 3.25: Gradient lengths for the channel region of CAMILA Hall thruster. The exit plane is at x=0.

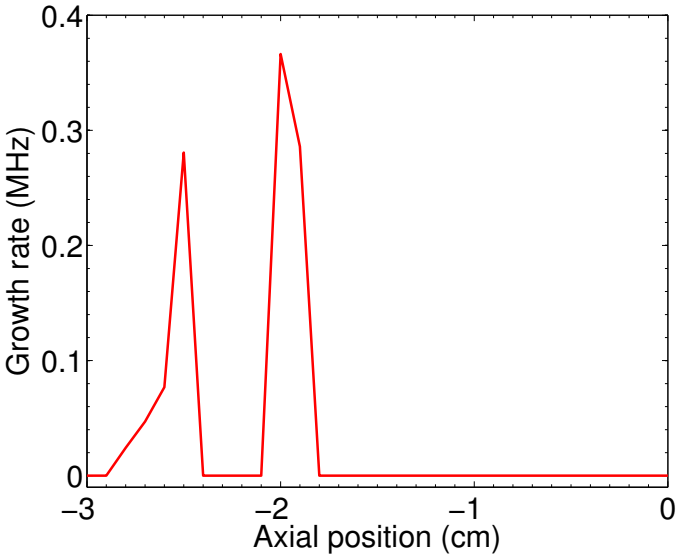

(a)

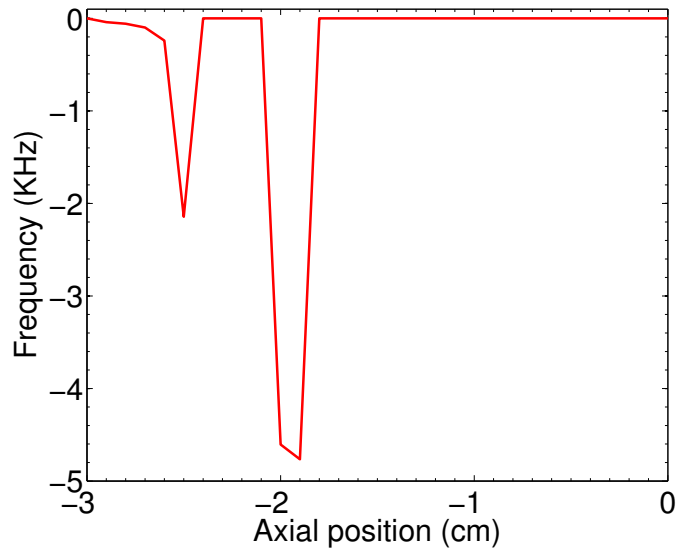

(b)

Figure 3.26: Growth rate and frequency of the instabilities in the CAMILA thruster [8] as a function of axial distance to the anode as predicted by the two-field model. The exit plane is at x=0.

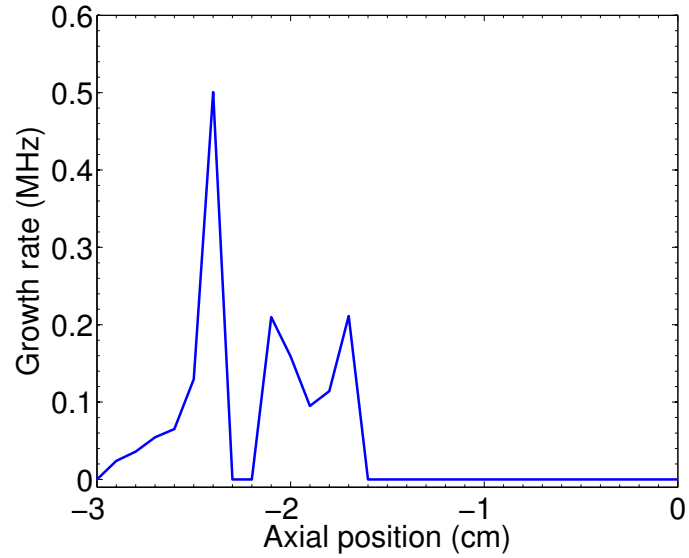

(a)

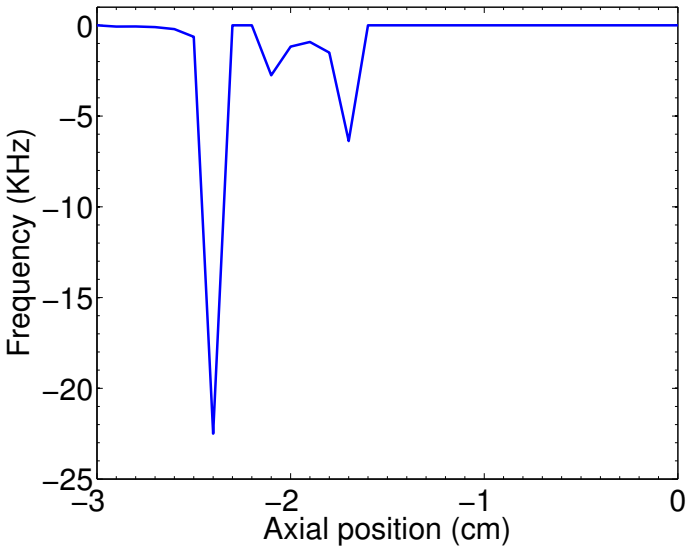

(b)

Figure 3.27: Growth rate and frequency of the instabilities in the CAMILA thruster [8] as a function of axial distance to the anode as predicted by the three-field model. The exit plane is at x=0.

value for the growth rate is 280 KHz at x=-2.5 cm. The second unstable region corresponds to the interval from x=-2.0 cm to x=-1.9 cm, where the peak of the growth rate is 367 KHz at a position x=-2.0 cm. These two unstable regions have $1/L_N - 2/L_B > 0$ and since the electric field and the magnetic field gradient length are both positive, the factor $eE_0/T_e + 2/L_B$ is positive, resulting in the appearance of the instability. For x between -1.9 cm and the exit plane, the plasma density decreases with distance while the magnetic field is still increasing, resulting in density and magnetic field gradient lengths of opposite signs. In this region, the factor $1/L_N - 2/L_B$ becomes negative while $eE_0/T_e + 2/L_B$ remains positive, resulting in the disappearance of the instability. In the unstable regions, since $1/L_N - 2/L_B > 0$, the real part of the frequency is negative.

Using the three-field model, the instability exists from x=-2.9 cm to x=-2.4 cm and has a maximum value of 508 KHz at x=-2.4 cm and from x=-2.1 cm and -1.7 cm, with a maximum value of 210 KHz at x= -1.7 cm. Similar to the previous examples, the growth rate of the instability is smaller when the temperature gradients are considered, but in this case, the unstable region is continuous and somewhat broader than that of the two-field model. For the three-field model, the real part of the frequency is negative.

3.5 Summary

Understanding of the turbulent electron mobility requires a detailed knowledge of the spectra of unstable modes and their saturation levels. Quantitative information about the conditions for linear instabilities and mode eigenvalues (real part of the frequencies and growth rates) is thus of interest. Earlier works in instabilities in Hall thruster plasmas revealed the plasma density and magnetic field gradients as important sources of long wavelength plasma instabilities. This problem is revisited and a modified criterion for this instability is derived. The fluid model is extended to include the dynamics of electron temperature and a three-field fluid model that includes the electron energy equation is developed. The inclusion of two moments, density and temperature, provides a more accurate model of the electron response. Such two-moment model, (n, T), amounts to the two-pole approximation of the exact kinetic response and provides a reasonably accurate description of the exact kinetic response away from the resonances [77]. Such models were shown to be successful in describing a wide class temperature gradient modes in fusion plasmas [77]. The possible role of

the resonances has to be investigated with a kinetic model.

The analysis done in this chapter shows that by including the effects of a finite temperature gradient, the instability criterion is modified, especially near the marginal stability boundary. When temperature gradients are taken into account, there are unstable regions that were found to be stable when only density and magnetic field gradients were taken into account.

It is important to note that gradient-drift instabilities predicted by the model here presented are mostly aperiodic modes with $\gamma \gg \omega_r$. The two-field model predicts that the real part of the frequency explicitly depends on the density and magnetic field gradient lengths and on the magnitude of the external magnetic field, but not on the magnitude of the equilibrium electric field, $\omega_r \simeq -\left(k_\perp^2/k_y\right)\omega_{ci}\left(L_N^{-1} - 2L_B^{-1}\right)^{-1}$. Experimental observations [12,57,78] show an inverse dependence of the real part of the frequency on the magnetic field and an increase with the electric field. The scaling predicted by the model shows the dependence on the magnetic field but not on the electric field, though the electric field dependence might be implicit from the dependence on the gradient lengths. These scaling features are similar when temperature gradients are included. These modes have a real part of the frequency that is consistent with an azimuthal phase velocity in the same direction as, but significantly smaller than the equilibrium $\mathbf{E} \times \mathbf{B}$ drift velocity. Similar trends have been observed experimentally [61], even though, these trends were explained on the basis of the cyclotron instabilities driven by the equilibrium electron drift.

As it was done in the previous work presented in Refs. [9, 27, 54] the electron inertia in the transverse electron current as well as the parallel electron flow are neglected . The latter assumption is equivalent to the condition that the wave vector component $k_{||}$ along the magnetic field is zero, while by neglecting the electron inertia, the low hybrid modes are eliminated. These conditions are equivalent to the model of thermalized magnetic field lines introduced in [1, 17, 25].

The dispersion relations for the two and three-field models were used to study the instabilities in four different Hall thruster configurations, using experimental and simulations results. It is interesting that for all configurations, the instabilities are in the near anode and in the plume regions, where the gradient lengths are of the same sign, the gradient length being positive for the near anode region and negative in the plume region. Additionally, the instability exists in regions between the change of sign of either one of the factors $1/L_N - 2/L_B$ and $eE_0/T_e + 2/L_B$, with sharp peaks in the regions where there is a change of the sign in the factor $1/L_N - 2/L_B$. This condition follows

from Eq. (3.20), where both factors $1/L_N - 2/L_B$ and $eE_0/T_e + 2/L_B$ are required to be of the same sign. One important result of this fact being that the Morozov condition predicts instability in a wider spatial region than the one predicted by the model developed in this chapter. In the plume region, where the magnetic field gradient length is negative, when the factor $1/L_N - 2/L_B$ is positive, the instability requires that the electric field be larger than a certain threshold value given by $E_{0,thr} = 2T_e/e|L_B|$. If the contrary happens, that is that $1/L_N - 2/L_B < 0$, like in the unstable region in the plume of the SPT-100 thruster, the instability occurs if the electric field is smaller than the threshold $E_{0,thr} = 2T_e/e|L_B|$. In the near anode region, since the magnetic field gradient length and the factor $eE_0/T_e + 2/L_B$ (for $E_0 > 0$) are positive, the instability requires that $1/L_N - 2/L_B > 0$.

The highest growth rates are observed in the plume region for the HTX thruster and in the near anode region for the SPT-100 and CAMILA thrusters. In all thrusters, the addition of temperature gradients reduces the peak value of the instability, with the reduction being as much as 40 $\%$ for the plume region of the HTX thruster, 60 $\%$ for the near anode region of the SPT-100 thruster and 50 $\%$ for CAMILA. In the near anode region of the HTX thruster, the magnetic field gradient dominates over the density and temperature gradients and the predictions of the two- and three-field model do not differ considerably.

The conditions for the instability are different depending on the sign of plasma density and magnetic field gradients. The particular conditions existing in the different thrusters under consideration are summarized in Table 3.1. In the near anode region, where the gradients of the magnetic field and density are both positive, the instability is driven by large density gradient, while the magnetic field gradient is stabilizing. In the plume region, where the gradients of the magnetic field and density are both negative, either magnetic field gradient or the density gradient can be destabilizing, depending on the amplitude of the electric field.

The azimuthal phase velocity of the instabilities, defined as ω_r/k_y has a peak value of around -15000 m/s for the plume region of HTX (outside the thruster channel). For the anode region of the HTX the azimuthal phase velocity is -1500 m/s with the B_{pos} configuration and 600 m/s with the B_{neg} configuration. The azimuthal phase velocity in the thruster channel reaches a maximum value of around -400 m/s for the SPT-100 and of - around -250 m/s for CAMILA. These values are close to the azimuthal phase velocities for the rotating spoke instability observed inside the

Thruster	**Near Anode** (L_B, $L_N > 0$)	**Plume** (L_B, $L_N < 0$)
HTX [5]	no data	I
HTX [6]	I	no data
SPT-100 [7]	I	II
CAMILA [8]	I	no data

Table 3.1: Conditions for instability in different regions of Hall thrusters.
Condition I: $\frac{1}{L_N} - \frac{2}{L_B} > 0$, $E > E_{thr}$. Condition II: $\frac{1}{L_N} - \frac{2}{L_B} < 0$, $E < E_{thr}$.

thruster channel [30].

It is interesting to note that despite the difference in design, all configurations here studied show that the instabilities are concentrated in the near anode and in the plume regions (as far as available data show) and that they are absent in the acceleration region of the thrusters, close to the maximum values of the electric and magnetic fields.

The primary driving source of the long wavelength instabilities here studied is the equilibrium electron current. The instability can be triggered by collisions, as considered in Ref. [13] or by gradients of plasma density, temperature and/or magnetic field. Various approximations lead to several different models. The result from the two-fluid model presented in this chapter differs in numerical factors from the model by Kapulkin, discussed in Ref. [9], because of their incomplete account of the electron compressibility. In Fig. 3.28, the growth rate of the instabilities derived by Kapulkin (Eq. 19 in Ref. [9]) is compared with the growth rate predicted by the two-field model. The growth rate for the anti-drift instability from Eq. (3.43) is also shown in the same figure. The growth rate predicted by the Kapulkin model is larger than the one predicted by the two-field model in the near anode region, but it is smaller in the plume region. The growth rate is significantly smaller without the gradients of the magnetic field as, as predicted by Eq. (3.43).

The real part of the frequency for various discharges is shown in Figs. 3.13, 3.14, 3.22, 3.23, 3.26 and 3.27. The mode phase velocity is typically in the same direction as $\mathbf{E} \times \mathbf{B}$ drift (which is negative in our notations) but it is not related to the $\mathbf{E} \times \mathbf{B}$ drift directly. Rather, it is determined by the inverse of the $\omega_n - \omega_D$ frequency (see Eq. (3.18)). As a result, the real part of the frequency scales inversely with the ion mass, $\omega_r \sim m_i^{-1}$ while the growth rate has an inverse dependence on the square root of the ion mass, $\gamma \sim (m_i)^{-1/2}$. The phase velocity of this mode is roughly one order

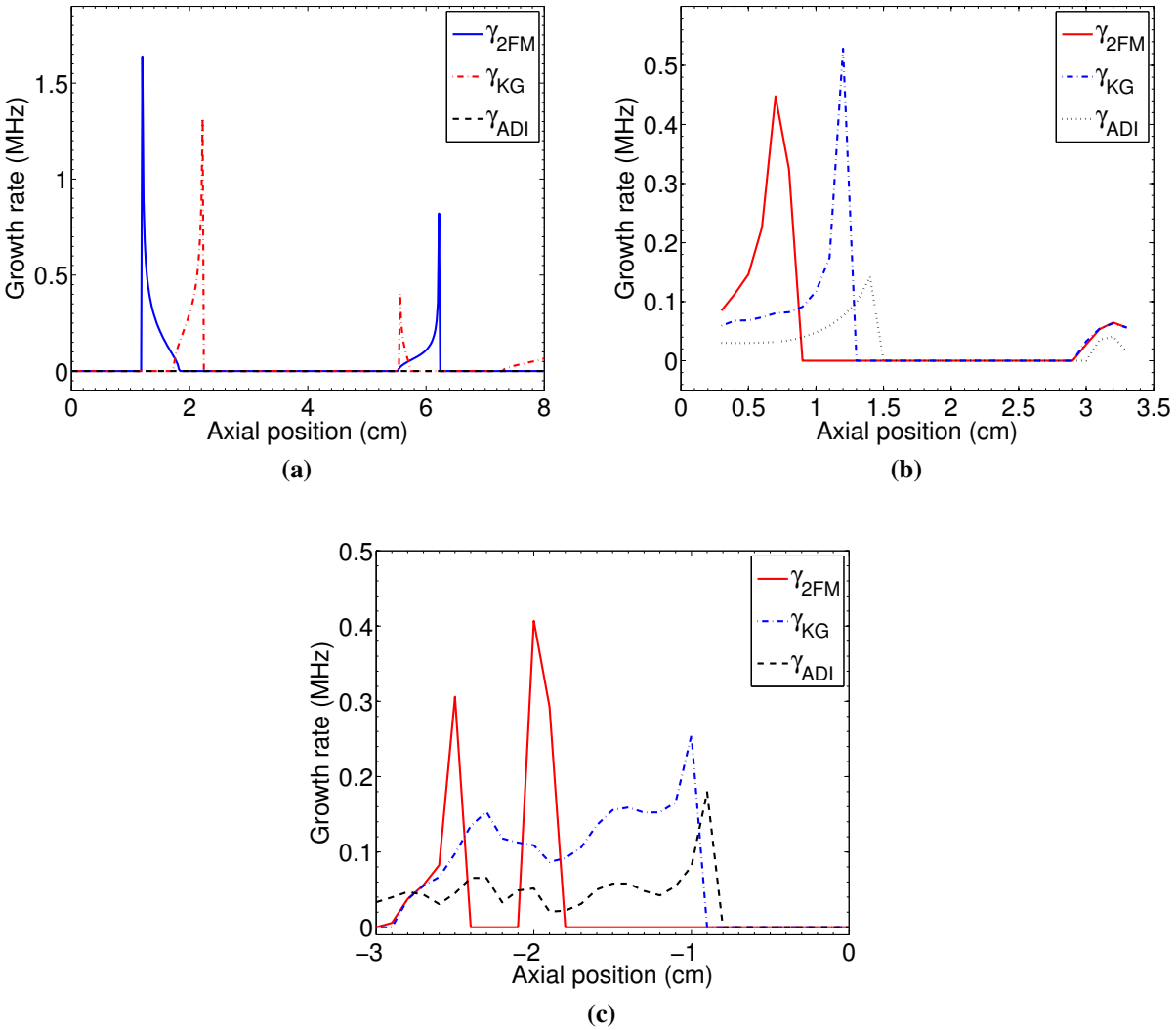

Figure 3.28: Growth rate of the instabilities for the a) HTX thruster, b) SPT-100 and c) CAMILA, as predicted by the two-field model, Eq. 19 from Ref. [9] and antidrift instability [10, 11].

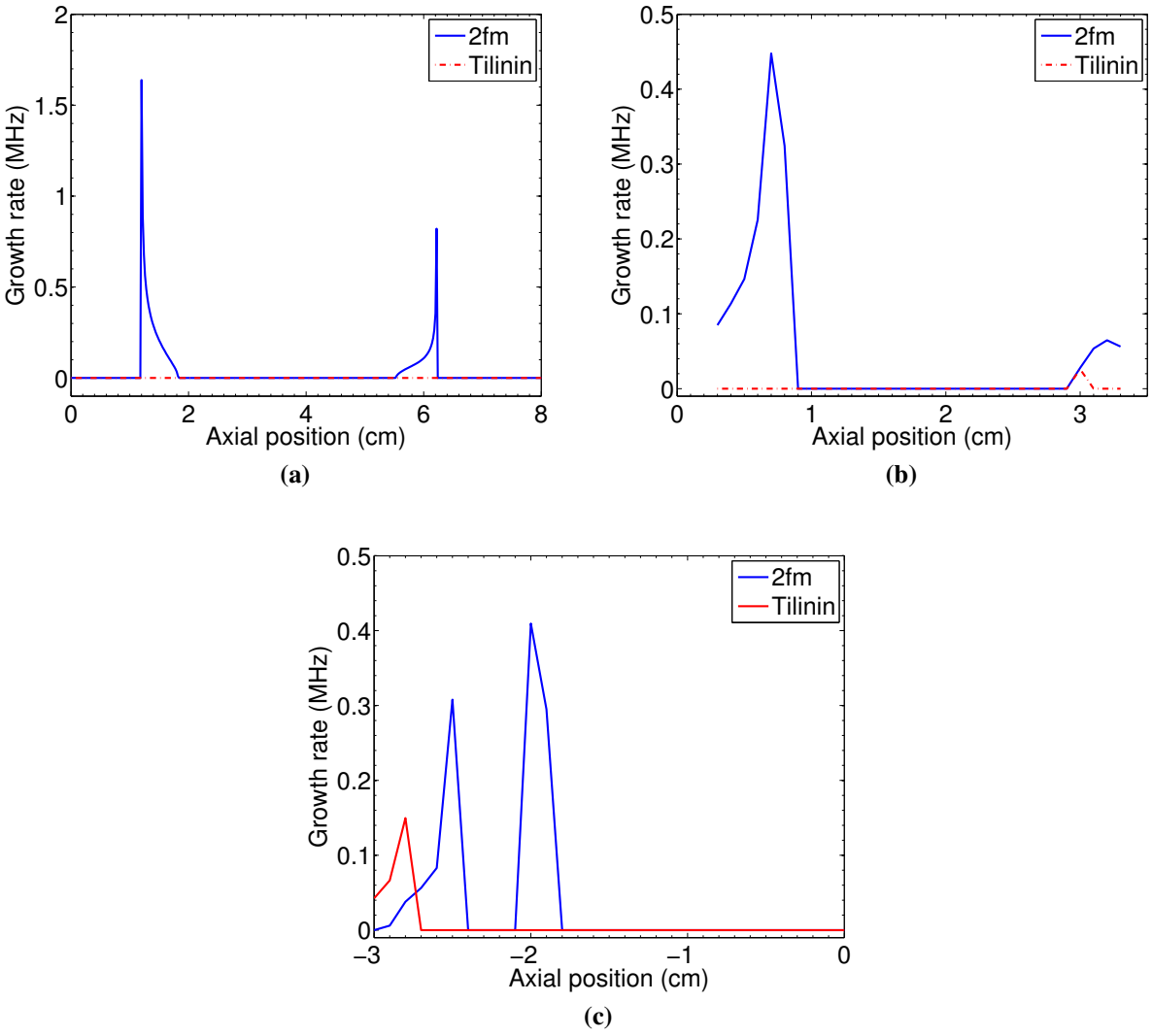

Figure 3.29: Growth rate of the instability as predicted by the two-field model and by Eq. (3.50) for a) HTX thruster, b) SPT-100 and c) CAMILA.

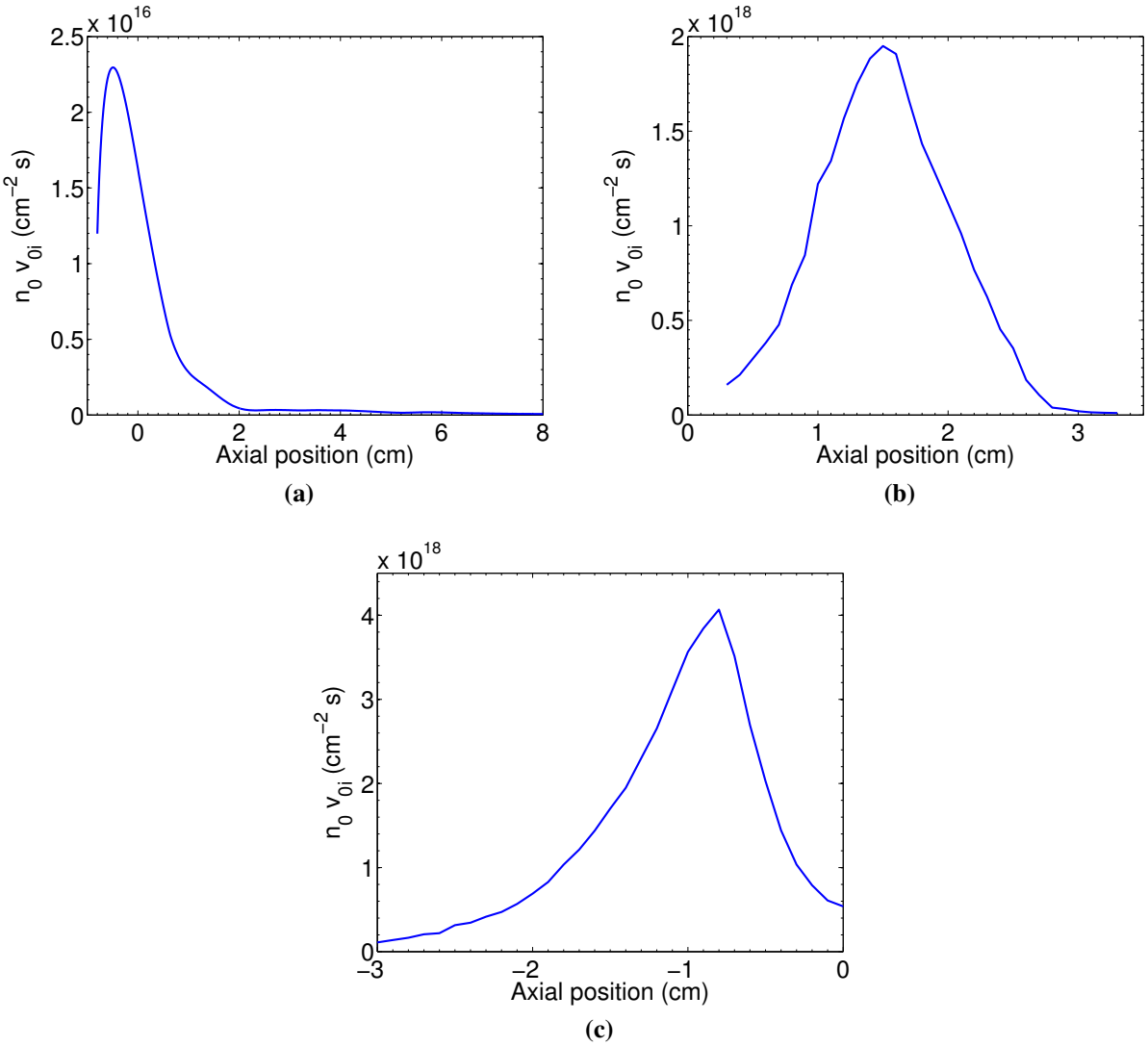

Figure 3.30: Product $n_0 v_{0i}$ for the a) HTX thruster, b) SPT-100 and c) CAMILA.

of magnitude lower than the $\mathbf{E} \times \mathbf{B}$ velocity (for the typical parameters under consideration). This result is consistent with the spoke phase velocity measured experimentally [30]. The inverse mass dependence also seems generally consistent with other experimental results [79]. This may suggest that the drift gradient modes are responsible for the spoke phenomena and no critical ionization phenomena may be involved. As was noted by Sakawa, the partial magnetization of ion motion results in the additional term $k_y v_{\theta i}$ to the real part of the frequency [10]. This is the regime of the so called modified Simon-Hoh instability. The calculation of the average ion drift velocity $v_{\theta i}$ in general requires a knowledge of the global electric field profile and it is not attempted here. An estimate based on Eq. (3.44) predicts that the $k_y v_{\theta i}$ contribution may be comparable or may exceed the real part of the frequency for the anti-drift mode in Eq. (3.18), thus changing the scaling for the real part of the mode frequency from $1/m_i$ for the anti-drift mode to $1/\sqrt{m_i}$ for the modified Simon-Hoh mode [10]. It is worth noting though that near the marginal stability boundary, the effect of the magnetic field gradient results in higher values of the real part of the frequency, so that the role of the ion azimuthal drift may be less pronounced.

Esipchuk and Tilinin have considered a physically similar model of the gradient drift instability but they used the relations (3.46) and (3.47) to express the density gradient via the electric field, resulting in Eq. (3.50). The solution of Eq. (3.50) is compared with the solution to the two-field model dispersion relation (Eq. 3.18) for the profiles in Figs. 3.11, 3.20 and 3.24 in Fig. 3.29. As can be seen from Fig. 3.29, there is a substantial difference between these models. Essentially, the model of (3.50) does not predict the instability in most of the regions. Should this model be used with the actual density profile, as in Eq. (3.51), the predictions will be similar to the Kapulkin model, with only quantitative differences with the two-fluid model as shown in Fig. 3.28.

As was noted above, the derivation of the dispersion relation (3.50) is based on the assumption that $n_0 v_{0i}$ remains constant. The data confirms that the assumption that $n(x)v_{0i}$ is constant is not met, especially near the channel exit, as can be seen from Fig. 3.30. Therefore, the model of Ref. [54], which is typically used in the form given by Eq. (3.50), gives significantly different results, due to the discrepancy of the ion density profile from the condition $n(x)v_{0i}$ = constant. The deviation of $n(x)v_{0i}$ from a constant value may be related to several factors, such as the radial divergence of the ion flow and to ionization processes. In addition to the modification of the equilibrium density profile, ionization process may lead to specific ionization instabilities [56],

which are not considered here.

Ducrocq *et. al.* [28] also studied the high frequency, short wavelength instability excited by the resonances between the term $k_y u_0$ and harmonics of the electron cyclotron frequency $n\omega_{ce}$. Such instabilities cannot be described by fluid theory presented in this chapter. According to Ref. [28], for the typical Hall thruster parameters, this instability is robust with respect to the gradients of plasma density and exists mainly in the exit plane of the Hall thruster, where the $\mathbf{E} \times \mathbf{B}$ drift velocity is maximal. This instability occurs as a result of coupling of the electron cyclotron mode and the ion sound and was studied in detail in Refs. [80–83]. These modes are typically highly aperiodic (with growth rates exceeding the real part of the frequency by orders of magnitude), which is consistent with some features observed experimentally [60]. Nonlinear theory and simulations [80–83] predict that due to large wave-vector, these modes saturate at low amplitudes and do not lead to significant anomalous transport.

The main emphasis in this chapter was on the analysis of azimuthal modes (with finite k_y). Note that according to (3.18), the drift gradient mode may also acquire the axial group velocity due the ion motion in axial direction. Such transit ion modes were studied in Refs. [29, 84], though the destabilization mechanisms considered in Refs. [29, 84] were due to collisions and ionization. The analysis presented in this chapter shows that drift gradient effects may also lead to the excitation of modes with ion group velocity in the axial direction.

The conditions for the linear excitation, the general mode characteristics such as frequency and growth rate, as well as the localization of the gradient drift modes studied here, are consistent with some experimental features, and thus may be responsible for anomalous electron mobility and nonlinear structures. The investigations of the latter require nonlinear theory and nonlinear simulations.

CHAPTER 4

WALL CURRENT CLOSURE EFFECTS ON PLASMA AND SHEATH FLUCTUATIONS IN HALL THRUSTERS

4.1 Introduction

The fluctuating closure current to the wall may destabilize the ion sound type modes in systems with $\mathbf{E}_0 \times \mathbf{B}_0$ electron drift [33]. The closure of the electron current parallel to the wall has strong influence on the steady state collisional electron transport. This phenomenon is well documented and it is known as Simon short circuit effect [85–87]. As it was shown in Ref. [33], the ion sound dynamics is strongly modified due to the current closure in the wall sheath leading to the instability. It is shown that this instability strongly depends on the dielectric properties of the wall material. How the sheath induced instability manifests itself for the specific conditions of the Hall thrusters is the subject of study of the present chapter.

4.2 Sheath boundary conditions and sheath induced instabilities

An important feedback mechanism in a finite length plasma arises when the sheath boundary conditions are included. The sheath boundary conditions determine the electron current to the walls, resulting in the coupling of the perturbed plasma density and potential to produce the instabilities. Consider a plasma between two walls separated by a distance of $2H$, where the equilibrium magnetic field $\mathbf{B}_0 = B_0\tilde{\mathbf{z}}$ is in the radial direction normal to the walls, the equilibrium electric field $\mathbf{E}_0 = E_0\hat{\mathbf{x}}$ is in the axial direction and the electrons drift along the azimuthal y direction with a

velocity $\mathbf{v}_0 = \mathbf{E}_0 \times \mathbf{B}_0 / B_0^2$ as in a Hall thruster (see Fig. 4.1). In the stationary state, the ion current to the sheath is equal to the Bohm current

$$J_{i0} = e n_0 c_s, \tag{4.1}$$

while the electron current is determined by electrons in the tail of the (Maxwellian) distribution function with energies above the potential drop in the sheath $\phi_0 = \phi_p - \phi_w$, where ϕ_p is the plasma potential at the plasma-sheath edge and ϕ_w is the wall potential

$$J_{0e} = -\frac{e n_0 v_{Te}}{2\sqrt{\pi}} \exp\left(-\frac{e(\phi_p - \phi_w)}{T_e}\right). \tag{4.2}$$

In stationary state, the total current into the sheath is zero i. e. $J_{0e} + J_{0i} = 0$. The perturbed ion and electron currents are determined by the density, potential and temperature perturbations from Eqs. (4.1)–(4.2) as

$$\tilde{J}_i = \left(\frac{\tilde{n}_i}{n_0} + \frac{1}{2}\frac{\tilde{T}_e}{T_{e0}}\right) J_{0i},, \tag{4.3}$$

$$\tilde{J}_e = \left[\frac{\tilde{n}_e}{n_0} + \frac{1}{2}\frac{\tilde{T}_e}{T_{e0}} - \left(\frac{e(\tilde{\phi}_p - \tilde{\phi}_w)}{T_e} - \Lambda\frac{\tilde{T}_e}{T_{e0}}\right)\right] J_{0e}, \tag{4.4}$$

where $\Lambda = \ln\sqrt{m_i/2\pi m_e}$. The parallel current to the sheath is the sum of the ion and electron currents from Eqs. (4.3)–(4.4). The total sheath current can then be expressed, neglecting temperature fluctuations, as [33]

$$\tilde{J}_{sh} = \frac{e^2 n_0 c_s}{T_e}\left(\widetilde{\phi}_p - \widetilde{\phi}_w\right). \tag{4.5}$$

If there is a conductive wall, $\tilde{\phi}_w = 0$, the sheath current is equivalent to a dissipation, the so called sheath resistivity [88–91]. In the case of a dielectric wall, one can assume that due to current conservation, the current at the plasma sheath edge is equal to the displacement current in the dielectric wall. Using the potential at the wall as a boundary condition and assuming that $k_z H >> 1$, where H is the half width of the channel, the potential at the wall can be written as function of the potential in the wall plasma [33]

$$\widetilde{\phi}_w = \widetilde{\phi}_p \frac{1}{1 - i\varepsilon\omega\left|k_y\right| c_s/\omega_{pi}^2}, \tag{4.6}$$

where ε is the dielectric constant of the wall material and ω_{pi} is the ion plasma frequency. Using Eqs. (4.5) and (4.6), the current into the sheath can be written as a function of the perturbations of

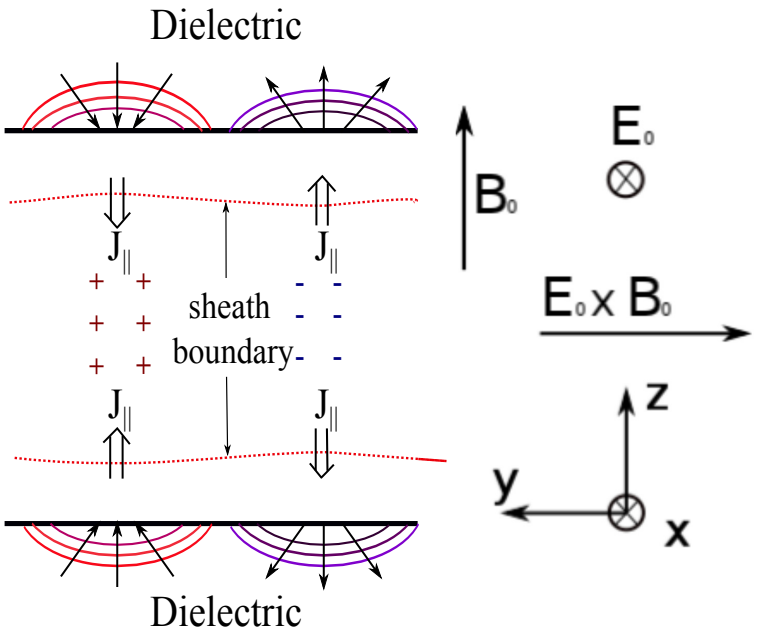

Figure 4.1: The schematics of the instability is driven by the component of the perturbed parallel current that is directed into the regions of positive charge (shown with "+"), thus enhancing the initial perturbation.

the plasma potential as

$$\tilde{J}_{sh} = -\frac{e^2 n_0 c_s}{T_e} \widetilde{\phi}_p \frac{iK}{1 - iK}, \tag{4.7}$$

where $K \equiv \varepsilon\omega \left|k_y\right| c_s/\omega_{pi}^2$. The value of the K parameter depends on the mode wave-vector k_y and the dielectric constant ε.

The expression for the sheath current that couples perturbed plasma density, potential and current can be used to derive dispersion relations for two types of modes. One of these modes is characterized by long wavelengths such that $H\partial/\partial z << 1$, while the other modes take into account the variations along the magnetic field. In both cases, the modes are rendered unstable due to the parallel component of the current that is directed into the regions of positive charge and enhances the initial perturbations as illustrated in Fig. 4.1.

To study the long wavelength global modes, consider a long plasma tube between the walls $z = -H$ and $z = H$ (see Fig. 4.1).

The electron and ion continuity equations, neglecting variations along the axial direction, can

be written as

$$\frac{\partial \tilde{n}_e}{\partial t} + u_0 \frac{\partial \tilde{n}_e}{\partial y} - \frac{1}{e}\frac{\partial \tilde{J}_{||e}}{\partial z} = 0, \tag{4.8}$$

$$\frac{\partial \tilde{n}_i}{\partial t} - i\frac{en_0}{m_i\omega}\frac{\partial^2 \tilde{\phi}}{\partial y^2} + \frac{1}{e}\frac{\partial \tilde{J}_{||i}}{\partial z} = 0. \tag{4.9}$$

The average density and potential are introduced as

$$\overline{n} \equiv \frac{1}{2H}\int_{-H}^{H} \tilde{n} dz, \tag{4.10}$$

$$\overline{\phi} \equiv \frac{1}{2H}\int_{-H}^{H} \widetilde{\phi} dz, \tag{4.11}$$

and the ion and electron continuity equations can be averaged, assuming an odd parity for the parallel currents ($J_{||}(-H) = -J_{||}(H)$), to produce

$$-i(\omega - \omega_0)\overline{n} - \frac{J_{\|e}(H)}{eH} = 0, \tag{4.12}$$

$$-i\omega\overline{n} + ien_0\frac{k_y^2\overline{\phi}}{\omega m_i} + \frac{J_{\|i}(H)}{eH} = 0, \tag{4.13}$$

where the $J_{\|e}(H)$ and $J_{\|i}(H)$ are the electron and ion currents at the sheath boundary, given by Eqs. (4.3)–(4.4),

$$J_{||i}(H) = \frac{n(H)}{n_0}J_{0i}, \tag{4.14}$$

$$J_{||e}(H) = \frac{n(H)}{n_0}J_{0e} + \frac{iK}{1-iK}\frac{e}{T_e}\phi(H)J_{0e}. \tag{4.15}$$

From Eqs. (4.10)–(4.15), it can be seen that the electron current exhibits a Doppler shift while the ion current does not. Introducing the sheath collision frequency, $\nu_{sh} = c_s/H$, and using the expressions obtained for the currents above, the perturbed average ion and electron densities are given by [33]

$$\frac{\overline{n}_i}{n_0} = \frac{k_y^2 c_s^2}{\omega(\omega + i\nu_{sh})}\frac{e\overline{\phi}}{T_e}, \tag{4.16}$$

$$\frac{\overline{n}_e}{n_0} = \frac{\nu_{sh}K}{(1-iK)(\omega - \omega_0 + i\nu_{sh})}\frac{e\overline{\phi}}{T_e}, \tag{4.17}$$

Using quasineutrality and assuming that $K < 1$ (dielectric), the following dispersion relation is obtained [33]

$$\omega^2(\omega + i\nu_{sh}) = \frac{|k_y| c_s \omega_{pi}^2}{\varepsilon\nu_{sh}}(\omega - \omega_0 + i\nu_{sh}). \tag{4.18}$$

The mode described by Eq. (4.18) has an unstable root for $\omega < \omega_0$, given by

$$\omega_r \simeq \gamma \simeq \left(-\frac{\omega_0 |k_y| c_s \omega_{pi}^2}{\varepsilon \nu_{sh}} \right)^{1/3}, \tag{4.19}$$

which corresponds to a reactive instability of the negative energy mode. In the opposite limit, $K >> 1$, the instability becomes dissipative with a corresponding complex frequency of

$$\omega = \pm \left(i \frac{\omega_0 k_y^2 c_s^2}{\nu_{sh}} \right)^{1/2}. \tag{4.20}$$

The transition between two limits, $K < 1$ and $K > 1$, is controlled by the mode frequency and the value of the dielectric constant ε. The limit of an infinitely conducting wall is obtained in the formal limit of $\varepsilon \to \infty$.

In the analysis presented in this chapter the ion convection along the channel is neglected. The effect of the ion convection is manifest in the inclusion of the term $k_x V_{0i}$, where k_x is the wavevector in the axial direction and $V_{0i} = \sqrt{2e\phi/m_i}$ is the equilibrium ion velocity due to the electric field. When this term is included, the dispersion relation for the long wavelength (global) modes, given by Eq. (4.18) becomes

$$\omega(\omega - k_x V_{0i}) \left(\omega - k_x V_{0i} + i\nu_{sh} \right) = \frac{|k_y| \, c_s \omega_{pi}^2}{\varepsilon \nu_{sh}} \left(\omega - \omega_0 + i\nu_{sh} \right). \tag{4.21}$$

For the Hall thruster parameters under consideration in this chapter, the maximum ion equilibrium velocity is of the order of 10^4 m/s, which results in the ion convection frequency $k_x V_{0i}$ of around 10^4 rad/s at most. Since the frequencies calculated for both the local and global modes are both much larger than $k_x V_{0i}$, it is expected that theses modes will not be severely affected by the ion convection term and they can be safely ignored.

The local modes are obtained when the variations along the magnetic field are taken into account. The eigenmodes obtained in this case have a dependence on both the z (parallel to the magnetic field) and y (perpendicular to the magnetic field) coordinates. In general, these perturbations can be expressed as the sum of a mode with both z and y dependence and a boundary mode that depends only on y

$$\phi = \left[\phi_0 \cos(k_z z) + \phi_b \right] e^{i(k_y y - \omega t)}, \tag{4.22}$$

$$n = \frac{e n_0}{T_e} \left[\phi_0 \cos(k_z z) + \phi_b \frac{k_y^2 c_s^2}{\omega^2} \right] e^{i(k_y y - \omega t)}. \tag{4.23}$$

Here, ω is the ion sound frequency, k_y is a free parameter determined from the geometry and boundary conditions of the region of interest and k_z is an eigenvalue that is calculated from the solvability condition of the linear system obtained from the ion and electron continuity and momentum conservation equations.

Coupling to the sheath follows from the averaged electron and ion equations (4.12)–(4.13), where now the average potential and density over the region from $z = -H$ to $z = H$ can be calculated using Eqs. (4.22)–(4.23) to produce

$$\overline{\phi} = \left[\phi_0 \frac{\sin(k_z H)}{k_z H} + \phi_b\right] \exp\left(-i\omega t + i k_y y\right), \tag{4.24}$$

$$\overline{n} = \frac{e n_0}{T_e}\left[\phi_0 \frac{\sin(k_z H)}{k_z H} + \phi_b \frac{k_y^2 c_s^2}{\omega^2}\right] \exp\left(-i\omega t + i k_y y\right). \tag{4.25}$$

Replacing the values for the currents in Eqs. (4.14)–(4.15) and the averaged density and potential from Eqs. (4.24)–(4.25) in the electron continuity equation (4.12), one obtains

$$\begin{aligned} & \phi_b\left(-i(\omega-\omega_0)\frac{k_y^2 c_s^2}{\omega^2} + \nu_{sh}\frac{k_y^2 c_s^2}{\omega^2} + \nu_{sh}\frac{iK}{1-iK}\right) \\ + \quad & \phi_0\left(-i(\omega-\omega_0)\frac{\sin k_z H}{k_z H} + \frac{\nu_{sh}\cos k_z H}{1-iK}\right) = 0. \end{aligned} \tag{4.26}$$

Using quasineutrality, the ion continuity equation (4.13) can be written as

$$i\omega_0 \overline{n} + i\frac{e n_0}{\omega m_i} k_y^2 \overline{\phi} + \frac{1}{eH}\frac{iK}{1-iK}\frac{e}{T_e}\phi(H) J_{0e} = 0,$$

or

$$\begin{aligned} & \phi_0\left(i\omega_0 \frac{\sin k_z H}{k_z H} - i\frac{k_y^2 c_s^2}{\omega}\frac{\sin k_z H}{k_z H} + \frac{iK\nu_{sh}\cos k_z H}{1-iK}\right) + \\ & \phi_b\left(-i(\omega-\omega_0)\frac{k_y^2 c_s^2}{\omega^2} + \nu_{sh}\frac{iK}{1-iK}\right) = 0. \end{aligned} \tag{4.27}$$

From Eqs. (4.26)–(4.27), a 2×2 linear system for ϕ_b and $\phi_0\cos(k_z H)$ is obtained. The solvability condition for this system of equations yields the dispersion relation for the small scale (local) modes [33]

$$\begin{aligned} & \frac{\tan(k_z H)}{k_z H} \times \left[\omega_0 - \frac{k_y^2 c_s^2}{\omega} - \frac{i\omega(\omega-\omega_0)}{\nu_{sh}}\left(1 - \frac{k_y^2 c_s^2}{\omega^2}\right)\right. \\ & \left. + i\omega\left(\frac{\omega^2}{k_y^2 c_s^2} - 1\right)\frac{K}{1-iK}\right] \\ & + \left[\omega - \omega_0 + \frac{\nu_{sh}}{1-iK} - \nu_{sh}\frac{\omega^2}{k_y^2 c_s^2}\frac{K}{1-iK}\right] = 0. \end{aligned} \tag{4.28}$$

The eigenvalues for ω can be obtained by solving Eq. (4.28) together with the dispersion relation for the ion sound waves, $\omega^2 = (k_y^2 + k_z^2)$. The local and global modes dispersion relation have been studied in detail in Ref. [33]. The dispersion relations predict perturbations which have azimuthal phase velocity in the direction of the electron $\mathbf{E}_0 \times \mathbf{B}_0$ drift. The growth rate and absolute value of the frequency of the unstable modes grow with the height of the channel, and the electron drift velocity ω_0. The growth rate also exhibits a $1/\sqrt{m_i}$ dependence. The absolute value of the real part of the frequency and the growth rate tend to decrease with increasing dielectric permittivity but they do not completely disappear in the limit $\varepsilon \to \infty$ which would correspond to the case of a fully conducting wall with $\phi_w = 0$.

4.3 Sheath induced modes in Hall thruster

The instabilities studied in the previous section can be thought of as resulting from a positive feedback mechanism between the Doppler shifted parallel electron current and fluctuations of plasma density and potential. In this section how these instabilities may manifest themselves for specific conditions of the Hall thruster is investigated. As an example, generic parameters from the 1 kW Laboratory Hall thruster developed at the PPPL Hall Thruster Experimental facility [12, 92] are used. This thruster has a channel made of boron nitride ceramic (BN) and has length of 90 mm (from anode to channel exit) and a mean radius of 36 mm [92]. For this study measured plasma parameters for the acceleration and exit region of the thruster as reported in Ref. [12] are used.

The growth rate and frequency obtained from Eqs. (4.18) and (4.28) using the plasma parameters corresponding to the 1 kW Laboratory Hall thruster are shown in Fig. 4.2. The instabilities are present in the region that extends from 8 mm upstream from the channel exit to the exit of the channel. The growth rate and the real part of the frequency of the instabilities predicted by the global modes in Eq. (4.18) reach a maximum value of f=2.88 MHz and γ=3.53 MHz 2 mm upstream from the channel exit. The growth rate and the real part of the frequency of the instabilities predicted by the local modes in Eq. (4.28) reach a maximum value of f=2.88 MHz and γ=3.53 MHz, also 2 mm upstream from the exit of the thruster channel. It turns out that for these parameters, the growth rate and frequency for the global and local modes are almost identical. These calculated frequencies are of the same order of magnitude as the azimuthal modes experimentally

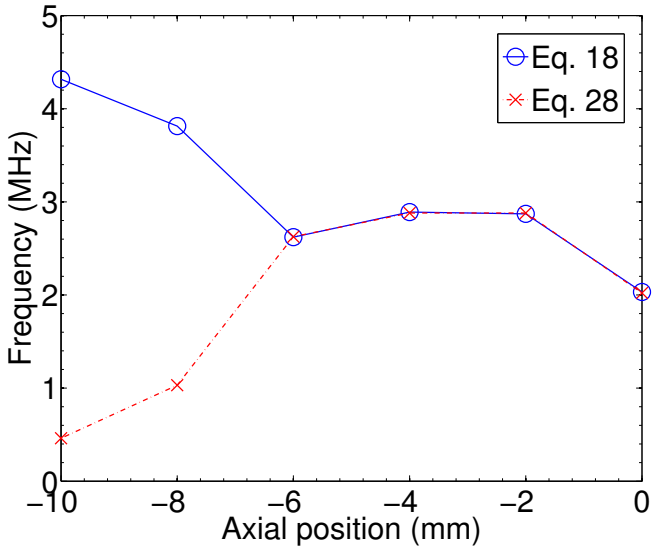

(a)

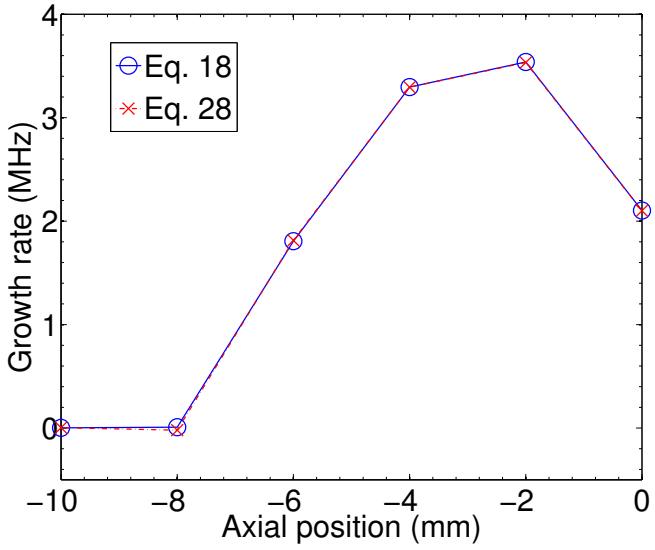

(b)

Figure 4.2: Frequency and growth rate of the instabilities in the 1 kW Laboratory Hall thruster [12] as a function of axial position from the channel exit as predicted by Eqs. (4.18) and (4.28); $k_y = 28$ rad/m (m=1). The anode is located at x = -36 mm.The exit plane is at x=0.

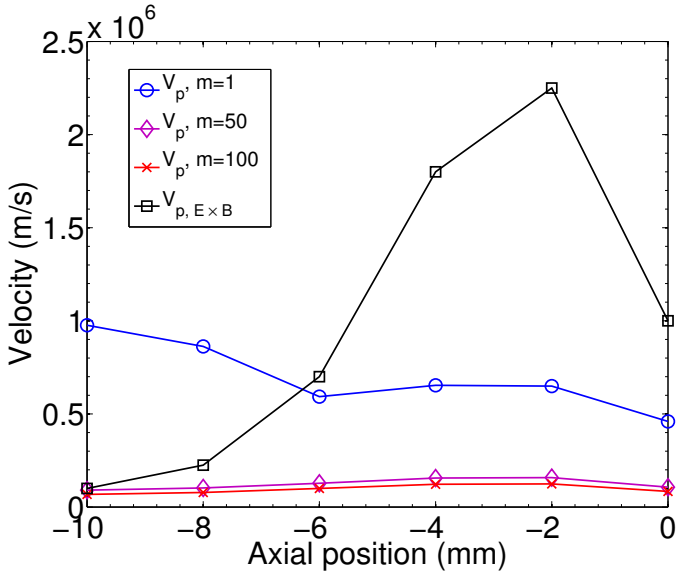

Figure 4.3: Azimuthal phase velocities of the instabilities in the 1 kW Laboratory Hall thruster [12] as a function of axial position from the channel exit as predicted by Eqs. (4.18) and (4.28)for different mode numbers and the equilibrium $\mathbf{E}_0 \times \mathbf{B}_0$ electron drift velocity, $k_y = m/r$, $r = 3.6$ cm. The anode is located at x = -36 mm. The exit plane is at x=0.

observed by Litvak *et. al* [12]. The calculated azimuthal phase velocity of the instabilities for the lowest azimuthal mode number (m=1) is shown in Fig. 4.3. The azimuthal phase velocity for the global modes reaches a maximum value of 6.52×10^5 m/s at 2 mm upstream from the channel exit. The maximum value for the azimuthal phase velocity of the local modes is reached at 2 mm upstream from the channel exit and has a value of 6.52×10^5 m/s. The equilibrium $\mathbf{E}_0 \times \mathbf{B}_0$ electron drift velocity has a maximum value of 2.25×10^6 m/s also at 2 mm upstream from the channel exit. Thus the phase velocities of both local and global modes are below the equilibrium electron drift velocity, meaning that the instability is of the negative energy type. The phase velocity of the unstable modes reported by Litvak *et. al* has a maximum value of the order of 1.75×10^6 m/s also at 2 mm upstream from the channel exit. The instability reported in the current Chapter is also characterized by having a real part of the frequency that decreases with increasing magnetic field and increases with increasing electric field as can be seen in Fig. 4.4. These results in general agree with the results obtained by Litvak *et. al,* as can be compared with Fig. 7 from Ref. [12].

Another thruster configuration of interest is the SPT-100 Hall thruster. The SPT-100 thruster has dielectric walls made of Borosil ($BNSiO_2$) with a dielectric constant, ε, of 3.50-3.75. The chan-

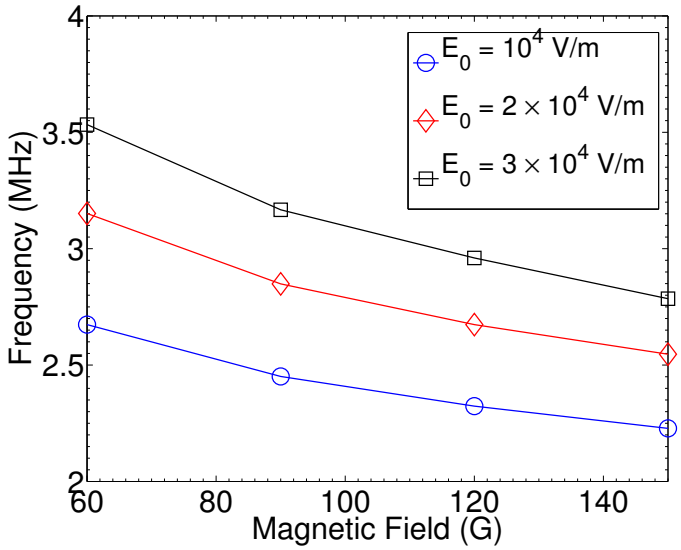

(a)

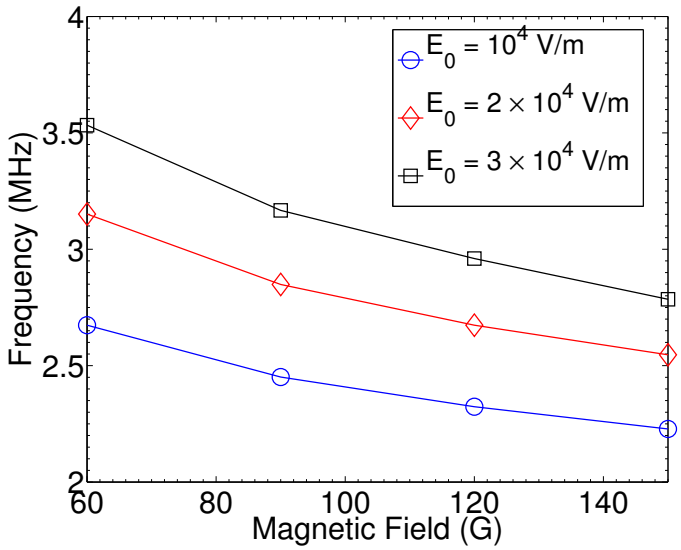

(b)

Figure 4.4: Frequency of the modes predicted by Eqs. (4.18) (a) and (4.28) (b) as a function of the magnetic field for different values of the electric field in 1 kW Laboratory Hall thruster [12]. $k_y = 28$ rad/m (m=1).

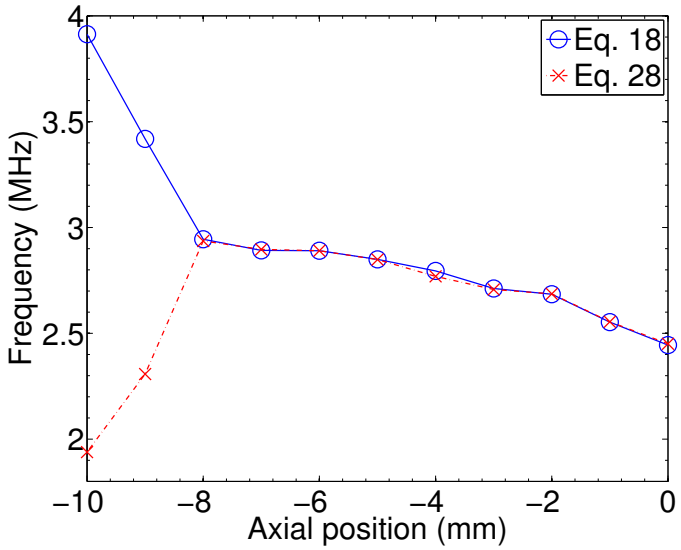

(a)

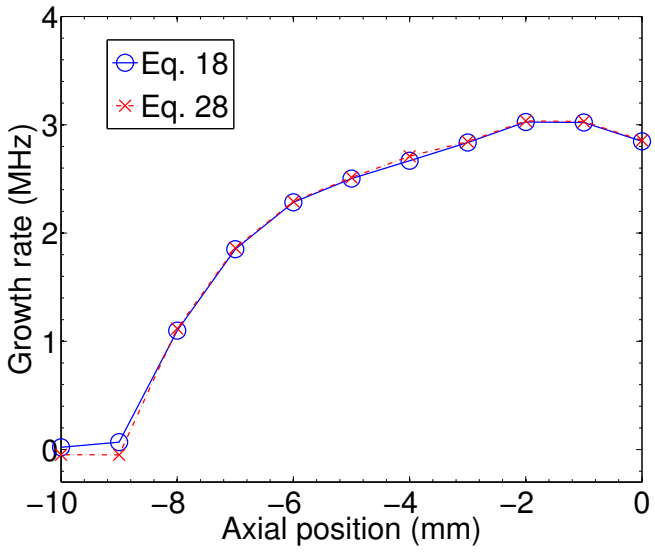

(b)

Figure 4.5: Frequency and growth rate of the instabilities in a SPT-100 thruster [7] as a function of axial position from the channel exit as predicted by Eqs. (4.18) and (4.28); $k_y =$ 20 rad/m (m=1). The exit plane is at x=0.

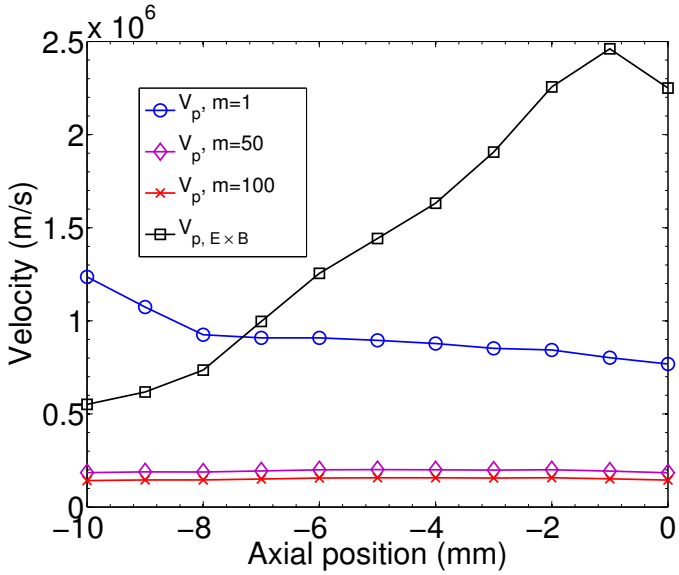

Figure 4.6: Azimuthal phase velocities of the instabilities in a SPT-100 thruster [7] as a function of axial position from the channel exit as predicted by Eqs. (4.18) and (4.28) for different mode numbers and the equilibrium $\mathbf{E}_0 \times \mathbf{B}_0$ electron drift velocity, $k_y = m/r$, $r = 5$ cm. The exit plane is at x=0.

nel width is 0.75 cm and the mid radius of the thruster is 5 cm [7]. The growth rates and frequency obtained from Eqs. (4.18) and (4.28) using the plasma parameters in the discharge chamber the of SPT-100 Hall thruster obtained by Hoffer with the HPHall-2 code [74, 75] as reported in Ref. [7] are shown in Fig. 4.5. For these conditions, the instabilities are present in the region located 9 mm upstream from the channel exit for the local modes. The global modes predict instability for the channel region but the growth rate is small reaching a value of 1 MHz at around 8 mm upstream from the channel exit and a maximum value of 3.03 MHz 2 mm upstream from the exit plane. The real part of the frequency of the instabilities predicted by the global modes Eq. (4.18) reaches a value of 2.554 MHz at the exit of the channel while the frequency for the local modes reaches a value of 2.5 MHz at the channel exit. These values correspond to azimuthal phase velocities at the exit plane of 8.03×10^5 m/s for the both the global and local modes. Similarly to the case with the 1 kW Laboratory Hall Thruster, the real part of the frequency and the growth rates for the local and global modes are equal. At the exit plane, the equilibrium $\mathbf{E}_0 \times \mathbf{B}_0$ azimuthal velocity is 2.40×10^6 m/s, which means that the instabilities are of the negative energy type.

These results for the SPT–100 parameters are similar to high frequency instabilities reported

by Lazurenko *et. al* [21]. Lazurenko *et. al* studied high frequency instabilities in the 1.5 kW SPT-100ML and 5 kW PPS-X000ML Hall thrusters. They observed a high frequency mode in the region directly downstream from the peak of the magnetic field inside the channel and in the near exit region that propagates azimuthally with a phase velocity of 2.0$\times$ 10^6 m/s, which corresponds to a frequency of 7-9 MHz for the lowest azimuthal mode [21]. This velocity is close to the expected electron equilibrium $\mathbf{E}_0 \times \mathbf{B}_0$ velocity. The real part of the frequency of the instabilities reported by Lazurenko et. al increases with increasing discharge voltage (see Fig. 10 in Ref. [21]). Also, a decrease of the frequency with increasing magnetic field in the PPS-X000ML Hall thruster is reported [21], similar to the trend observed in the experiments from Ref. [12].

As noted above, in the channel exit region the real part of the frequency and the growth rate of the instabilities predicted by both global and local dispersion relations are almost identical. The frequency of the local modes, ω, and eigen-value wavenumber in the direction parallel to the magnetic field, k_z, are calculated using the ion sound frequency and (4.28). For the frequencies predicted by the local modes in the channel exit region, the obtained wavenumber parallel to the magnetic field results in the small value of the factor $\tan(k_z H)/k_z H \ll 1$. Taking this into account, the equation for the local modes in the region close to the channel exit can be written as

$$k_y^2 c_s^2 (\omega - \omega_0) = \omega^2 \frac{\nu_{sh} K}{1 - iK}. \tag{4.29}$$

In the exit region $K << 1$ and the sheath collision frequency ν_{sh} is much smaller than both the frequency of the instabilities and the electron drift frequency, which allows to write the equation for the local modes in this region as

$$\omega^3 = \frac{|k_y|\, c_s \omega_{pi}^2}{\varepsilon \nu_{sh}} \left(\omega - \omega_0\right), \tag{4.30}$$

which is the same as the dispersion relation for the global modes, Eq. (4.18), under the assumption that $\nu_{sh} << \omega, \omega_0$. Another result obtained from the solution to the eigenvalue problem for k_z is that in Eqs. (4.22)–(4.23) for the potential and density perturbations, $\phi_b >> \phi_0$, which means that the potential and density perturbations are mainly boundary modes that depend on the azimuthal coordinate similar to the global modes.

It is possible to estimate the magnitude of the axial current produced by these fluctuations using quasilinear estimates. The perturbations of the azimuthal electric field produce the axial drift

velocity

$$\tilde{v}_{ex} = \frac{\tilde{E}_y}{B_0}. \tag{4.31}$$

This perturbed electron drift results in the axial electron current, whose time average can be calculated at each point along the channel as

$$\left\langle \tilde{J}_{ex} \right\rangle = \frac{1}{2}\mathrm{Re}\left(e\tilde{n}_e\tilde{v}^*_{ex}\right). \tag{4.32}$$

Using the expression in Eq. (4.16) for the perturbed plasma density, assuming quasineutrality, and with the azimuthal electric field given by the potential perturbations $\tilde{E}_y = -ik_y\phi$, the averaged axial electron current is calculated as

$$\left\langle \tilde{J}_{ex} \right\rangle = \frac{e^2 n_0 k_y^3 c_s^2}{2B_0 T_e} \frac{|\phi|^2}{|\omega|^2|\omega + i\nu_{sh}|^2}\omega_r(2\gamma + \nu_{sh}). \tag{4.33}$$

This estimate can be written in the form

$$\left\langle \tilde{J}_{ex} \right\rangle \simeq \frac{n_0 T_e k_y^3 c_s^2}{B_0} \frac{e^2|\phi|^2}{T_e^2|\omega|^2}, \tag{4.34}$$

assuming $|\omega| \simeq \omega_r \simeq \gamma$. For (purely) sound waves with $\omega \simeq k_y c_s$, and $e\left|\phi\right|/T_e \simeq 1$, this estimate would lead to the Bohm like current $\left\langle \tilde{J}_{ex} \right\rangle \sim n_0 T_e k_y/B_0$, $k_y = m/r$, where m is the azimuthal wave number and r is the radius. Note that potential fluctuations of the order of $|\phi|$=10 V were observed in experiments [21, 93] for the exit region.

However, for the boundary modes considered here, the equation (4.34) predicts much lower amplitude of the axial current because the amplitude of the density fluctuations, that is proportional to the ratio $k_y^2 c_s^2/\omega^2$, see Eq. (4.16), is small for the modes under consideration. Suppression of the amplitude of the density response (with respect to the amplitude of potential fluctuations) occurs as a result of the current constrain at the sheath, Eqs. (4.14) and (4.15). It is important to note that the sheath response depends on the dielectric constant of the wall material. In the limit of high ε, the mode frequency and growth rate decrease [33]. In this regime, using (4.20) the axial current estimate in Eq. (4.34) takes the form

$$\left\langle \tilde{J}_{ex} \right\rangle \simeq n_0 T_e k_y/B_0 \left(\nu_{sh}/\omega_0\right)\left(e\left|\phi\right|/T_e\right)^2. \tag{4.35}$$

Numerically, for typical thruster parameters, $|\phi| \simeq 10$ V, azimuthal wavenumber m =100, and permittivity ε =100, the axial current calculated with Eq. (4.34), is of the order of 10^2 A/m^2, which

is consistent with typical experimental values. The current amplitude decreases with an increase of the magnetic field (downstream towards the exit). The current decrease with the magnetic field is weaker than B_0^{-1}. Note that in the $\varepsilon \to \infty$ limit, the magnetic field dependence formally disappears in Eq. (4.35). The self-consistent evaluation of the anomalous current requires a nonlinear theory to determine the amplitude of the fluctuations as well as the effective wave number.

4.4 Summary

The stationary $\mathbf{E}_0 \times \mathbf{B}_0$ flow of magnetized electrons is a powerful source of free energy in plasmas with unmagnetized ions. There is a variety of bulk plasma modes that are driven unstable due to gradients of magnetic field, plasma density, collisional and ionization effects [9, 11, 13, 28, 29, 54, 94, 95] and that may be sources of turbulent transport. Near-wall collisions are also considered as a possible contribution to anomalous current [17, 93]. Additionally, it was earlier noted that the wall material affects the electron transport [96]. In this chapter the positive feedback mechanism between the plasma current into the sheath and potential fluctuations in the bulk plasma is analyzed. This mechanism, resulting in bulk plasma and sheath fluctuations, is sensitive to the dielectric properties of the wall material.

The instabilities discussed in the present chapter are located in the region around the peak of the magnetic field. They have a real part of the frequency in the 1-10 MHz range, which results in an azimuthal phase velocity of the order of 6.52$\times$ 10^5 - 8.03$\times$ 10^5 m/s for the lowest azimuthal wavenumber m =1. This phase velocity is lower than, but of the same order of magnitude as the equilibrium $\mathbf{E}_0 \times \mathbf{B}_0$ electron drift velocity. Similar propagation characteristics have been observed experimentally by Litvak *et. al* [12] and Lazurenko *et. al* [21] for different types of Hall thrusters.

The real part of the frequency of both the global and local modes in Eqs. (4.18)–(4.28) decreases with increasing magnetic field and increases with increasing electric field, similar to what was observed in experiments by Litvak *et. al* and Lazurenko *et. al*, as can be seen in Fig. 4.4. This is also consistent with the observation that the maximum values of both the real part of the frequency and the growth rate correspond to the region of the maximum of the equilibrium $\mathbf{E}_0 \times \mathbf{B}_0$ velocity.

It is worth to note that the characteristic phase velocity of the modes studied in our work is

weakly sensitive to the mode number, as shown in Figs. 4.3 and 4.6. For higher mode numbers, the mode frequency increases, while the phase velocity decreases. In these regimes, the kinetic electron cyclotron effects need to be included, which is outside the scope of this dissertation. Tsikata *et. al* have observed fluctuations in the 5 kW PPS-X000ML Hall thruster that are located outside of the peak of the magnetic field and have the real part of the frequency of around 4.5 MHz and the wavelengths of the order of the electron cyclotron radius [60, 61]. These instabilities are characterized by a phase velocity much smaller than the $\mathbf{E}_0 \times \mathbf{B}_0$ equilibrium drift velocity and have an origin in the resonance of the electron cyclotron frequency with the azimuthal electron drift frequency ω_0 [28, 60, 61].

Wall material effects manifest themselves via the dielectric permittivity of the wall. The walls of the Hall thrusters studied are made of Boron Nitrate (1 kW PPPL Laboratory Hall Thruster) and Borosil, $BNSiO_3$, (SPT-100), whose permittivity can increase with temperature. The thruster walls can reach temperatures of the order of 500^oC, which may result in a permittivity as high as 50. In the present discussion purely dielectric wall materials (real ε) are considered. The more general case of finite conductivity (complex permittivity ε) is not studied here, though the case of ideally conducting wall can be reproduced in the limit $\varepsilon \to \infty$. The results presented in this chapter indicate that the dielectric properties of the wall material act as an additional parameter that may affect the electron transport and thruster performance and thus are complementary to the secondary electron emission (SEE) effects which are also important for the electron transport in the thruster [96]. It is interesting to note that the possible influence of the dielectric properties of the wall material on the thruster performance was noted in Ref. [97]. In that paper, the effect of the dielectric properties of the wall material was considered with the example of ion sound waves neglecting electron inertia, finite Larmor radius and plasma gradients. The latter effects were shown to be important for the conditions of the Hall thruster and the related instabilities were studied in connection with the problem of anomalous transport [9, 11, 28, 54, 94]. It is expected that wall properties will also be important for such modes.

CHAPTER 5

NONLINEAR SIMULATIONS AND ANOMALOUS ELECTRON TRANSPORT IN HALL THRUSTER PLASMA

5.1 Introduction

It is well established experimentally that in the acceleration and near plume regions of a Hall thruster, the classical resistivity (mobility) is not sufficient to explain experimental results. Fluctuations driven by various instabilities are thought to be the main mechanism responsible for the anomalous transport observed in Hall thrusters.

The full picture of the instabilities in Hall plasmas is complex and, for typical experimental conditions, likely involves a number of interacting modes which require numerical simulations. Particle-in-cell kinetic simulations offer a first principles description that has provided valuable results on plasma dynamics [31, 98–101]. Such fully kinetic nonlinear simulations could be the most realistic approach to study the experimental conditions, however, they could also be difficult to interpret. These simulations are still very difficult and expensive even with modern computer capabilities. Hybrid simulations, where electrons are treated as fluid and ions are treated as particles, have also been used to study the plasma behavior in a Hall thruster, but similar to the particle approach, they are computationally very expensive [18, 29, 35, 102–105]. In these hybrid simulations, either full Bohm mobility [35], or an ad-hoc combination of both fluctuation-induced mobility and near wall conductivity [103, 104] have been artificially added. On the other hand, fluid simulations are faster and cheaper numerical tools for simulations of nonlinear plasma dynamics. They are easier to interpret and provide much greater flexibility in separating various physics elements. Fluid models have been important contributors and have been indispensable for the development of tokamak physics [106]. Fluid models are especially valuable in complex magnetic geometries

where direct kinetic simulations may become prohibitively expensive [107]. The simulations presented in this chapter are based on an advanced multi-fluid model developed to investigate the turbulent fluctuations and transport in Hall plasmas relevant to electric propulsion. These fluid simulations are based on the BOUT++ computational framework [40]. BOUT++ is a platform for fluid and plasma simulations in curvilinear magnetic field geometry using finite-difference discretization and a variety of numerical methods and time-integration solvers. It was designed and tested with reduced plasma fluid models applications in mind by LLNL, University of York (UK) and others. It has been widely used for studies of edge tokamak phenomena, 3D plasma structures and plasma turbulence and structures in Large Plasma Device (LAPD) [41, 42, 108–110]. As mentioned above, BOUT++ has now been recently adapted for simulations of Hall plasmas relevant to electric propulsion [111].

The fluid model discussed in this chapter is based on the low frequency ($\omega < \omega_{ce}$) reduction of the electron dynamics. It includes the electron inertia and electron neutral collisions, so that the lower hybrid modes destabilized by $\mathbf{E} \times \mathbf{B}$ drift and collisions are included in addition to the long wavelength modes. This nonlinear model also includes the electron gyroviscosity and the so called gyroviscous cancellation effects [112]. The gyroviscosity effects are of the same order as the electron inertia and have to be retained in a finite electron temperature plasma to properly account for the correct behavior at high values of the perpendicular wave-vector, as well as for the proper energy balance among nonlinear terms. Note that both growth rate and real part of the density gradient driven modes increase linearly with the wave-vector $\mathbf{k}$. The inertia and gyroviscosity effects introduce a physics based cutoff at high $\mathbf{k}$ values, which is important for simulations in finite size regions.

5.2 Nonlinear equations for Hall thruster plasma

Here the set of basic fluid equations appropriate for studying the plasma dynamics in the conditions typical of a Hall thruster is formulated. In the region inside the Hall thruster channel, there is a background magnetic field that is mainly directed in the radial direction, $\mathbf{B}_0 = B_0\hat{\mathbf{y}}$ [1]. The

[1]The reader is brought to the attention that in this chapter the convention for the axis directions is taken as it is defined in BOUT++. See Fig. 5.1

magnitude of the magnetic field is chosen in such a way that it does not affect the motion of the ions, that is, the ion Larmor radius is much larger than the characteristic length of the channel. The model is a 2D model with a geometry corresponding to the axial-azimuthal domain (see Fig. 5.1) where the background electric field is fixed in the axial direction, $\mathbf{E}_0 = E_0\hat{\mathbf{x}}$ [1], resulting in an electron drift in the azimuthal direction, $\hat{\mathbf{z}}$. The background plasma density and magnetic field gradients have gradients in the axial direction.

This model includes gradients in the plasma density while neglecting magnetic field and electron temperature gradients. Also included in the model are electron collisions with neutrals thus providing a coupling between the gradient drift instabilities due to density gradients and the resistive instabilities due to electron-neutral collisions [12]. Plasma is assumed to be quasineutral and the electric field is electrostatic. Ion are collisionless, unmagnetized and cold, $T_i = 0$. For simplicity , the ion dynamics is assumed to be linear [2].

The ion continuity and momentum equations are

$$\frac{\partial n_i}{\partial t} + \nabla \cdot (n_i \mathbf{v}_i) = 0, \tag{5.1}$$

$$\frac{\partial \mathbf{v}_i}{\partial t} + (\mathbf{v}_i \cdot \nabla)\mathbf{v}_i = -\frac{e}{m_i}\nabla\phi. \tag{5.2}$$

In order to study the perturbations in the system, it is assumed that all relevant quantities can be described as the sum of a background and a fluctuating component, $\alpha = \alpha_0 + \tilde{\alpha}$, $\alpha_0 >> \tilde{\alpha}$, such that $\tilde{\alpha} = \tilde{\alpha}_0 e^{i(\mathbf{k}\cdot\mathbf{r} - \omega t)}$.

With this into account, the ion continuity equation can be written as

$$\frac{\partial n}{\partial t} = -\mathbf{v}_0 \cdot \nabla_\perp n + n_0 \nabla_\perp \cdot \mathbf{v}_i. \tag{5.3}$$

The ion dynamics can be conveniently described by the potential function $\mathbf{v}_i = -\nabla\chi$, after which the ion continuity equation takes the form

$$\frac{\partial n}{\partial t} = -\mathbf{v}_0 \cdot \nabla_\perp n + n_0\theta, \tag{5.4}$$

$$\theta = \nabla_\perp^2 \chi. \tag{5.5}$$

The ion momentum equation can be written as

$$\frac{\partial \mathbf{v}_i}{\partial t} = -(\mathbf{v}_0 \cdot \nabla_\perp)\mathbf{v}_i - \frac{e}{m_i}\nabla_\perp\phi, \tag{5.6}$$

[2] Nonlinear extensions to the ion dynamics can be the subject of future work.

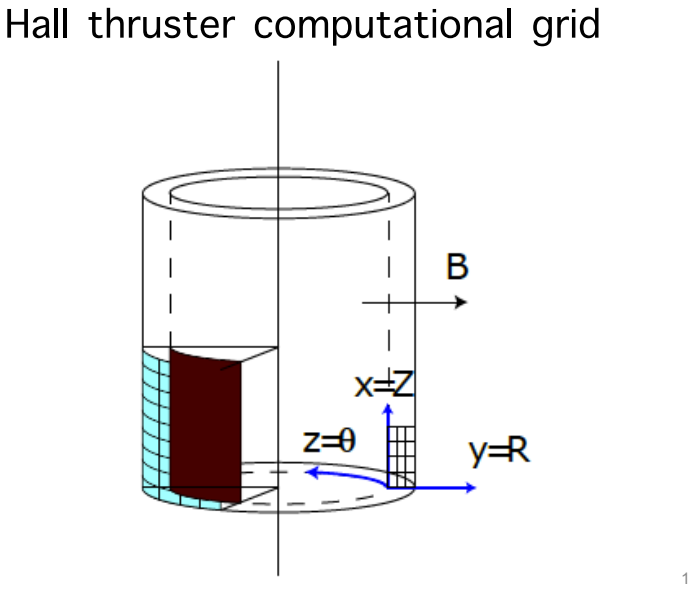

Figure 5.1: Schematics of the geometry of a Hall thruster and the computational grid for Eqs. (5.35)–(5.37). The magnetic field is mainly in the radial direction, the electric field and the density gradients are in the axial direction, while the electron $\mathbf{E}_0 \times \mathbf{B}_0$ drift is in the azimuthal direction. In the grid used by BOUT++, the axial, radial and azimuthal directions correspond to the $\hat{\mathbf{x}}$, $\hat{\mathbf{y}}$ and $\hat{\mathbf{z}}$ coordinates respectively.

which, after taken the divergence, reduces to

$$\frac{\partial \theta}{\partial t} = -\mathbf{v}_0 \cdot \nabla_\perp \theta + \frac{e}{m_i} \nabla_\perp^2 \phi. \tag{5.7}$$

The electron continuity equation is written as

$$\frac{\partial n_e}{\partial t} + n_e \nabla_\perp \cdot \mathbf{v}_{e\perp} + \mathbf{v}_{e\perp} \cdot \nabla_\perp n_e = 0. \tag{5.8}$$

The electron momentum conservation equation in the perpendicular (to the magnetic field) direction is given by

$$m_e n_e \frac{d\mathbf{v}_{e\perp}}{\partial t} = e n_e (-\nabla_\perp \phi + \mathbf{v}_{e\perp} \times \mathbf{B}) - \nabla_\perp p_e - m_e n_e \nu \mathbf{v}_{e\perp} - \nabla \cdot \mathbf{\Pi}_g, \tag{5.9}$$

where the substantive derivative is

$$\frac{d}{dt} = \frac{\partial}{\partial t} + \mathbf{v}_{e\perp} \cdot \nabla, \tag{5.10}$$

and $\mathbf{\Pi}_g$ is the gyroviscosity tensor.

Assuming that $d/dt \ll \omega_{ce}$, the electron velocity in Eq. (5.9) can be written as [113]

$$\mathbf{v}_{e\perp} = \mathbf{v}_{\mathbf{E}} + \mathbf{v}_{pe} + \mathbf{v}_I + \mathbf{v}_\nu + \mathbf{v}_{\Pi_g}, \tag{5.11}$$

where $\mathbf{v}_{\mathbf{E}}$ is the $\mathbf{E}\times\mathbf{B}$ drift velocity, $\mathbf{v}_{pe}$ is the diamagnetic drift velocity and $\mathbf{v}_I$, $\mathbf{v}_\nu$ and $\mathbf{v}_{\Pi_g}$ are the drift velocities associated with the inertia, collisions and the gyroviscosity tensor,

$$\mathbf{v}_{\mathbf{E}} = \frac{\mathbf{b}}{B_0}\times\nabla_\perp\phi, \mathbf{v}_{pe} = -\frac{1}{en_e}\frac{\mathbf{b}}{B_0}\times\nabla_\perp p_e,$$
$$\mathbf{v}_I = \frac{1}{\omega_{ce}}\mathbf{b}\times\frac{d}{dt}\left(\mathbf{v}_{\mathbf{E}}+\mathbf{v}_{pe}\right), \mathbf{v}_\nu = \frac{\nu}{\omega_{ce}}\mathbf{b}\times\left(\mathbf{v}_{\mathbf{E}}+\mathbf{v}_{pe}\right), \mathbf{v}_{\Pi_g} = \frac{1}{m_e n_e\omega_{ce}}\mathbf{B}\times\nabla\cdot\mathbf{\Pi}_g. \tag{5.12}$$

The gyroviscosity tensor in this last equation is given by [3] [114]

$$\mathbf{\Pi}_g = \frac{1}{\omega_{ce}}\hat{\mathbf{K}}^{-1}\left(\left[p\nabla\mathbf{v}+p\left(\nabla\mathbf{v}\right)^T\right]+\frac{2}{5}\left[\nabla\mathbf{q}+\left(\nabla\mathbf{q}\right)^T\right]\right), \tag{5.13}$$

where the operator $\hat{\mathbf{K}}^{-1}$ acting on a (symmetric) tensor $\mathbf{A}$ is [114]

$$\hat{\mathbf{K}}^{-1}\mathbf{A} = \frac{1}{4}\left\{\left[\mathbf{b}\times\mathbf{A}\cdot\left(\mathbf{1}+3\mathbf{bb}\right)\right]+\left[\mathbf{b}\times\mathbf{A}\cdot\left(\mathbf{1}+3\mathbf{bb}\right)\right]^T\right\}. \tag{5.14}$$

The gyroviscous force (that is a finite Larmor radius effect correction to the momentum balance equation) has a contribution to the momentum balance equation of the same order as the inertia [113, 114]. The fact that the gyroviscosity and the inertia contributions to the electron momentum equation are of the same order leads to the so called gyroviscous cancellation. The general form of the gyroviscous cancellation is of the form [113]

$$m_e n_e\left(\mathbf{v}_{pe}\cdot\nabla\right)\mathbf{v}_{e\perp}+\nabla\cdot\mathbf{\Pi}_g = \nabla\xi^{'}, \tag{5.15}$$

where $\xi^{'}$ is some scalar function [4].

Taking into account the gyroviscous cancellation from Eq. (5.15) and assuming isothermal electrons, the perpendicular electron velocity from Eq. (5.12) becomes

$$\mathbf{v}_{e\perp} = {\mathbf{v}_{\mathbf{E}}}^{(0)} + {\mathbf{v}_{\mathbf{E}}}^{(1)}, \tag{5.16}$$
$${\mathbf{v}_{\mathbf{E}}}^{(0)} = \frac{\mathbf{b}}{B_0}\times\nabla_\perp\phi - \frac{T_e}{en_e}\frac{\mathbf{b}}{B_0}\times\nabla_\perp n_e = \mathbf{v}_{\mathbf{E}}+\mathbf{v}_{pe}, \tag{5.17}$$
$${\mathbf{v}_{\mathbf{E}}}^{(1)} = \frac{e}{m_e}\frac{1}{\omega_{ce}^2}\left(\frac{\partial}{\partial t}+\mathbf{v}_{\mathbf{E}}\cdot\nabla+\nu\right)\nabla_\perp\left(\phi-\frac{T_e}{e}\frac{n_e}{n_0}\right). \tag{5.18}$$

[3] In the expression for $\mathbf{\Pi_g}$, $\mathbf{v}=\mathbf{v_E}+\mathbf{v_{pe}}$ and the heat flux $\mathbf{q}=\frac{5}{2}\frac{\mathbf{p_e}}{\mathbf{eB}}\mathbf{b}\times\nabla\mathbf{T_e}$.

[4] The calculation of the gyroviscous cancellation is in general not easy and tedious. For more details, the reader is referred to Ref. [113].

To obtain the final equation of the system, the quasineutralty condition along with the expression for the electron velocity in Eq. (5.16), are used in the electron continuity equation (5.8), assuming that there are no gradients in the magnetic field

$$\frac{\partial n}{\partial t}+\nabla\cdot\left[n\frac{\mathbf{b}}{B_0}\times\nabla_\perp\phi-n\frac{T_e}{en}\frac{\mathbf{b}}{B_0}\times\nabla_\perp n+\frac{en}{m_e}\frac{1}{\omega_{ce}^2}\frac{\partial}{\partial t}\left(\nabla_\perp\phi-\frac{T_e}{en}\nabla_\perp n\right)\right.$$
$$+\frac{en}{m_e}\frac{1}{\omega_{ce}^2}\frac{\mathbf{b}}{B_0}\times\nabla_\perp\phi\cdot\nabla_\perp\left(\nabla_\perp\phi-\frac{T_e}{en}\nabla_\perp n\right)$$
$$\left.+\frac{en}{m_e}\frac{\nu_e}{\omega_{ce}^2}\left(\nabla_\perp\phi-\frac{T_e}{en}\nabla_\perp n\right)\right]=0. \tag{5.19}$$

By opening the brackets, the equation becomes

$$\frac{\partial}{\partial t}\left[\frac{en_0}{m_e}\frac{1}{\omega_{ce}^2}\nabla_\perp^2\left(\phi-\frac{T_e}{e}\frac{n}{n_0}\right)+n\right]+u_0\frac{\partial}{\partial z}\left[\frac{en_0}{m_e}\frac{1}{\omega_{ce}^2}\nabla_\perp^2\left(\phi-\frac{T_e}{e}\frac{n}{n_0}\right)+n\right]$$
$$+\nu_e\left[\frac{en_0}{m_e}\frac{1}{\omega_{ce}^2}\nabla_\perp^2\left(\phi-\frac{T_e}{e}\frac{n}{n_0}\right)+n\right]-\nu_e n+\frac{n_0}{B_0}\left(\frac{1}{n_0}\frac{\partial n_0}{\partial x}\right)\frac{\partial\phi}{\partial z}+\frac{1}{B_0}\{n,\phi\}$$
$$+\nabla\cdot\left[\frac{en}{m_e}\frac{1}{\omega_{ce}^2}\frac{\mathbf{b}}{B_0}\times\nabla_\perp\phi\cdot\nabla_\perp\left(\nabla_\perp\phi-\frac{T_e}{en}\nabla_\perp n\right)\right]=0 \tag{5.20}$$

where the last two quantities contain the main nonlinearities of the equation. Here, the quantity in the curly brackets in the second to last member is the Poisson bracket, defined as

$$\{A,B\}=\frac{\partial A}{\partial x}\frac{\partial B}{\partial z}-\frac{\partial A}{\partial z}\frac{\partial B}{\partial x}.$$

The expression under the divergence can be reduced using

$$\frac{en_0}{m_e\omega_{ce}^2}\frac{\mathbf{b}}{B_0}\times\nabla_\perp\phi\cdot\nabla_\perp\left(\nabla_\perp\phi-\frac{T_e}{en}\nabla_\perp n\right)=\frac{1}{B_0}\left\{\frac{en_0}{m_e}\frac{1}{\omega_{ce}^2}\nabla_\perp\left(\phi-\frac{T_e}{e}\frac{n}{n_0}\right),\phi\right\}. \tag{5.21}$$

The divergence of this Poisson bracket quantity can be calculated using the identity $\nabla\cdot\{\phi,\nabla_\perp\Sigma\}=\{\phi,\nabla_\perp^2\Sigma\}+\{\nabla_\perp\phi,\nabla_\perp\Sigma\}$ to obtain the final form of the electron continuity equation [113, 115]

$$\frac{\partial}{\partial t}\left[\frac{en_0}{m_e}\frac{1}{\omega_{ce}^2}\nabla_\perp^2\left(\phi-\frac{T_e}{e}\frac{n}{n_0}\right)+n\right]+u_0\frac{\partial}{\partial z}\left[\frac{en_0}{m_e}\frac{1}{\omega_{ce}^2}\nabla_\perp^2\left(\phi-\frac{T_e}{e}\frac{n}{n_0}\right)+n\right]$$
$$+\nu_e\left[\frac{en_0}{m_e}\frac{1}{\omega_{ce}^2}\nabla_\perp^2\left(\phi-\frac{T_e}{e}\frac{n}{n_0}\right)+n\right]-\nu_e n+\frac{n_0}{B_0}\left(\frac{1}{n_0}\frac{\partial n_0}{\partial x}\right)\frac{\partial\phi}{\partial z}$$
$$+\frac{1}{B_0}\left\{\frac{en_0}{m_e}\frac{1}{\omega_{ce}^2}\nabla_\perp^2\left(\phi-\frac{T_e}{e}\frac{n}{n_0}\right)+n,\phi\right\}$$
$$+\frac{1}{B_0}\left\{\frac{en_0}{m_e}\frac{1}{\omega_{ce}^2}\nabla_\perp\left(\phi-\frac{T_e}{e}\frac{n}{n_0}\right),\nabla_\perp\phi\right\}=0. \tag{5.22}$$

The electron continuity equation reduces to the time evolution of the vorticity ϖ

$$\frac{\partial \varpi}{\partial t} + u_0 \frac{\partial \varpi}{\partial z} + \nu_e \varpi - \nu_e \left(\frac{n}{n_0} \right) + v_n \frac{\partial}{\partial z} \left(\frac{e\phi}{T_e} \right) + \frac{T_e}{eB_0} \left\{ \varpi, \frac{e\phi}{T_e} \right\} + \frac{T_e}{eB_0} \rho_e^2 \left\{ \nabla_\perp \left(\frac{e\phi}{T_e} \right), \nabla_\perp \left(\frac{n}{n_0} \right) \right\} = 0, \tag{5.23}$$

where [5]

$$\varpi = \rho_e^2 \nabla_\perp^2 \left(\frac{e\phi}{T_e} - \frac{n}{n_0} \right) + \frac{n}{n_0}, \quad v_n = \frac{T_e}{eB_0} \left(\frac{1}{n_0} \frac{\partial n_0}{\partial x} \right). \tag{5.24}$$

5.3 Linear Dispersion Relation

Assuming that the quantities have a harmonic time and space dependence and keeping only the linear terms in the system of equations (5.4), (5.7) and (5.23), the following dispersion relation for the linear modes in the Hall thruster plasma is obtained

$$\frac{\left(\omega - \omega_0 + i\nu_e\right) k_\perp^2 \rho_e^2 + \omega_n}{\left(\omega - \omega_0 + i\nu_e\right) k_\perp^2 \rho_e^2 + \omega - \omega_0} = \frac{k_\perp^2 c_s^2}{\left(\omega - k_x v_0\right)^2}. \tag{5.25}$$

This dispersion relation is an extension of the dispersion relation in Eq. (3.18) [11] to include electron collisions and electron inertia.

5.3.1 Lower hybrid instability

The lower hybrid oscillation is a longitudinal oscillation of ions and electrons in a magnetized plasma. The direction of propagation must be very nearly perpendicular to the stationary magnetic field. If electron collisions, density gradients and the ion equilibrium flow are neglected in Eq. (5.25), the dispersion relation reduces to

$$\frac{k_\perp^2 \rho_e^2}{1 + k_\perp^2 \rho_e^2} = \frac{k_\perp^2 c_s^2}{\omega^2}, \tag{5.26}$$

whose solution is

$$\omega^2 = \frac{c_s^2}{\rho_e^2} \left(1 + k_\perp^2 \rho_e^2\right) = \omega_{lh}^2 + k_\perp^2 c_s^2 = \omega_{lh}^2 \left(1 + k_\perp^2 \rho_e^2\right). \tag{5.27}$$

[5] The term under the brackets in the continuity equation is rearranged to give $\frac{e n_0}{m_e} \frac{1}{\omega_{ce}^2} \nabla_\perp^2 \left(\phi - \frac{T_e}{e} \frac{n}{n_0} \right) = n_0 \rho_e^2 \nabla_\perp^2 \left(\frac{e\phi}{T_e} - \frac{n}{n_0} \right)$

Equation (5.27) was obtained previously in Chapter 2, see Eq. (2.97). The lower hybrid mode can be rendered unstable by including the effect of the electron collisions. Keeping the electron collision term in Eq. (5.25), while neglecting density gradients, the dispersion relation becomes

$$\frac{(\omega - \omega_0 + i\nu_e)\,(\omega - k_x v_0)^2}{(\omega - \omega_0)\,(1 + k_\perp^2 \rho_e^2) + i\nu_e\, k_\perp^2 \rho_e^2} = \frac{k_\perp^2 c_s^2}{k_\perp^2 \rho_e^2} = \omega_{lh}^2. \tag{5.28}$$

Under the assumption that $k_\perp^2 \rho_e^2$ is a small term, Eq. (5.28) reduces to the cubic equation

$$\begin{aligned} (\omega - \omega_0 + i\nu)(\omega - k_x v_0)^2 &= \omega_{lh}^2(\omega - \omega_0), \\ \left(1 + \frac{i\nu}{\omega - \omega_0}\right)(\omega - k_x v_0)^2 &= \omega_{lh}^2. \end{aligned} \tag{5.29}$$

The cubic equation in the dispersion relation given by Eq. (5.29) can be simplified to a quadratic equation if it is assumed that the azimuthal equilibrium $\mathbf{E}_0 \times \mathbf{B}_0$ flow frequency is much larger than both the electron collision frequency and the characteristic frequency of the system i. e. that $|\omega| << |\omega_0|$ and $|\nu| << |\omega_0|$ (which is the case, for example, around the exit region of a Hall thruster, where the peak of the magnetic field is located). When these two assumptions are met, the dispersion relation reduces to

$$\omega = k_x v_0 \pm \omega_{lh}\left(1 + \frac{i\nu}{2\omega_0}\right). \tag{5.30}$$

This dispersion relation, that describes the lower hybrid mode rendered unstable by electron collisions and with the $\mathbf{E}_0 \times \mathbf{B}_0$ drift as free energy source and is discussed extensively in Ref. [13]. The real part of the frequency in Eq. (5.30) is given by the lower hybrid frequency, shifted by the axial equilibrium ion flow frequency $k_x\, v_0$ while the growth rate of the instability is proportional to the electron collision frequency and decreases with increasing azimuthal wavevector.

In the regions where the above mentioned conditions ($|\omega| << |\omega_0|$ and $|\nu| << |\omega_0|$) are not met, the dispersion relation is described by a cubic equation. In this case, the real part of the frequency increases with increasing azimuthal wavenumber until it approaches the lower hybrid frequency. For values of the real part of the frequency smaller than the lower hybrid frequency, $\omega < \omega_{lh}$, the real part of the frequency is approximately equal to the azimuthal equilibrium $\mathbf{E}_0 \times \mathbf{B}_0$ flow frequency ω_0, that is $\omega_r \approx \omega_0$.

5.3.2 Effect of the electron inertia on the gradient drift instability

Equation (5.25) contains a modification of the dispersion relation of the density gradient drift modes described by Eq. (3.28) and studied in Chapter 3, that includes the effect of electron inertia. Neglecting collisions, the general dispersion relation (5.25) becomes

$$k_\perp^2 \rho_e^2 + \frac{\omega_n}{\omega - \omega_0} = \frac{k_\perp^2 c_s^2}{\omega^2}. \tag{5.31}$$

By expanding this last dispersion relation, the following cubic equation for the frequency is obtained

$$k_\perp^2 \rho_e^2 \omega^3 + (\omega_n - k_\perp^2 \rho_e^2 \omega_0)\omega^2 - k_\perp^2 c_s^2 \omega + k_\perp^2 c_s^2 \omega_0 = 0.$$

Assuming that $|\omega| << |\omega_0|$, the cubic equation reduces to a quadratic equation

$$(\omega_n - k_\perp^2 \rho_e^2 \omega_0)\omega^2 - k_\perp^2 c_s^2 \omega + k_\perp^2 c_s^2 \omega_0 = 0, \tag{5.32}$$

whose solution is given by

$$\omega = \frac{1}{2} \frac{k_\perp^2 c_s^2}{\omega_n - k_\perp^2 \rho_e^2 \omega_0} \left(1 \pm \sqrt{1 - \frac{4\omega_0(\omega_n - k_\perp^2 \rho_e^2 \omega_0)}{k_\perp^2 c_s^2}} \right) \tag{5.33}$$

From the solution to the dispersion relation, it is seen that the system is stable for

$$\omega_n - k_\perp^2 \rho_e^2 \omega_0 < 0,$$

or

$$k_y \, k_n - k_\perp^2 \frac{\omega_0}{\omega_{ce}} < 0.$$

In the case of purely azimuthal propagation, $k_\perp = k_y$, the instability condition reduces to

$$\frac{k_n}{k_y} < \frac{\omega_0}{\omega_{ce}}, \qquad \frac{R_t}{L_n} < m \, \frac{\omega_0}{\omega_{ce}}. \tag{5.34}$$

This condition means that for high enough k_y (high mode number m), the instability disappears. This in contrast to the dispersion relation in Eq. (3.28) obtained without taking into account the electron inertia, that predicts that the instability always grows with the azimuthal wavenumber.

5.4 Linear benchmarks and nonlinear simulations

The system of equations (5.4), (5.7) and (5.23) yields the general dispersion relation (5.25). The general dispersion relation contains the gradient drift modes as well as the lower hybrid and the resistive mode rendered unstable by electron collisions [13]. To perform numerical simulations with BOUT++, as well as to obtain the real part of the frequency and the growth rate for the different modes, it is suitable to write the equations in dimensionless form. To accomplish this task, the following system of units is used for normalization, $t^{'} \rightarrow \omega_{lh} t$, $\nabla \rightarrow (1/\rho_l)\nabla^{'}$, $v \rightarrow c_l v^{'}$, $\phi \rightarrow (T_e/e)\phi^{'}$, $n \rightarrow n_0 n^{'}$, $c_l^2 = T_e/\sqrt{m_i m_e}$, $\rho_l = c_l/\omega_{lh}$, $\omega_{lh} = \sqrt{\omega_{ci}\omega_{ce}}$:

$$\frac{\partial n}{\partial t} = -v_0 \frac{\partial n}{\partial x} + \theta, \tag{5.35}$$

$$\frac{\partial \theta}{\partial t} = -v_0 \frac{\partial \theta}{\partial x} + \mu_e \nabla_\perp^2 \phi, \tag{5.36}$$

$$\frac{\partial \varpi}{\partial t} = -u_0 \frac{\partial \varpi}{\partial z} - \nu_e \varpi + \nu_e n - v_n \frac{\partial \phi}{\partial z} + \{\phi, \varpi\} + \mu_e \{\nabla_\perp n, \nabla_\perp \phi\} - D_\varpi \nabla^4 \varpi, \tag{5.37}$$

$$\varpi = \mu_e \nabla_\perp^2 (\phi - n) + n, \mu_e = \sqrt{m_e/m_i}.$$

Equations (5.35) - (5.37) are written in the coordinate convention assumed in BOUT++, namely the axial direction is along the $\hat{\mathbf{x}}$ axis, the radial direction is along the $\hat{\mathbf{y}}$ axis and the $\mathbf{E}_0 \times \mathbf{B}_0$ azimuthal direction is along the $\hat{\mathbf{z}}$ axis. A schematic of the computational grid used to solve the system in Eqs. (5.35)–(5.37) is shown in Fig. 5.1.

To benchmark the code the initial value linear simulation results are compared with the solution of the 1D (azimuthal) linear eigenvalue problem described in Ref. [13]. This comparison is shown in Fig. 5.2.

In the nonlinear simulations presented here, the gradient drift modes are neglected by assuming uniform plasma density and magnetic field. This leaves only the resistive low hybrid mode instability as a source of plasma turbulence [13]. This way, the system of nonlinear equations solved is given by

$$\frac{\partial n}{\partial t} = \theta, \tag{5.38}$$

$$\frac{\partial \theta}{\partial t} = \sqrt{\frac{m_e}{m_i}} \nabla_\perp^2 \phi, \tag{5.39}$$

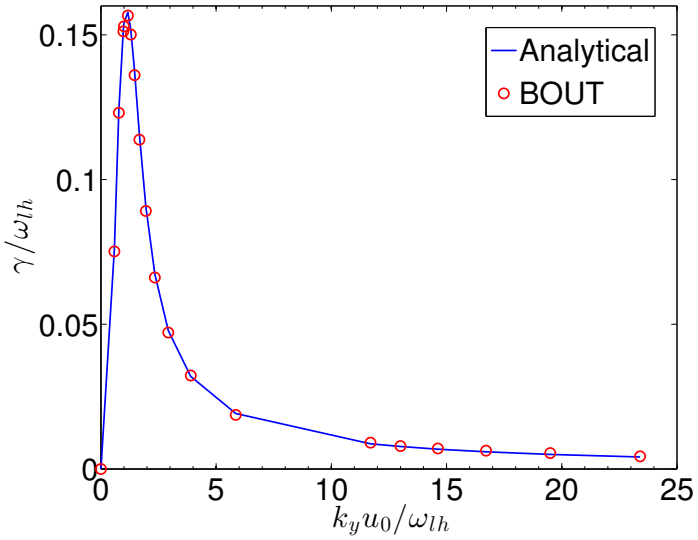

(a)

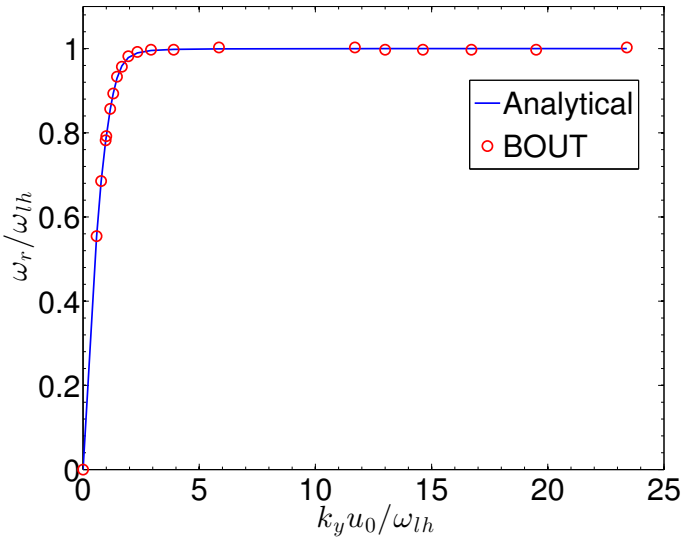

(b)

Figure 5.2: Real part of the frequency and growth rate of the resistive instability described in Ref. [13] as a function of the azimuthal wavenumber. The solid line represents the analytical solution to the dispersion relation while the red circles represent the simulations results.

$$\frac{\partial \varpi}{\partial t} = -u_0 \frac{\partial \varpi}{\partial z} - \nu_e \varpi + \nu_e n + \{\phi, \varpi\} - D_\varpi \nabla^4 \varpi, \tag{5.40}$$

$$\varpi \;\; = \;\; \sqrt{\frac{m_e}{m_i}}\, \nabla_\perp^2 \phi + n \tag{5.41}$$

The nonlinear equations were solved using a rectangular mesh with 128×256 points in the axial and azimuthal directions for three different initial profiles of the perturbed plasma parameters, namely the product of a sinusoidal function and a gaussian, a purely gaussian perturbation and a purely sinusoidal perturbation using Dirichlet boundary conditions for these perturbations. The saturation of the instability in the system was studied by checking the energy type integral

$$E_n = \int |n|^2 \, dx dz. \tag{5.42}$$

The energy calculated from Eq. (5.42) is shown in Fig 5.3 for the three different initial states.

From Fig. 5.3, it can be seen that the energy saturates after around t = 400. Though, the time to reach saturation could be different, the final turbulent state is generally independent of the initial conditions.

5.5 Anomalous electron current

The perturbed nonlinear electron density can be expressed by the product of the perturbed electron density and the perturbed electron velocity. This current density is then

$$\mathbf{J}_e = -e\, \widetilde{n}\, \widetilde{\mathbf{u}}_e. \tag{5.43}$$

In this equation, the perturbed electron velocity, $\widetilde{\mathbf{u}}_e$ is the perturbed electron $\mathbf{E} \times \mathbf{B}$ drift velocity produced by the perturbed electric field and the radial magnetic field

$$\widetilde{\mathbf{u}}_e = \frac{\hat{\mathbf{b}}}{B_0} \times \nabla \widetilde{\phi} = \frac{1}{B_0} \frac{\partial \widetilde{\phi}}{\partial z} \hat{\mathbf{x}} - \frac{1}{B_0} \frac{\partial \widetilde{\phi}}{\partial x} \hat{\mathbf{z}}. \tag{5.44}$$

Using Eqs. (5.44) and (5.43), the axial current density becomes

$$J_{ex} = -\frac{e\, \widetilde{n}}{B_0} \frac{\partial \widetilde{\phi}}{\partial z}. \tag{5.45}$$

The local value of the oscillating electron current given by the equation (5.45) is space averaged at every time step

$$\bar{J}_{ex}(t) = \frac{1}{L_z\, L_x} \int \int \tilde{n}(t, x, z) \frac{\partial \tilde{\phi}(t, x, z)}{\partial \tilde{z}} \, dx \, dz. \tag{5.46}$$

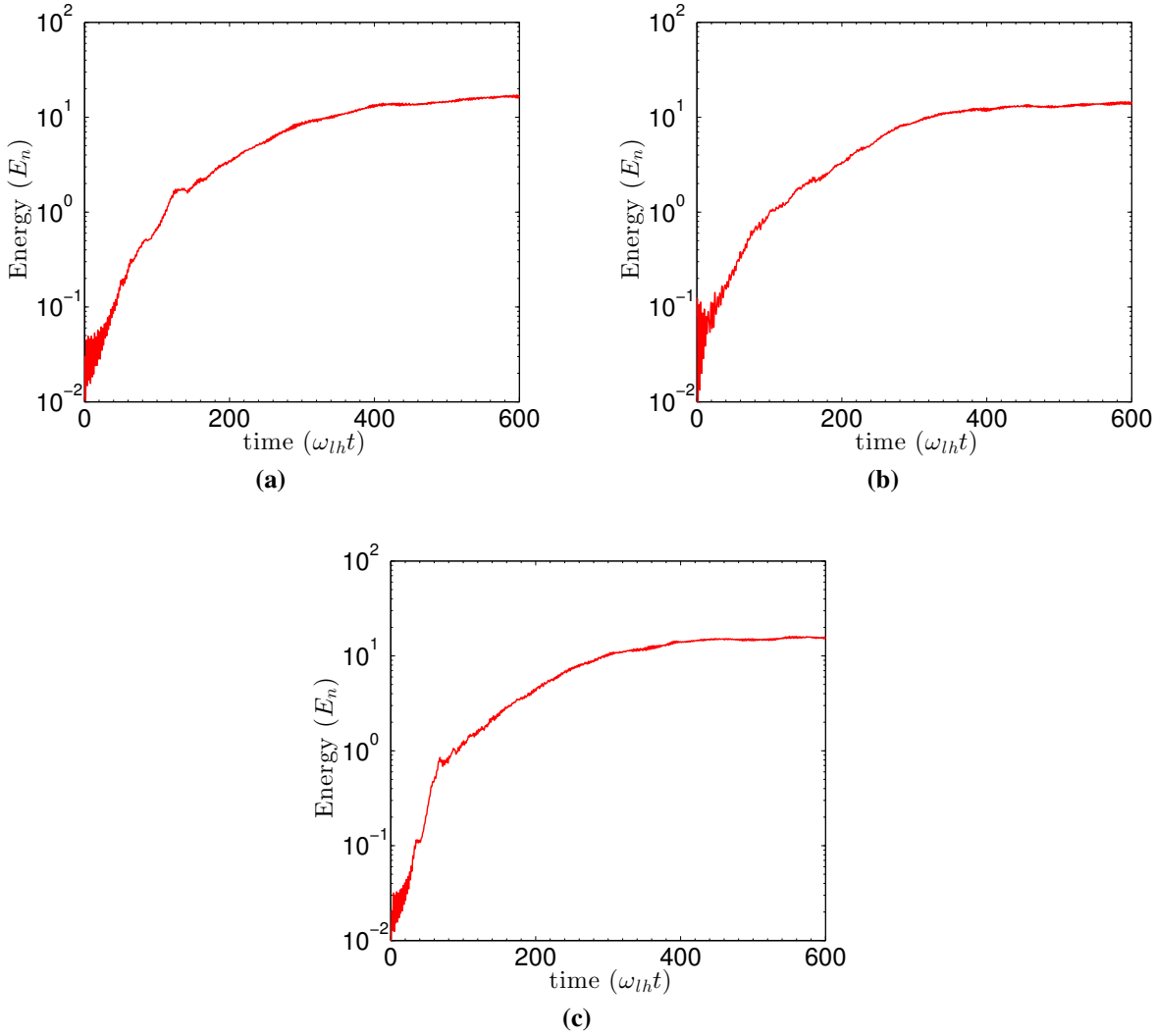

Figure 5.3: Saturation of the energy integral as a function of time ($\omega_{ln}t$) for three different initial states: a) Product of sinusoidal and gaussian, b) Gaussian, c) Sinusoidal.

The classical collisional current density is given by

$$J_{ex_{classical}} = \frac{en_0}{B_0}\frac{\nu_e}{\omega_{ce}}E_0. \tag{5.47}$$

The classical current in Eq. (5.47) can be also written in terms of a dimensionless parameter, called the Hall parameter, as

$$\begin{aligned} J_{ex_{classical}} &= \frac{en_0}{B_0}\frac{\nu_e}{\omega_{ce}}E_0 = \frac{en_0}{B_0}\frac{E_0}{\Omega_H}, \\ \Omega_H &= \frac{\omega_{ce}}{\nu_e}. \end{aligned} \tag{5.48}$$

The perturbed axial current density calculated from Eq. (5.46), along with the mean average value over a lower hybrid period and the classical current density given by Eq. (5.47) are shown in Fig. (5.4).

5.6 Scaling of the anomalous electron current with plasma parameters

As was demonstrated in the previous section, the fluctuating electron current reaches the same saturated state regardless of the initial conditions. In this section how the axial electron current in saturation depends on plasma parameters such as the ion mass, the background magnetic field, the electron neutral collision frequency and the background electric field is studied.

To study the scaling of the electron current with the ion mass, the simulations are run for four different ion species, Ar, Kr, Xe and Bi. These ion species have a mass number, AA, of 40, 84, 131 and 209, respectively and have all been considered as candidates for the propellant of a Hall thruster. The axial electron current density for the different ion species, assuming a background magnetic field B of 150 G and a collision frequency (normalized to ω_{lh}) of 0.2, is shown in Fig. 5.5a. As can be seen from Fig. 5.5a, the axial electron current density decreases with smaller ion mass. The axial electron current density dependence on the ion mass has been determined to be

$$J_{ex} \sim 1/\sqrt{m_i}. \tag{5.49}$$

Another important parameter that affects the axial electron density is the external magnetic field. The simulations are run for four typical values of the magnetic field inside a Hall thruster.

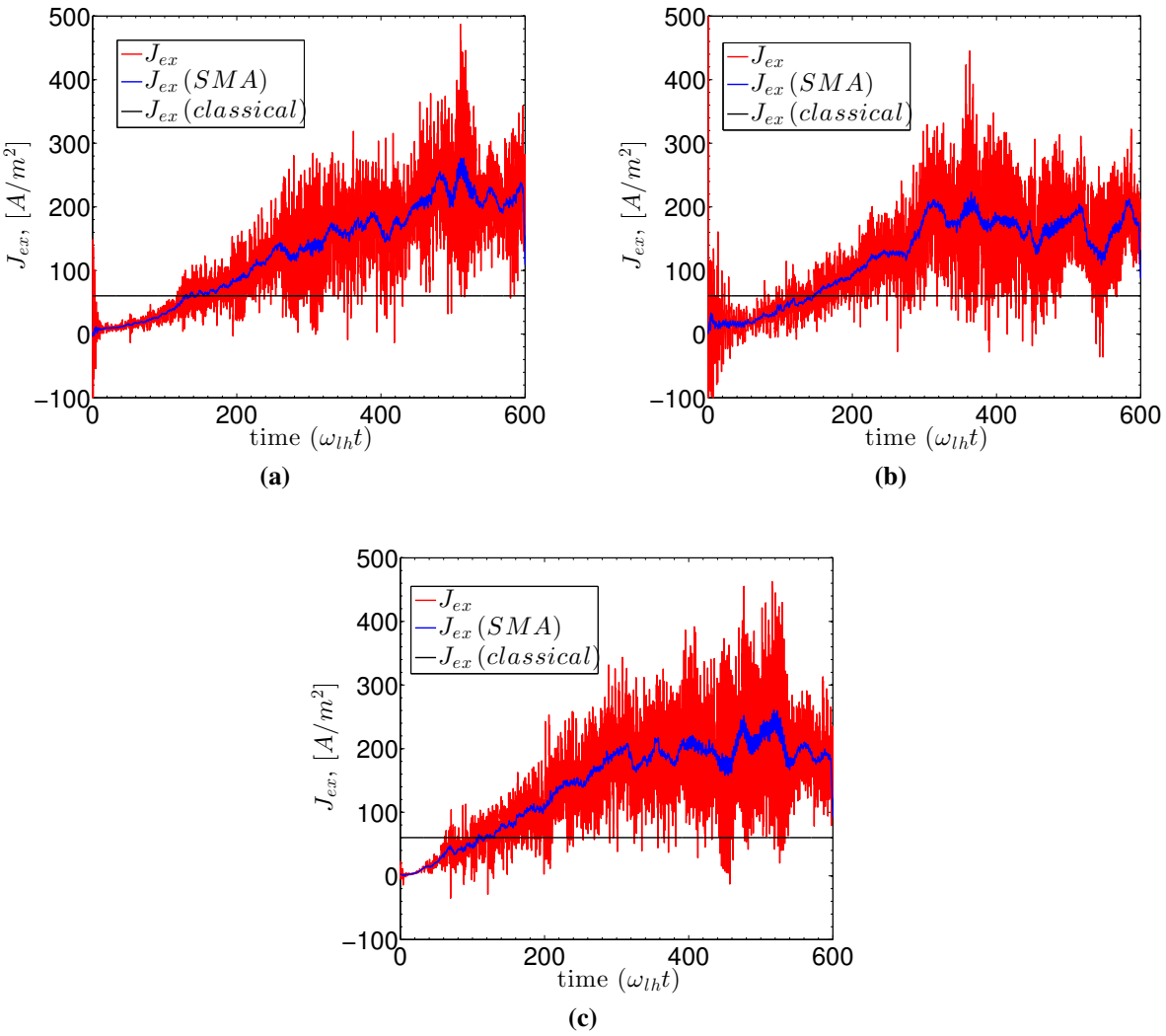

Figure 5.4: Axial current density as a function of normalized time ($\omega_{ln}t$) for cold electrons model for three different initial profiles for plasma parameters. a) Product of sinusoidal and gaussian, b) Gaussian, c) Sinusoidal. The value of the classical current density is $J_{ex}(classical)$ = 60 A/m^2.

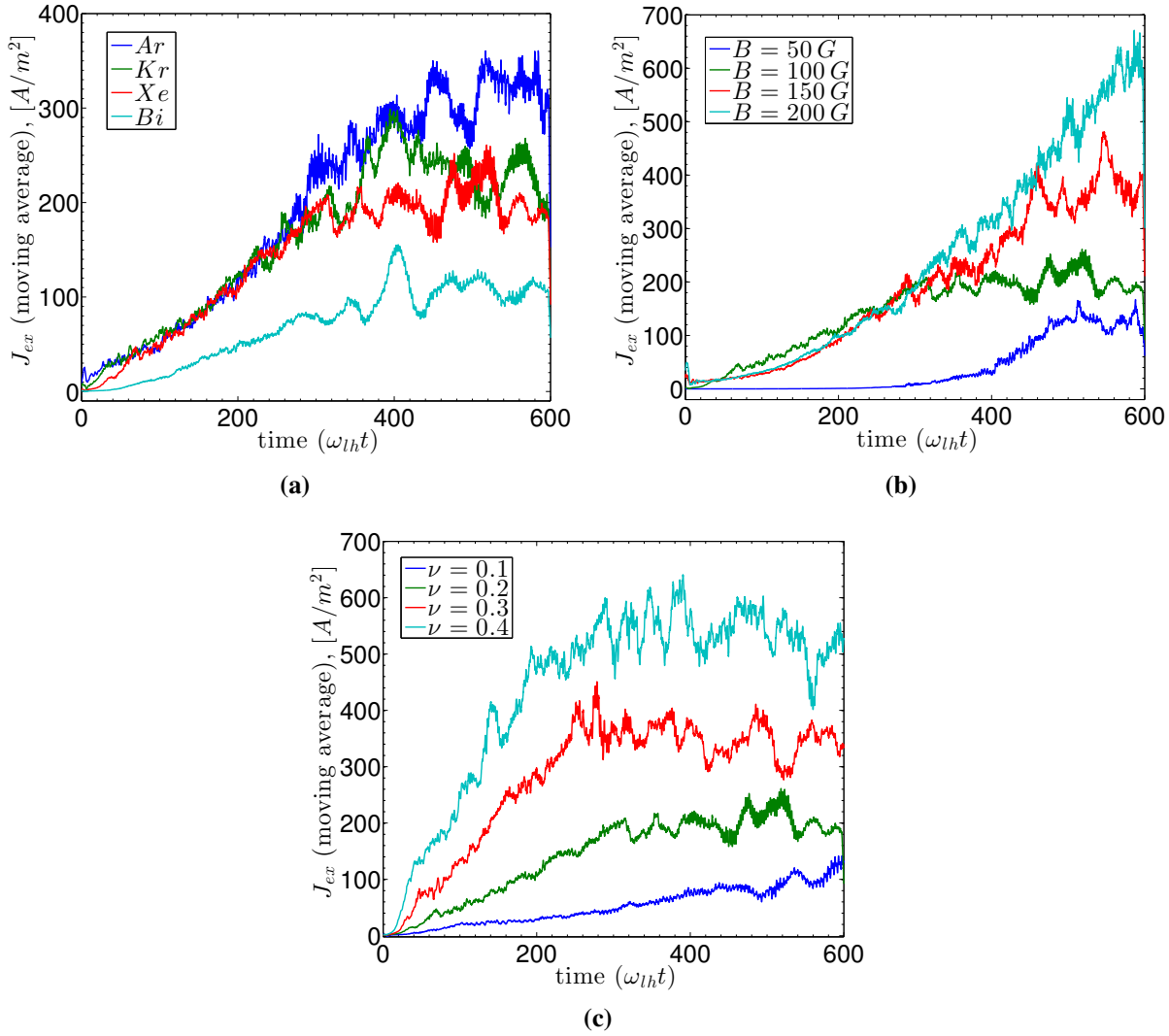

Figure 5.5: Axial current density as a function of normalized time ($\omega_{ln}t$) for cold electrons model for a) four different ion species, Ar, Kr, Xe and Bi, b) four different values of the equilibrium magnetic field and c) four different values of the electron neutral collision frequency. The values for the parameters held constant for the calculations are ion mass number, AA = 131 (Xe), B = 150 G and ν_e = 0.2 [ω_{lh}].

The values of the equilibrium magnetic field B_0 chosen are 0.005 T, 0.01 T, 0.015 T and 0.02 T. The axial electron current density for the different values of the equilibrium magnetic field, assuming Xe propellant and a collision frequency (normalized to ω_{lh}) of 0.2, is shown in Fig. 5.5b. As can be seen from Fig. 5.5b, the axial electron current density is larger for larger magnetic field values. The axial electron current density dependence on the equilibrium magnetic field has been determined to be

$$J_{ex} \sim B_0. \tag{5.50}$$

To study the effect of the electron collision frequency, four values of the collision frequency, that correspond to typical values in a Hall thruster are used in the simulations. The values of the normalized (to the lower hybrid frequency ω_{lh}) electron collision frequency, ν_e used in the simulations are ν_e = 0.1, 0.2, 0.3 and 0.4. The axial electron current density for the different values of electron collision frequency, assuming Xe as propellant and a magnetic field, B of 150 G, is shown in Fig. 5.5c. As can be seen from Fig. 5.5c, the axial electron current density is larger for larger collision frequency values. The axial electron current density dependence on the electron collision frequency is

$$J_{ex} \sim \nu_e. \tag{5.51}$$

From the scalings of the axial electron current with the ion mass, the equilibrium magnetic field and the electron collision frequency, a composite scaling can be built in the form

$$J_{ex} \sim \frac{\nu_e B_0}{\sqrt{m_i}} \sim \nu_e \omega_{lh}. \tag{5.52}$$

The (linear) growth rate of the low hybrid instability is given by (see Eq. (5.30)

$$\gamma_{linear} = \omega_{lh} \frac{\nu_e}{2\omega_0}.$$

It seems that the anomalous electron current is proportional to the linear growth rate of the unstable mode.

5.7 Summary

The reduced nonlinear fluid model has been developed to simulate plasma turbulence and anomalous transport in Hall plasmas. The nonlinear model has been implemented in the high performance BOUT++ framework. A linear bench-marking of the BOUT++ initial value simulations

against the results obtained by the eigenvalue solvers has been performed. In the linear simulations a clear transition from gradient driven modes [11, 116] to the low-hybrid modes destabilized by collisions [13] (and density gradients) is observed, with the subsequent decay of the growth rate at high $\mathbf{k}$ values. The saturation of the turbulence and formation of the stationary turbulent spectra in nonlinear simulations are also investigated. It is shown that the nonlinear simulations reach saturation at the level which is independent of the initial state. The related anomalous electron transport has been calculated. It can be seen from Figs. 5.4 that the perturbed current is strongly oscillating and is generally smaller than the classical collisional current during the first stage of the simulation corresponding to the linear phase. Once the nonlinearities start to dominate the system and it approaches saturation, the perturbed current grows and becomes larger than the classical collisional current density. Once the system reaches saturation, the current density also stabilizes. The value of the perturbed current density in saturation state for the values used in the simulations is larger than the classical current density from collisions by a factor of around 6. This indicates that the nonlinear effects are responsible for the anomalous transport observed in Hall plasma experiments.

For the simulations performed in this chapter, the background plasma parameters have been assumed to be constant and in steady state. Since the simulations only model the perturbed plasma parameters, the current obtained from the simulations corresponds to the current due to the plasma perturbations. The parameters used in the simulations correspond to the region where the electrons are strongly magnetized and the strongest deviation from the classical current are expected [20,29].

CHAPTER 6

CONCLUSIONS

Hall thrusters use crossed electric and magnetic fields to ionize and accelerate a propellant gas and generate thrust. Electrons are trapped in closed azimuthal orbits by the mostly radial magnetic and axial electric fields. A neutral propellant gas is injected into the channel and ionized by collisions with the azimuthally orbiting electrons. The produced ions are then accelerated by the electric field and expelled through the thruster channel exit to produce thrust. Due to collisions with neutrals, electrons drift towards the anode. It has been experimentally observed that the electron current to the anode is orders of magnitude higher than the classical collisional electron current. Two main mechanisms have been proposed to explain this observed anomalous transport. Fluctuations are widely thought to be the cause for the observed transport. Electron collisions with the walls (near wall conductivity) is another mechanism that may be responsible for the observed levels of the electron current. It is noted that in the near plume region, outside of the thruster, near wall conductivity is absent while the anomalous transport is high.

The first step towards understanding anomalous transport is to study the range of instabilities observed in a Hall thruster. It is the goal of this dissertation to study some types of instabilities present in a Hall thruster. It has sought to gain insight into the mechanisms that give rise to these instabilities and into how these instabilities can affect the performance of the Hall thruster.

In Chapter 3, the gradient drift instability is studied. This is a class of long wavelength instabilities driven by the electron current, gradients of plasma density, temperature and magnetic field. By using a fluid model, it is shown that a full account of the compressibility of the electron flow in a inhomogeneous magnetic field leads to quantitative modifications of the earlier obtained instability criteria and characteristics of the unstable modes. The modification of the stability criteria due to finite temperature fluctuations is also investigated. It is shown that the instability occurs only when special conditions for the density and magnetic field gradient lengths are satisfied. In a

typical Hall thruster, these instabilities exhibit azimuthal (and axial) oscillations in the frequency spectrum ranging from tens KHz to few MHz, that is often observed in experiments. The azimuthal phase velocity of these modes is typically one order of magnitude lower than the $\mathbf{E} \times \mathbf{B}$ drift velocity and scales inversely with ion mass while the growth rate of these modes scales inversely with the square root of the ion mass, $\gamma \sim 1/\sqrt{m_i}$. The instabilities are localized in two separate regions, near the anode and in the plume region, where the gradient of density and magnetic field are parallel to each other. The instability is absent in the acceleration region. The results obtained in Chapter 3 were published in Refs. [11, 116].

In Chapter 4, a new type of Hall plasma instabilities is studied. These instabilities are related to the excitation of negative energy ion sound types modes driven by the $\mathbf{E} \times \mathbf{B}$ drift. Negative energy mode instabilities arise due to the positive feedback mechanism between the plasma current into the sheath region (and the walls) and the potential fluctuations in the bulk plasma. This feedback mechanism is sensitive to the dielectric properties of the thruster wall material and therefore it is of great importance to the design and construction of Hall thrusters. These modes are studied in the global (average) mode approximation as well as using a local theory. The first approximation uses the average of the plasma density and potential along the direction of the magnetic field. The global modes are characterized by the sheath collision frequency, which is effectively a measure of the transit time between the walls along the magnetic field. In the local theory, variations of the plasma parameters along the magnetic field are included. The local modes can be expressed as the sum of a bulk mode, that propagates along the radial and azimuthal directions, and a purely boundary mode along the azimuthal direction. Both the global and local modes depend explicitly on the material characteristics of the wall, namely on the dielectric constant, ε, of the wall material. The modes are mainly present in the region that is near the peak of the magnetic field and exhibit a real part of the frequency and a growth rate in the 1-10 MHz region for the smallest azimuthal wavenumber. The azimuthal phase velocity for this wavenumber is smaller than the equilibrium $\mathbf{E}_0 \times \mathbf{B}_0$ drift velocity, with the phase velocity decreasing with k_y. Dielectric properties of the wall material were identified as an additional parameter affecting the mode excitation and electron transport. The results from Chapter 4 are published in Refs. [33, 34].

The full picture of plasma instabilities in a Hall thruster is very complex and computer simulations are required to study the plasma dynamics. In Chapter 5, a nonlinear model for simulations

of plasma dynamics in conditions of Hall thrusters is built. The model consists of three fluid equations describing the ion (unmagnetized) motion, the evolution of the quasineutral plasma density and the potential vorticity. The model includes the electron motion due to the electron drifts due to the equilibrium and perturbed electric fields, diamagnetic and electron inertia drifts as well as electron collisional effects. Additionally, the model includes gyroviscosity effects and takes into account the gyroviscous cancellation. Nonlinear effects in the electron and ion convection and vorticity are included. The model has been implemented in BOUT++, which is a finite difference high performance framework for nonlinear plasma fluid simulations in curvilinear magnetic field geometry that was originally developed to study plasma edge turbulence in tokamaks and has been extensively tested. BOUT++ has first been used for simulations of Hall thruster plasmas in this dissertation.

The nonlinear system of fluid equations presented in this dissertation describes several unstable modes. The nonlinear simulations have been performed for low-hybrid modes in Hall plasmas destabilized by collisions. It has been confirmed that initial value linear simulations reproduce the real frequency and growth rates obtained from linear eigenmodes calculations. In the nonlinear simulations the saturation of energy with time has been obtained and it is shown that the nonlinear saturated state is independent of the initial state. The nonlinear electron current form the simulations is also studied. This current also exhibits saturation with time, similar to the one exhibited by the energy. This current is observed to increase with increasing electron neutral collision frequency and magnetic field and to decrease with the square root of the ion mass. This means that the perturbed nonlinear current is proportional to the growth rate of the linear unstable limiting mode. The simulations presented in this dissertation are among the first works providing first principles calculations of the anomalous electron current from turbulent fluctuations. Further work will include expansion of the simulations to include gradient and ionization effects. An important remaining questions relates to the role of kinetic effects, such as Landau damping, on ion sound modes and electron cyclotron resonances [28, 31, 60, 61, 117, 118]. Though fluid equations generally do not include kinetic effects, it is still possible to incorporate linear kinetic interactions via linear closures [119–121]. Such investigations, in particular, those directed toward the studies of the electron cyclotron instability, are currently of large interest for the Hall thruster community [117, 122, 123]. The work presented in this dissertation is also directly relevant to applications

widely used in plasma processing, namely to magnetrons [122, 124–126]. It appears that these systems exhibit fluctuations and transport which are very similar to those observed in Hall thrusters. The diagnostic of fluctuations and transport in these devices is a complex problem. This is in part due to the difficulty of having direct access to the inner regions of the thruster. Therefore, despite significant attention and efforts, an experimental identification of the exact nature of the unstable modes responsible for anomalous transport in Hall thrusters and magnetrons is still lacking. Theoretical studies play then an important role in providing insight and guidance to the experiments that look into the nature of the different modes in Hall plasma devices and the related transport.

As final comment, the author would like to remark that a more complete model of the plasma in a Hall thruster that takes into account the evolution of the full plasma parameters (background and perturbations) can be built in the future as continuation of the work presented in this dissertation. Possible challenges that could arise from attempting to construct such a model and that have not been studied or its effects neglected in the here presented model are related to neutral gas injection, electron injection and beam neutralization by the cathode, neutral dynamics, ionization processes, magnetic field geometry, and wall effects. Such a model would need to be necessarily a full three dimensional model, which adds an additional layer of difficulty. Building and simulating such a model is a very difficult, albeit, interesting endeavour.

REFERENCES

[1] D. M. Goebel and I. Katz. *Fundamentals of Electric Propulsion: Ion and Hall Thrusters*. Wiley, 2008.

[2] V. V. Zhurin, H. R. Kaufman, and R S Robinson. Physics of closed drift thrusters. *Plasma Sources Science and Technology*, 8:R1– R20, 1999.

[3] E. Y. Choueiri. Plasma oscillations in Hall thrusters. *Physics of Plasmas*, 8:1411–1426, 2001.

[4] M. Keidar and I. I. Beilis. Electron transport phenomena in plasma devices with E x B drift. *IEEE Transactions on Plasma Science*, 34:804–814, 2006.

[5] Y. Raitses, D. Staack, M. Keidar, and N. J. Fisch. Electron-wall interaction in Hall thrusters. *Physics of Plasmas*, 12:057104, 2005.

[6] L. Dorf, Y. Raitses, and N. J. Fisch. Effect of magnetic field profile on the anode fall in a Hall-effect thruster discharge. *Physics of Plasmas*, 13:057104, 2006.

[7] R.R. Hofer, I.G. Mikellides, I. Katz, and D.M. Goebel. Wall sheath and electron mobility modeling in hybrid-PIC Hall thruster simulations. *43rd AIAA/ASME/SAE/ASEE Joint Propulsion Conference & Exhibit AIAA 2007-5267*, 2007.

[8] I. Kronhaus, A. Kapulkin, V. Balabanov, M. Rubanovich, M. Guelman, and B. Natan. Investigation of physical processes in CAMILA Hall thruster using electrical probes. *Journal of Physics D: Applied Physics*, 45:175203, 2012.

[9] A. Kapulkin and M. Guelman. Low-frequency instability in near-anode region of Hall thruster. *IEEE Transactions on Plasma Science*, 36:2082–2087, 2008.

[10] Y. Sakawa, C. Joshi, P. K. Kaw, F. F. Chen, and V. K. Jain. Excitation of the modified Simon–Hoh instability in an electron beam produced plasma. *Physics of Fluids B: Plasma Physics*, 5:1681–1694, 1993.

[11] W. Frias, A. I. Smolyakov, I. D. Kaganovich, and Y. Raitses. Long wavelength gradient drift instability in Hall plasma devices. I. Fluid theory. *Physics of Plasmas*, 19:072112, 2012.

[12] A. A. Litvak, Y. Raitses, and N. J. Fisch. Experimental studies of high-frequency azimuthal waves in Hall thrusters. *Physics of Plasmas*, 11:1701–1705, 2004.

[13] A. A. Litvak and N. J. Fisch. Resistive instabilities in Hall current plasma discharge. *Physics of Plasmas*, 8:648–651, 2001.

[14] K. E. Tsiolkovsky. Investigation of outer space using reactive devices (in Russian). 1903.

[15] E. Y. Choueiri. A critical history of electric propulsion: The first 50 years (1906-1956). *Journal of Propulsion and Power*, 20:193–203, 2004.

[16] NASA. Asteroid Redirect Mission (ARM). `https://www.nasa.gov/mission_pages/asteroids/initiative/index.html`, 2015.

[17] A. I. Morozov and V. V Savelyev. Fundamentals of stationary plasma thruster theory. In B.B. Kadomtsev and V. D. Shafranov, editors, *Reviews of Plasma Physics*, volume 21, pages 203–391. Kluver, New York, 2000.

[18] R. Tedrake and B. Pote. Performance of a high specific impulse Hall thruster. *27th International Electric Propulsion Conference IEPC-2001-35*, 2001.

[19] T. D. Kaladze, D. G. Lominadze, and K. N. Stepanov. Experimental studies of high-frequency azimuthal waves in Hall thrusters. *Soviet Physics JETP*, 7:196, 1972.

[20] N. B. Meezan, W. A. Hargus, and M. A. Cappelli. Anomalous electron mobility in a coaxial Hall discharge plasma. *Physical Review E*, 63:026410, 2001.

[21] A. Lazurenko, V. Krasnoselskikh, and A. Bouchoule. Experimental insights into high-frequency instabilities and related anomalous electron transport in Hall thrusters. *IEEE Transactions on Plasma Science*, 36:1977–1988, 2008.

[22] A. I. Morozov and V. V. Savel'ev. Theory of the near-wall conductivity. *Plasma Physics Reports*, 27:570–575, 2012.

[23] S. Yoshikawa and D. J. Rose. Anomalous diffusion of a plasma across a magnetic field. *Physics of Fluids*, 5:334–340, 1962.

[24] G. S. Janes and R. S. Lowder. Anomalous electron diffusion and ion acceleration in a low density plasma. *Physics of Fluids*, 9:1115–1123, 1966.

[25] A. I. Morozov. The conceptual development of stationary plasma thrusters. *Plasma Physics Reports*, 29:235–250, 2003.

[26] E. Y. Choueri. Overview of U.S academic programs in electric propulsion. *35th AIAA Joint Propulsion Conference AIAA–99–2163*, 1999.

[27] A. I. Morozov, Y. V. Esipchuk, A. M. Kapulkin, V. A. Nevrovskii, and V. A. Smirnov. Effect of the magnetic field on a closed-electron-drift accelerator. *Soviet Physics Techical Physics*, 17:482–487, 1972.

[28] A. Ducrocq, J. C. Adam, A. Heron, and G. Laval. High-frequency electron drift instability in the cross-field configuration of Hall thrusters. *Physics of Plasmas*, 13:102111, 2006.

[29] E. Fernandez, M. K. Scharfe, C. A. Thomas, N. Gascon, and M. A. Cappelli. Growth of resistive instabilities in E $\times$ B plasma discharge simulations. *Physics of Plasmas*, 15:012102, 2008.

[30] C. L. Ellison, Y. Raitses, and N. J. Fisch. Cross-field electron transport induced by a rotating spoke in a cylindrical Hall thruster. *Physics of Plasmas*, 19:013503, 2012.

[31] K. Matyash, R. Schneider, S. Mazouffre, S. Tsikata, Y. Raitses, and A. Diallo. 3d simulation of the rotating spoke in a Hall thruster. *33rd International Electric Propulsion Conference IEPC-2013-307*, 2013.

[32] D. Sydorenko, I. Kaganovich, Y. Raitses, and A. Smolyakov. Breakdown of a space charge limited regime of a sheath in a weakly collisional plasma bounded by walls with secondary electron emission. *Physical Review Letters*, 103:145004, 2009.

[33] A. I. Smolyakov, W. Frias, I. D. Kaganovich, and Y. Raitses. Sheath-induced instabilities in plasmas with $E_0 \times B_0$ drift. *Physical Review Letters*, 111:115002, 2013.

[34] W. Frias, A. I. Smolyakov, I. D. Kaganovich, and Y. Raitses. Wall current closure effects on plasma and sheath fluctuations in Hall thrusters. *Physics of Plasmas*, 21:062113, 2014.

[35] E. Fernandez and M. A. Cappelli. Modeling anomalous electron transport in two dimensional simulations of Hall thrusters. *APS Meeting Abstracts 2000APS DPPHM1005F*, 2000.

[36] J. C. Adam, A. Heron, and G. Laval. Study of stationary plasma thrusters using two-dimensional fully kinetic simulations. *Physics of Plasmas*, 11:295–305, 2004.

[37] C. Boniface, L. Garrigues, G. J. M. Hagelaar, J. P. Boeuf, D. Gawron, and S. Mazouffre. Anomalous cross field electron transport in a Hall effect thruster. *Applied Physics Letters*, 89:161503, 2006.

[38] E. Fernandez, A. K. Knoll, and M. A. Cappelli. An axial-azimuthal hybrid simulation of coaxial Hall thrusters. *42nd AIAA/ASME/SAE/ASEE Joint Propulsion Conference and Exhibit AIAA 2006-4329*, 2006.

[39] J.A. Carlsson, I. D. Kaganovich, A.V. Khrabrov, Y. Raitses, A.I. Smolyakov, and D. Sydorenko. Multi-dimensional kinetic simulations of instabilities and transport in $E \times B$ devices. *Joint Conference of 30th International Symposium on Space Technology and Science, 34th International Electric Propulsion Conference and 6th Nano-satellite Symposium IEPC-2015-373/ISTS-2015-b-373*, 2015.

[40] B. D. Dudson, M. V. Umansky, X.Q. Xu, P. B. Snyder, and H. R. Wilson. BOUT++: A framework for parallel plasma fluid simulations. *Computer Physics Communications*, 180:1467 – 1480, 2009.

[41] P. Popovich, M. V. Umansky, T. A. Carter, and B. Friedman. Analysis of plasma instabilities and verification of the BOUT code for the Large Plasma Device. *Physics of Plasmas*, 17:102107, 2010.

[42] M. V. Umansky, P. Popovich, T. A. Carter, B. Friedman, and W. M. Nevins. Numerical simulation and analysis of plasma turbulence in the Large Plasma Device. *Physics of Plasmas*, 18:055709, 2011.

[43] F. Chen. *Introduction to plasma physics and controlled fusion. Volume 1, Plasma physics*. Springer, 1984.

[44] J. D. Callen. *Fundamentals of Plasma Physics (Draft)*. `http://homepages.cae.wisc.edu/~callen/book.html`, 2003.

[45] R. Fitzpatrick. *Plasma physics.* Lecture Notes, University of Texas at Austin, 2011.

[46] J.D. Huba. *NRL plasma formulary*. Naval Research Lab. Washington D. C., 2011.

[47] H. C. Berg. *Random Walks in Biology*. Princeton University Press, 1993.

[48] D. Sydorenko, A. Smolyakov, I. Kaganovich, and Y. Raitses. Effects of non-Maxwellian electron velocity distribution function on two-stream instability in low-pressure discharges. *Physics of Plasmas*, 14:013508, 2007.

[49] A. B. Mikhailovskii. *Theory of Plasma Instabilities: Instabilities of a homogeneous plasma*. Studies in Soviet science: Physical sciences. Consultants Bureau, 1974.

[50] C. N. Lashmore-Davies. Negative energy waves. *Journal of Plasma Physics*, 71:101–109, 4 2005.

[51] D. H. Bohm. *Characteristics of Electrical Discharges in Magnetic Fields, A. Guthrie and R. K. Wakerling (eds.)*. McGraw-Hill, 1949.

[52] N. B. Meezan and Mark A. Hargus, W. A. and. Anomalous electron mobility in a coaxial Hall discharge plasma. *Physical Review E*, 63:026410, Jan 2001.

[53] M. A. Cappelli, N. B. Meezan, and N. Gascon. Transport physics in Hall plasma thrusters. *40th AIAA Aerospace Sciences Meeting and Exhibit AIAA–2002-0485*, 2002.

[54] Y. V. Esipchuk and G. N. Tilinin. Drift instability in a Hall-current plasma accelerator. *Soviet Physics Technical Physics*, 21:417–423, 1976.

[55] E. Chesta, N. B. Meezan, and M. A. Cappelli. Stability of a magnetized hall plasma discharge. *Journal of Applied Physics*, 89:3099–3107, 2001.

[56] D. Escobar and E. Ahedo. Ionization-induced azimuthal oscillation in Hall effect thrusters. *32nd International Electric Propulsion Conference IEPC-2011-196*, 2011.

[57] A. Lazurenko, G. Coduti, S. Mazouffre, and G. Bonhomme. Dispersion relation of high-frequency plasma oscillations in Hall thrusters. *Physics of Plasmas*, 15:034502, 2008.

[58] J. Kurzyna, S. Mazouffre, A. Lazurenko, L. Albarede, G. Bonhomme, K. Makowski, M. Dudeck, and Z. Peradzynski. Spectral analysis of Hall-effect thruster plasma oscillations based on the empirical mode decomposition. *Physics of Plasmas*, 12:123506, 2005.

[59] M. Prioul. Experimental study of Hall-type thrusters. *PhD thesis, Orleans University*, 2002.

[60] S. Tsikata, N. Lemoine, V. Pisarev, and D. M. Gresillon. Dispersion relations of electron density fluctuations in a Hall thruster plasma, observed by collective light scattering. *Physics of Plasmas*, 16:033506, 2009.

[61] S. Tsikata, C. Honore, N. Lemoine, and D. M. Gresillon. Three-dimensional structure of electron density fluctuations in the Hall thruster plasma: ExB mode. *Physics of Plasmas*, 17:112110, 2010.

[62] A. I. Smolyakov, W. Frias, Y. Raitses, and I. D. Kaganovich. Gradient-drift instabilites in Hall thruster plasmas. *32nd International Electric Propulsion Conference IEPC-2011-271*, 2011.

[63] A. Simon. Instability of a partially ionized plasma in crossed electric and magnetic fields. *Physics of Fluids*, 6:382–388, 1963.

[64] J. D. Huba and S. T. Zalesak. Long-wavelength limit of the E $\times$ B instability. *Journal of Geophysics Research*, 88:10263, 1983.

[65] R.N. Sudan, A.V. Gruzinov, W. Horton, and N. Kukharkin. Convective turbulence in weakly ionized plasma. *Physics Reports*, 283:95 – 119, 1997.

[66] B. Coppi, M. N. Rosenbluth, and R. Z. Sagdeev. Instabilities due to temperature gradients in complex magnetic field configurations. *Physics of Fluids*, 10:582, 1967.

[67] J. W. Connor. Transport due to ion pressure-gradient turbulence. *Nuclear Fusion*, 26:193–199, 1986.

[68] W. Horton, D. I. Choi, and W. M. Tang. Toroidal drift modes driven by ion pressure-gradients. *Physics of Fluids*, 24:1077–1089, 1981.

[69] A. Jarmen, P. Andersson, and J. Weiland. Fully toroidal ion temperature-gradient driven drift modes. *Nuclear Fusion*, 27:941–949, 1987.

[70] D. Staack, Y. Raitses, and N. J. Fisch. Temperature gradient in Hall thrusters. *Applied Physics Letters*, 84:3028–3030, 2004.

[71] F. C. Hoh. Instability of Penning-type discharges. *Physics of Fluids*, 6:1184–1191, 1963.

[72] A. Hirose and I. Alexeff. Electrostatic instabilities driven by currents perpendicular to an external magnetic field. *Nuclear Fusion*, 12:315, 1972.

[73] A. M. Fridman. *Soviet Physics Doklady*, 9:75, 1964.

[74] F. I. Parra, E. Ahedo, J. M. Fife, and M. A. Martinez-Sanchez. A two-dimensional hybrid model of the Hall thruster discharge. *Journal Applied Physics*, 100:023304, 2006.

[75] J. M. Fife. Hybrid-PIC modeling and electrostatic probe survey of Hall thruster. *PhD Thesis, Aeronautics and Astronautics, Massachusetts Institute of Technology*, 1998.

[76] T. Ito and M.A. Cappelli. High speed images of drift waves and turbulence in magnetized microplasmas. *IEEE Transactions on Plasma Science*, 36:1228–1229, Aug 2008.

[77] J. Weiland. *Collective Modes in Inhomogeneous Plasmas: Kinetic and Advanced Fluid Theory*. Taylor & Francis, 1999.

[78] A. Lazurenko, L. Albarede, and A. Bouchoule. Physical characterization of high-frequency instabilities in Hall thrusters. *Physics of Plasmas*, 13:083503, 2006.

[79] N. Brenning and D. Lundin. Alfven critical ionization velocity observed in high power impulse magnetron sputtering discharges. *Physics of Plasmas*, 19:093505, 2012.

[80] C. N. Lashmore-Davies and T. J. Martin. Electrostatic instabilities driven by an electric current perpendicular to a magnetic field. *Nuclear Fusion*, 13:193, 1973.

[81] M. Lampe, W. M. Manheimer, J. B. McBride, J. H. Orens, R. Shanny, and R. N. Sudan. Nonlinear development of the beam-cyclotron instability. *Physical Review Letters*, 26:1221–1225, May 1971.

[82] M. Lampe, W. M. Manheimer, J. B. McBride, J. H. Orens, K. Papadopoulos, R. Shanny, and R. N. Sudan. Theory and simulation of the beam cyclotron instability. *Physics of Fluids*, 15:662–675, 1972.

[83] H. V. Wong. Electrostatic electron-ion streaming instability. *Physics of Fluids*, 13:757–760, 1970.

[84] S. Barral, K. Makowski, Z. Peradzyski, and M. Dudeck. Transit-time instability in Hall thrusters. *Physics of Plasmas*, 12:073504, 2005.

[85] A. Simon. Ambipolar diffusion in a magnetic field. *Physical Review*, 98:317–318, 1955.

[86] A. Fruchtman. Ambipolar and nonambipolar cross-field diffusions. *Plasma Sources Science & Technology*, 18:025033, 2009.

[87] T. Lafleur and R. W. Boswell. Particle-in-cell simulations of ambipolar and nonambipolar diffusion in magnetized plasmas. *Physics of Plasmas*, 19:053505, 2012.

[88] B.B. Kadomtsev. Plasma instability. In *7th Conf. on Phenomena in Ionized Gases*, volume 2, page 610, Belgrade, 1965. Consultants Bureau.

[89] H. L. Berk, D. D. Ryutov, and Y. A. Tsidulko. Temperature-gradient instability induced by conducting end walls. *Physics of Fluids B-Plasma Physics*, 3:1346–1354, 1991.

[90] R. H. Cohen and D. D. Ryutov. Sheath physics and boundary conditions for edge plasmas. *Contributions to Plasma Physics*, 44:111–125, 2004.

[91] D. D. Ryutov and R. H. Cohen. Instability driven by sheath boundary conditions and limited to divertor legs. *Contributions to Plasma Physics*, 44:168–175, 2004.

[92] Y. Raitses, M. Keidar, D. Staack, and N. J. Fisch. Effects of segmented electrode in Hall current plasma thrusters. *Journal of Applied Physics*, 92:4906–4911, 2002.

[93] A. W. Smith and M. A. Cappelli. Time and space-correlated plasma potential measurements in the near field of a coaxial Hall plasma discharge. *Physics of Plasmas*, 16:073504, 2009.

[94] A. A. Litvak and N. J. Fisch. Rayleigh instability in Hall thrusters. *Physics of Plasmas*, 11:1379–1383, 2004.

[95] A. Heron and J. C. Adam. Anomalous conductivity in Hall thrusters: Effects of the non-linear coupling of the electron-cyclotron drift instability with secondary electron emission of the walls. *Physics of Plasmas*, 20:082313, 2013.

[96] Y. Raitses, I. D. Kaganovich, A. Khrabrov, D. Sydorenko, N. J. Fisch, and A. Smolyakov. Effect of secondary electron emission on electron cross-field current in E x B discharges. *IEEE Transactions on Plasma Science*, 39:995–1006, 2011.

[97] E. Raitses, J. Ashkenazy, G. Appelbaum, and M. Guelman. Experimental investigation of the effect of channel material on Hall thruster characteristics. *25th International Electric Propulsion Conference IEPC-97-056*, 1997.

[98] J. Szabo, M. Martinez-Sanchez, and O. Batishev. Numerical modeling of the near-anode region in a TAL thruster. *36th AIAA Joint Propulsion Conference AIAA-2000-33653*, 2000.

[99] F. Taccogna, S. Longo, M. Capitelli, and R. Schneider. Anomalous transport induced by sheath instability in Hall effect thrusters. *Applied Physics Letters*, 94:251502, 2009.

[100] J. P. Boeuf and B. Chaudhury. Rotating instability in low-temperature magnetized plasmas. *Physical Review Letters*, 111:155005, Oct 2013.

[101] P. Coche and L. Garrigues. A two-dimensional (azimuthal-axial) particle-in-cell model of a hall thruster. *Physics of Plasmas*, 21:023503, 2014.

[102] J. Fife and M. Martinez-Sanchez. A numerical study of low-frequency discharge oscillations in Hall thrusters. *33rd AIAA Joint Propulsion Conference AIAA-1997-3052*, 2001.

[103] J. P. Boeuf and L. Garrigues. Low frequency oscillations in a stationary plasma thruster. *Journal of Applied Physics*, 84:3541–3554, 1998.

[104] L Garrigues, A Heron, J C Adam, and J P Boeuf. Hybrid and particle-in-cell models of a stationary plasma thruster. *Plasma Sources Science and Technology*, 9:219, 2000.

[105] M. K. Scharfe, N. Gascon, M. A. Cappelli, and E. Fernandez. Comparison of hybrid Hall thruster model to experimental measurements. *Physics of Plasmas*, 13:083505, 2006.

[106] K. Ikeda. Progress in the ITER physics basis. *Nuclear Fusion*, 47, 2007.

[107] X. Garbet, Y. Idomura, L. Villard, and T.H. Watanabe. Gyrokinetic simulations of turbulent transport. *Nuclear Fusion*, 50:043002, 2010.

[108] J. R. Angus, M. Umansky, and S. I. Krasheninnikov. 3D blob modelling with BOUT++. *Contributions to Plasma Physics*, 52:348–352, 2012.

[109] P. Popovich, M. V. Umansky, T. A. Carter, and B. Friedman. Modeling of plasma turbulence and transport in the Large Plasma Device. *Physics of Plasmas*, 17:122312, 2010.

[110] R. H. Cohen, B. LaBombard, D. D. Ryutov, J. L. Terry, M. V. Umansky, X. Q. Xu, and S. Zweben. Theory and fluid simulations of boundary-plasma fluctuations. *Nuclear Fusion*, 47:612–625, 2007.

[111] W. Frias, A. I. Smolyakov, I. D. Kaganovich, Y. Raitses, and M. V. Umansky. Simulation of gradient drift instabilities in Hall thruster plasmas with the BOUT++ code. *APS Meeting Abstracts 2012APS DPPYP8068F*, 2012.

[112] R. D. Hazeltine, M. Kotschenreuther, and P. J. Morrison. A four field model for tokamak plasma dynamics. *Physics of Fluids*, 28:2466–2477, 1985.

[113] A. I. Smolyakov. Gyroviscous forces in a collisionless plasma with temperature gradients. *Canadian Journal of Physics*, 76:321–331, 1998.

[114] A. I. Smolyakov. Elements of neoclassical theory and plasma rotation in a tokamak. In P. H. Diamond, X. Garbet, P. Ghendrih, and Y. Sarazin, editors, *Rotation and Momentum Transport in Magnetized Plasmas*, chapter 7, pages 173–219. World Scientific, Singapore, 2015.

[115] B. D. Scott. Nonlinear polarization and dissipative correspondence between low-frequency fluid and gyrofluid equations. *Physics of Plasmas*, 14:102318, 2007.

[116] W. Frias, A. I. Smolyakov, I. D. Kaganovich, and Y. Raitses. Long wavelength gradient drift instability in Hall plasma devices. II. Applications. *Physics of Plasmas*, 20:052108, 2013.

[117] S. Tsikata, C. Honore, D. Gresillon, A. Heron, N. Lemoine, and J. Cavalier. The small-scale high frequency ExB instability and its links to observed features of the Hall thruster discharge. *33rd International Electric Propulsion Conference IEPC-2013-261*, 2013.

[118] S. Tsikata, J. Cavalier, A. Heron, C. Honore, N. Lemoine, D. Gresillon, and D. Coulette. An axially propagating two-stream instability in the Hall thruster plasma. *Physics of Plasmas*, 21:072116, 2014.

[119] G. W. Hammett and F. W. Perkins. Fluid moment models for landau damping with application to the ion-temperature-gradient instability. *Physical Review Letters*, 64:3019–3022, 1990.

[120] X. Q. Xu, P. W. Xi, A. Dimits, I. Joseph, M. V. Umansky, T. Y. Xia, B. Gui, S. S. Kim, G. Y. Park, T. Rhee, H. Jhang, P. H. Diamond, B. Dudson, and P. B. Snyder. Gyro-fluid and two-fluid theory and simulations of edge-localized-modes. *Physics of Plasmas*, 20:056113, 2013.

[121] A. M. Dimits, I. Joseph, and M. V. Umansky. A fast non-Fourier method for Landau-fluid operators. *Physics of Plasmas*, 21:055907, 2014.

[122] J. P Boeuf. Rotating structures in low temperature magnetized plasmas - insight from particle simulations. *Frontiers in Physics*, 2, 2014.

[123] K. Matyash, R. Schneider, S. Mazouffre, S. Tsikata, Y. Raitses, and A. Diallo. Hall2De simulations with an anomalous transport model based on the electron cyclotron drift instability. *Joint Conference of 30th International Symposium on Space Technology and Science, 34th International Electric Propulsion Conference and 6th Nano-satellite Symposium IEPC-2015-402/ISTS 2015-B-402*, 2015.

[124] A. Anders, P. Ni, and A. Rauch. Drifting localization of ionization runaway: Unraveling the nature of anomalous transport in high power impulse magnetron sputtering. *Journal of Applied Physics*, 111:053304, 2012.

[125] N. Brenning, D. Lundin, T. Minea, C. Costin, and C. Vitelaru. Spokes and charged particle transport in HiPIMS magnetrons. *Journal of Physics D: Applied Physics*, 46:084005, 2013.

[126] S. Tsikata and T. Minea. Modulated electron cyclotron drift instability in a high-power pulsed magnetron discharge. *Physical Review Letters*, 114:185001, 2015.